Evaluation of model-based RSA for *in vivo* measurement of polyethylene wear in a total knee replacement

By

Trevor C. Gascoyne

A Thesis submitted to the Faculty of Graduate Studies of
The University of Manitoba
in partial fulfilment of the requirements of the degree of

MASTER OF SCIENCE

Department of Biosystems Engineering
University of Manitoba
Winnipeg

Abstract

There is a need for a repeatable method of measuring polyethylene wear in total knee replacement (TKA). Model-based radiostereometric analysis (MBRSA) is a high accuracy diagnostic tool with the potential to meet this need; however, a number of unknowns must be examined. This research examines optimized patient positioning for MBRSA imaging as well as *in vitro* validation of a wear measurement technique using a loaded TKA phantom to mimic patient physiology.

Imaging along the antero-posterior and medio-lateral axes of the patient achieved optimal MBRSA accuracy of better than 0.035 mm (in-plane) and 0.12° (in-plane). The developed MBRSA technique underestimated TKA wear on previously-worn polyethylene bearings; however, a number of factors can be corrected to improve this discrepancy. This research provides an overall methodology for measuring TKA wear, but additional experimentation and an improved physiological phantom are needed to obtain accurate wear measurement.

Acknowledgments

Jason Morrison - for his role as supervisor, for his incredible support and praise throughout, for his help in all aspects of planning, analyzing, writing, and defending.

Thomas Turgeon for his invaluable input to the project as well as his wealth of knowledge of knee arthroplasty, his willingness to lend a hand, and for funding to purchase the software and equipment needed for the completion of this project.

Martin Petrak for use of the x-ray suite and equipment at the Concordia Hip and Knee Institute as well as his input and research ideas.

Jitendra Paliwal, for his role as my internal committee member and his willingness to meet and discuss my progress throughout.

Dale Bournes and Robert Lavalee, for their help in designing and building of the mechanical components of my project.

Tarek El-Makawy, for his help with statistical analysis and designing my experimental process.

Sean O'Brien and Alex Vecherya, for their assistance with the 3-D scanner and Solidworks.

Contents

List of Tables

List of Figures

Chapter 1

Introduction

1.1 Overview

Osteoarthritis is the leading cause of total knee arthroplasty in North America with upwards of 90% of all patients undergoing a total knee replacement (TKR) having a primary diagnosis of osteoarthritis (OA) [1]. The pain caused by osteoarthritis can generally be managed for a relatively short period of time by non-surgical means such as anti-inflammatory medications [2, 3] and hydro-cortisone injection [4, 5]. However, because osteoarthritis is a degenerative disease, the proven treatment for end-stage osteoarthritis is partial or total knee replacement (TKR) [6].

The prevalence of knee osteoarthritis and subsequent total knee arthroplasty (TKA) is on the rise in North America due to an increasing level of obesity in the general population [7-9]. Increased body mass index (BMI) in young patients (<55 years of age) has been correlated to an increase in knee arthroplasty for this age group [6, 10-12]. As well, young patients have shown a reduced survivorship in their primary knee replacements due to the more rigorous demands they place on their artificial joints [13].

Higher patient activity levels coupled with increased body weight can cause great amounts of stress on knee replacement components. High stresses can lead to mechanical loosening of the implants, excessive wear, and even fracture of the components [14, 15]. Revision knee arthroplasty must be performed when any of these endpoints are reached. Revision surgeries are generally more painful and invasive for the patient and tend to require longer hospital stays and physical rehabilitation time [16]. Additionally, patient outcomes after revision surgery are generally not as good as primary knee replacement surgery [17].

It is evident that artificial knee replacements must be designed to withstand increasing demands from patients for longer periods of time with fewer complications and failures. The resulting decrease in revision surgeries would reduce the burden placed on the patients (pain and rehabilitation time) as well as the healthcare system.

1.2 Anatomical Terminology

The human body is a complex structure that is most accurately and efficiently described using a medical vocabulary. The following is a glossary of anatomical terminology used in this thesis. This glossary is focussed on the terms frequently used to describe the location of a structure or landmark, direction of motion and axes (or planes) of the body [18].

Proximal: Nearest the trunk or the point of origin, said part of a limb, of an artery or a nerve, so situated. Toward the median plane.

Distal: Situated away from the center of the body, or from the point of origin.

Medial: Nearer to the midline of the body.

Lateral: On the side. Farther from the median or midsagittal plane.

Bilateral: Relating to, or having, two sides.

Supine: The body when lying face upward.

Internal/external rotation: The turning of a limb about its axis of rotation towards or away from the midline of the body.

Antero-posterior rotation: Rotation towards the anterior or posterior of the body.

Varus/valgus rotation: Rotation of the distal portion of the limb towards or away from the midline of the body.

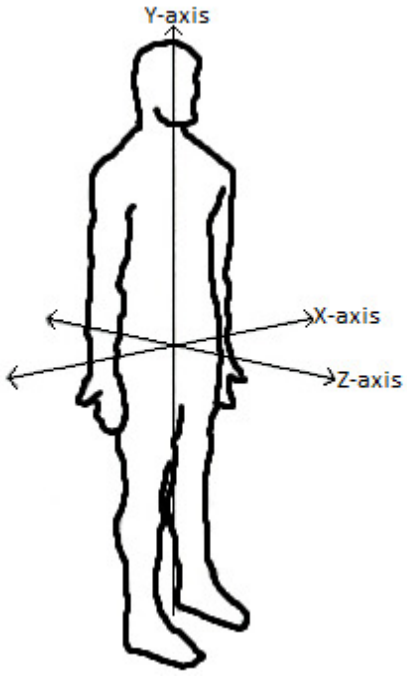

Figure 1: Anatomical axes of the body.

1.3 The Knee Joint

The knee joint is a complex joint, specifically in terms of kinematics between the tibia and femur. The meniscus is the thick layer of hyaline cartilage that covers the proximal surface of the tibia, known as the tibial plateaus (Figure 2A). The meniscus allows for low-friction articulation between the tibia and the femur and provides some shock absorption between the leg bones. The distal surface of the femur is made up of two smooth, curved surfaces known as condyles, which are covered by a thin layer of hyaline cartilage (Figure 2B). Unlike the hip joint, the knee joint is relatively unconstrained, allowing the tibia to both rotate and translate with respect to femur (Figure 3). The predominant kinematic movements of the knee are rolling (with a no-slip condition between the surfaces) and sliding (with relative translation without rotation) as shown in Figure 3. Due to the unconstrained nature of this joint, individual kinematics vary significantly between patients and depend on the activity being performed.

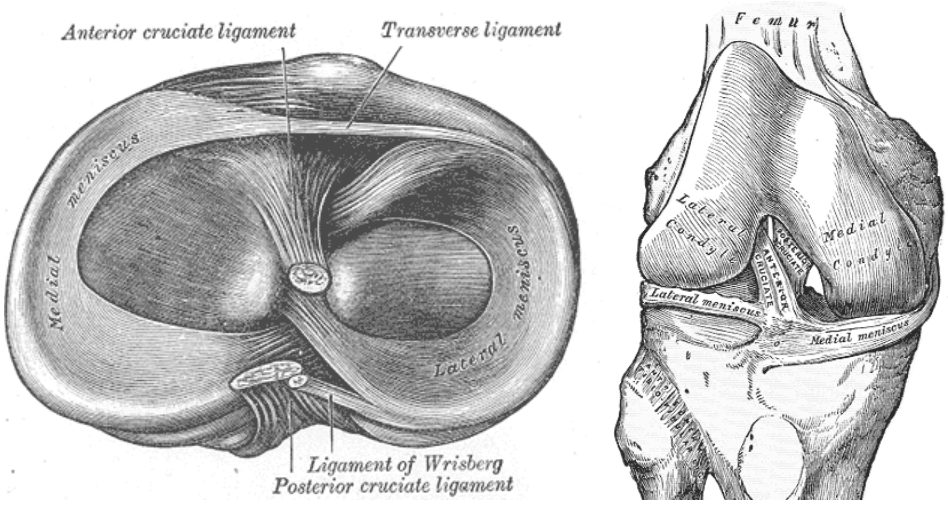

Figure 2: A) Superior view of the meniscus cartilage showing locations of the anterior and posterior cruciate ligaments [20], B) anterior view of the knee joint showing the meniscus and condyle cartilage [20].

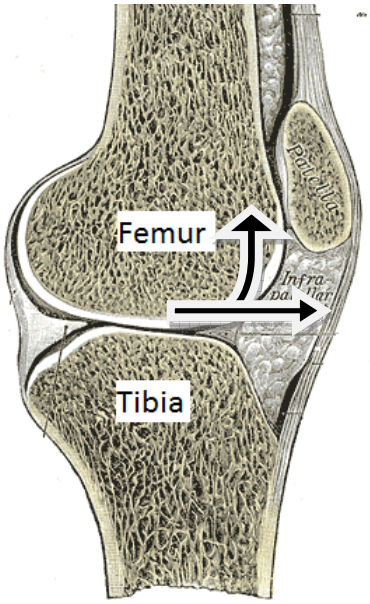

Figure 3: Anterio-posterior rolling and sliding motion of the knee joint [20].

1.4 Total Knee Arthroplasty

Total knee arthroplasty (TKA) also known as total knee replacement (TKR) involves the complete resurfacing of both the tibial plateau and the femoral condyles, and in some cases the patella as well. Modern total knee replacement prostheses generally consist of a femoral component with smooth condylar surfaces for articulation; a tibial tray and post; and a plastic bearing. One of two types of bearings/prostheses are used: fixed bearing prostheses which have their bearings fixed to the tibial tray by a locking mechanism, and mobile bearing prostheses have bearings that are free to rotate and/or translate on the surface of the tray. It has been suggested that a mobile polyethylene bearing reduces polyethylene wear by reducing the cross-shear forces which result from the non-linear rolling

and sliding motions of a knee joint [21]. However, additional polyethylene wear is encountered by the inferior surface (backside) of the bearing as it moves against the tibial baseplate [22]. For this reason, neither bearing has been confirmed as superior [23, 24].

Additional designations exist for both fixed- and mobile-bearing total knee replacements that depend upon whether or not the posterior cruciate ligament (PCL) is or is not removed during surgery. The PCL sacrificing designs (CS) require PCL removal, while PCL retaining designs (CR), require that the ligament not be removed during surgery. The (CS) designs have a posterior post on the bearing that prevents unwanted range of motion of the knee. Alternatively, the CR designs are shaped to allow the presence of the PCL, and thus a stability post is not needed. In general, cruciate-retaining designs are indicated for younger patients with good ligament quality [25].

Survivorship of total knee replacements varies due to a wide range of factors including patient activity level [12]; implant design [26, 27] and materials [28]; implantation technique [29]; and others [30, 31]. What has been shown through large-scale registry data from Australia, North America, and Northern Europe [32] is that knee replacements that are cemented into the bone generally have improved survivorship over uncemented components. For this reason, the standard treatment at the Concordia Hip and Knee Institute is to use a cemented prosthesis.

Due to the complex kinematics and surface interactions of the knee joint, rapid wear of the plastic bearing has also been a concern in total knee replacements [33, 34]. In the past decade, significant improvements have been made in the material properties which have increased the overall wear resistance of the plastic and thus presumably increasing the length of survivorship of total knee replacements [33].

1.4.1 Ultra High Molecular Weight Polyethylene (UHMWPE)

Ultra High Molecular Weight Polyethylene UHMWPE is a combined structure of crystalline and amorphous regions of multiple ethylene chains. It was first used in a total hip replacement in 1962 by Sir John Charnley [35]. This material has been continually used as a bearing surface in total joint replacements over the past 5 decades [36] due to its inherent toughness and resistance to fracture [37]. UHMWPE has been shown to last up to 15-20 years in a typical knee replacement before it wears out [11]. The particles of polyethylene that are produced from this wear have been shown to cause bone resorption (alternatively known as osteolysis), which often leads to loosening of the implant and thus necessitates revision surgery [38, 39]. Better wear resistance and material toughness can increase the longevity of polyethylene bearings, which is quickly becoming a necessity as younger, heavier patients are receiving total knee replacements [33].

Cross linking of UHMWPE was first examined in the early 1990's with evidence of significantly reduced wear rates compared to non-cross linked polyethylene [40]. Cross-linking is done with gamma irradiation in the range of 40 – 100 kGy [41, 42], which creates additional linkages between the ethylene chains. In 1998, highly cross-linked UHMWPE was introduced to the arthroplasty market [14]. The major concern associated with irradiated polyethylene was the production of free radicals during the cross-linking treatment. The first generation of highly cross-linked polyethylene components employed post-irradiation melting and annealing (heating to just below the melting point) to reduce free radicals in the plastic [14, 43]. These first-generation bearings had much greater

wear resistance but reduced other mechanical properties (toughness, ductility) relative to non-cross-linked polyethylene.

Second generation cross-linked polyethylene components have recently been introduced to the market. Sequential annealing and incorporation of anti-oxidant additives such as vitamin E, are claimed to significantly reduce free-radicals in the polyethylene while maintaining high wear resistance [44, 45]. These materials have been examined *in vitro* with material testing machines (pin-on-disc wear testing) and joint simulators [46], but little literature is available on their *in vivo* performance [47].

1.4.2 Wear

Many studies have examined the rate of wear of many different types of polyethylene bearings in hips [47, 48], knees [49, 50], shoulders [51, 52], ankles [53, 54], and spinal disc replacements [55]. Wear rate is highly dependent on a number of material factors such as how it is manufactured, processed, and treated [15]. As well, patient weight, patient activity level, *in vivo* joint lubrication, the articular surface properties, and other factors all contribute to the annual rate of wear of polyethylene bearings [56]. In total hip replacements, polyethylene wear is generally reported in terms of linear penetration of the femoral head into the acetabular cup [48]. Similarly, *in vivo* polyethylene wear in knees is generally reported in terms of proximity between the femoral condyles and the tibial tray [49, 57]. However, during the first 6 months to 1 year of implantation, this increase in proximity (penetration) is largely due to cold flow, or creep, of the polyethylene [58, 59]. After the first year, it is generally accepted that polyethylene creep has finished, and thus the subsequent penetration is a direct result of polyethylene wear [58, 59].

Conventional, non-cross linked polyethylene components in total hip replacements have shown penetration (wear) rates between 0.05 and 0.4 mm per year [49, 60, 61]. Highly-cross-linked polyethylene has shown wear rates that are generally less than 0.07 mm per year [62-66]. This reduction in wear and subsequent wear particles has been shown to reduce the occurrence of osteolysis and increased longevity of the artificial joint [63].

In vivo measurement of cross-linked polyethylene wear in the short-term (less than 3 years) is difficult due to the miniscule amount of linear penetration that occurs during this time [47, 62]. Measurement of wear in total hip replacements is significantly easier compared to total knee replacements simply because of the 'ball and socket' nature of the hip joint. Only one study by Gill et al. in 2006 [49] examined polyethylene wear in a total knee replacement after 6 years *in vivo* using the technique of radiostereometric analysis. Gill was able to quantify the linear and volumetric wear of the polyethylene bearings as approximately 0.1 mm and 100 mm^3 per year, respectively. However, this research has not yet been repeated by other researchers and a number of possible optimisations and analyses remain unexplored, including the work considered in this thesis.

1.4.3 Genesis II Total Knee Replacement

The Genesis II total knee replacement system (Smith & Nephew, Memphis, TN) is a joint replacement system that has performed well during more than 10 years of clinical use (Figure 4). The model chosen for this research is the cruciate sacrificing, fixed-bearing design since it is the most common type of knee replacement implanted at the Concordia Hip and Knee Institute (CHKI) (pers. comm. Dr. Thomas Turgeon). Additionally, over

100 Genesis II total knee replacement systems have been retrieved at the CHKI's implant retrieval laboratory. Extensive analysis has been performed on this implant type and communication is well established with the Smith & Nephew (Memphis, TN) company.

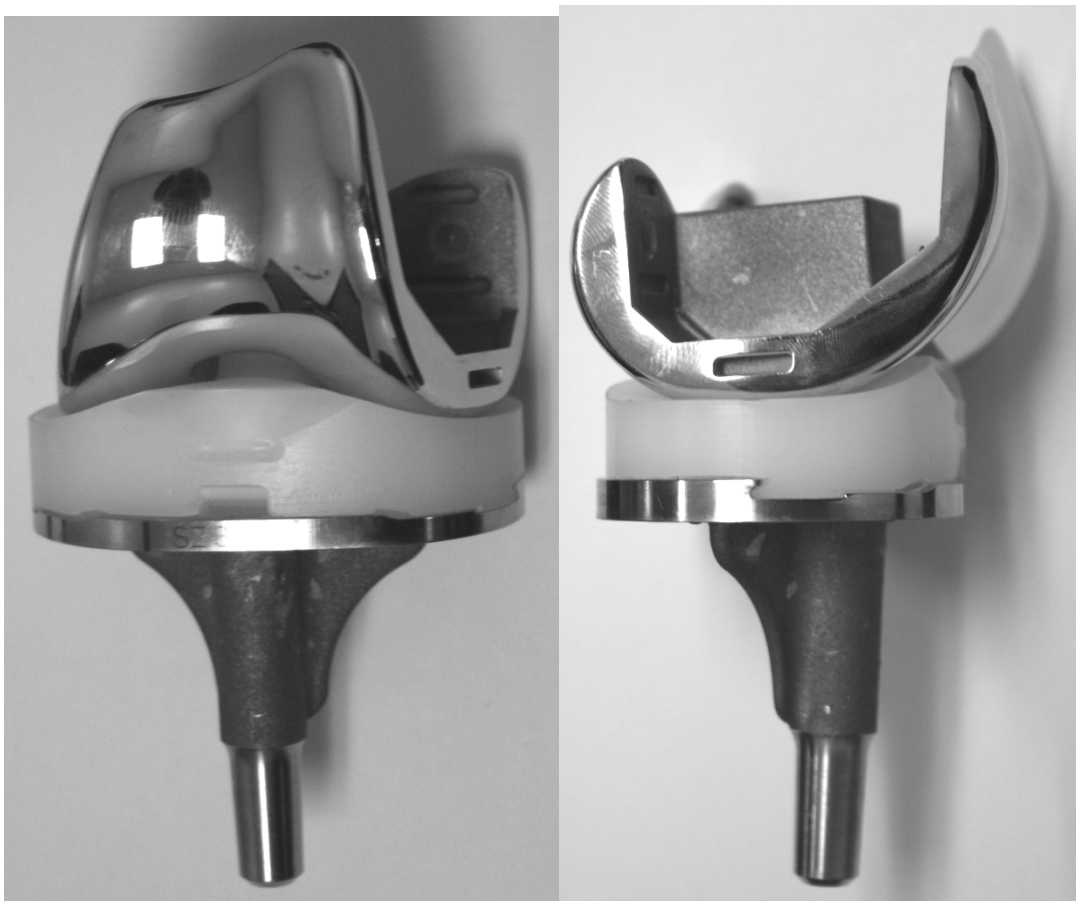

Figure 4: Genesis II posterior stabilized total knee replacement system from Smith & Nephew (Memphis, TN).

1.5 Radiostereometric Analysis

1.5.1 Overview

Radiostereometric analysis (RSA), also known as roentgen stereophotogrammetric analysis, is a technique for determining the three-dimensional location of an object in the body using bi-directional radiographs. The underlying principle of RSA is akin to depth perception in human vision, except with the use of a coordinate frame and relatively simple geometric calculations. The location of an object of interest is calculated as the intersection of back-projected lines between each x-ray focus and the silhouette of the object in each image.

RSA was developed by Goran Selvik during the early 1970's in his doctoral thesis [68]. Initially, RSA was used for analysis of skeletal kinematics and measurement of bone growth [69, 70]. RSA was first applied to orthopaedics in the late 1970's with excellent results [71]. Due to the high level of precision and accuracy attainable with RSA [69, 72], small sample sizes and short follow-up periods are acceptable to predict the survivorship of an implant [73-75]. Therefore, RSA has proven to be a very valuable tool for clinical validation of new implant designs, coatings, cements, and surgical methods. Many lessons have been learned about implant survivorship thanks to the ability to measure early *in vivo* motion (micromotion) of the implant [74, 76, 77].

Two main methods of RSA exist; the conventional marker-based method and the newly-developed model-based method. Conventional RSA requires the implant to be premarked with small beads in order to determine the position of the implant. Model-based

RSA estimates implant position by matching a virtual projection of a computer model of the implant to the implant silhouette on the x-ray image, thereby removing the need for pre-marked implants [78, 79]. Both model- and marker-based RSA were used in this research; however, only the model-based RSA software (mbRSA, Medis Specials, Leiden, The Netherlands) and equipment (Halifax Biomedical, Mabou, NS) has been closely analyzed.

1.5.2 Applications of RSA

A number of types of studies can be performed using RSA. Longitudinal studies examine relative motion between an implant and the surrounding bone over time [80]. Inducible displacement studies examine motion of the implant relative to the bone between loaded and unloaded conditions of the joint [81]. Kinematic studies examine the relative motions between the two sides of the joint and how they interact during movement [82]. Wear studies examine the reduction of inter-implant distance over time, which is indicative of polyethylene wear [48]. The research for this thesis focussed on wear measurement in a total knee replacement.

1.5.3 Intra-Operative Marker Insertion

RSA requires the implantation of tantalum (a radio-opaque, biocompatible metal [83]) markers into the patient's bone during surgery. A minimum of 3 markers are required for analysis of relative motion between bone and implant [84]. Generally 5 to 10 markers are inserted per bone segment (pelvis, femur, tibia, etc.). These implanted markers provide the necessary reference points required to measure micromotion of the implant. Sufficient

distribution (spread) of markers is required to reduce the error associated with small motions of the markers [84]. The condition of marker distribution is improved with a greater number of markers that are further apart in all dimensions such that they are not collinear (lie on a line) or coplanar (lie in one plane). The condition number (CN) quantifies the quality of marker distribution, and is defined by the equation;

$$CN = \sqrt{\frac{1}{d_1^2 + d_2^2 + \ldots + d_n^2}}$$

Where d is the distance between each of n markers and a regression line passing through the cluster of markers which minimizes CN [85]. A lower CN indicates a better spread of markers and as such is generally restricted to less than 90 [86].

1.5.4 Examinations

An initial reference RSA examination is taken within the first 6 weeks after surgery to represent the initial position of all components within the patient's bone. Successive examinations are obtained during specified follow-up periods (generally at 6 months, 1 year, 2 years, etc) in order to provide a progression of motion between the implant and the bone or between components of the implant (wear).

Figure 5: A) Supine RSA examination of the hip, and B) Standing RSA examination of the knee, both with the carbon-fibre uniplanar calibration box from Halifax Biomedical (Mabou, NS) with x-ray sources at 30° from orthogonal to the calibration cage.

An examination is comprised of two x-ray sources (tubes) positioned above (Figure 5A) or in front (Figure 5A) of the patient at a specified angle to each other with a specialised calibration cage centered below or behind the patient (respectively). The implant is positioned within the area of crossing x-rays such that it is visible in both radiograph images. The x-ray sources are synchronized for rapid simultaneous exposure (20-50 milliseconds) [84] in order to reduce the error resulting from patient motion. The x-rays are given a high potential (kilovolts, kV) but are of a low power (mAs) in order to maximize the image contrast while reducing the patient radiation dose [84, 87]. The x-ray images are obtained by cassettes (analog) or detectors (digital) which are placed underneath or behind the calibration cage. These images are then transferred into a specialized analysis program in which a local coordinate system is determined, the bone and implant markers or contours are located, and rigid-body kinematics are performed.

The calibration cage is a precisely manufactured device that establishes a global co-ordinate system necessary to analyse implant micromotion. In general, tantalum markers are embedded into the surface of the cage on either side of center. The surface markers are referred to as fiducial markers, and they provide scale to x-ray images and calculate dimensions of the imaged true object (Figure 6). Additionally, markers are embedded into the cage above the level of the fiducial markers. These are known as control markers, and they are used for calculating the precise center of the x-ray foci (Figure 7). The calibration cage used in this research is the uniplanar carbon-fibre calibration box from Halifax Biomedical (Mabou, NS) (Figure 7).

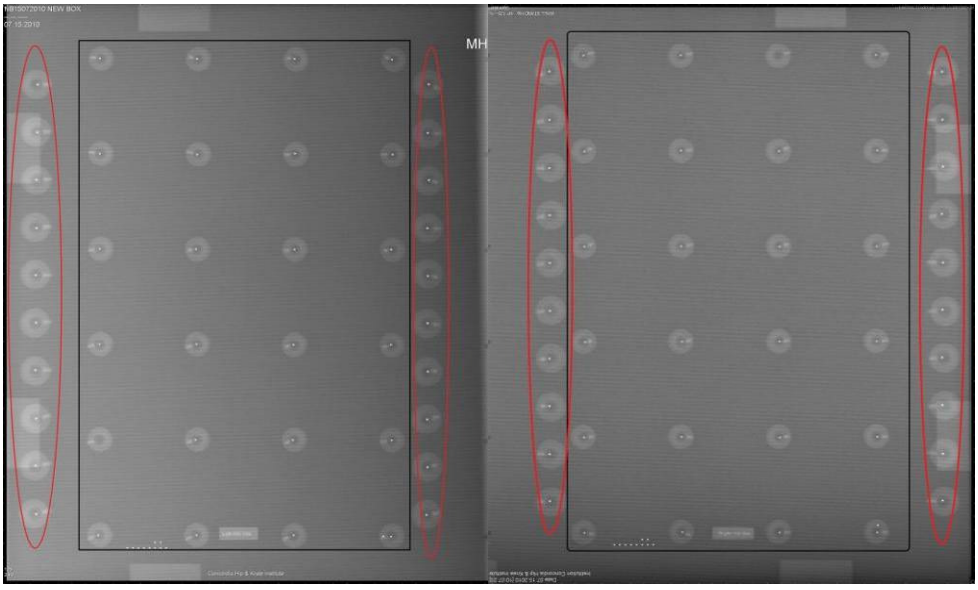

Figure 6: Radiographic images of the left and right sides of the Halifax Biomedical calibration cage, showing the fiducial markers (black squares) and the control markers (red ovals).

Figure 7: Halifax Biomedical uniplanar calibration cage showing the control markers on either side of the cage. The fiducial markers are not visible as they are located inside this enclosed cage.

1.5.5 Analysis of Motion

Calibration cage markers are detected automatically by mbRSA, whereas bone and implant markers are detected manually by user selection. Location of the marker centers is done by computing the center of the detected marker using the Canny edge detection algorithm [86]. The radiograph images are calibrated using the control and fiducial markers present in each image to provide the global coordinate system.

The locations of bone and implant markers are approximated by the intersection of the two back-projected lines between the x-ray images and the foci. Marker location is approximated since it is rare that these back-projected lines actually intersect; a result of x-ray diffraction and variation within the x-ray beam when striking an object. Therefore, the midpoint of the shortest line connecting these non-intersecting rays is defined as the center of the marker. This line is called the crossing-line distance, and it is usually less

than 0.2 mm [86]. Implanted markers and those fixed to implants are generally separated into groups called segments, by the user in order to distinguish between moving and non-moving 'bodies'.

All visualized markers in a particular segment are used to create a rigid body, with inter-marker distances and angles. These distances and angles are used to match the rigid bodies between successive follow-up examinations. Generally, the bone markers are defined as the non-moving segment and the implant or implant markers are defined as the moving segment. Motion that is measured between two segments over time is *in vivo* micromotion.

Three-dimensional motion is defined with 6 degrees of freedom; however, a commonly used description of motion is maximum total point motion (MTPM). The calculation for MTPM is the three-dimensional case of Pythagoras' theorem:

$$MTPM = \sqrt{x^2 + y^2 + z^2}$$

Where x, y, and z are translations in each axis. This formula can also be applied to small rotations (less than 5°) as a summation of the approximate total rotation that has occurred. Translations originate at the right side of the patient and rotations follow the right-hand-rule [86]. Motion is typically placed at the centroid of the rigid body.

Rigid body error (RBE) is defined as the mean difference of inter-marker distances when matching marker segments between successive follow-up examinations. It is defined by the equation;

$$ME = \sqrt{\sum d_R^2 / n}$$

Where d_R^2 is the residual distance of matching markers between successive rigid bodies after rotation of the rigid bodies has been optimized and overall rigid body displacement has been accounted for [81, 88]. Differences in inter-marker distances are a result of unwanted motion of the bone or implant markers whether it is due to loosening of the markers or to bone reformation processes which occur naturally. The RBE is generally restricted to less than 0.3 mm as an average for all markers in each segment.

1.5.6 Error in RSA

Errors in radiostereometric analysis result from a multitude of surgical, examination, radiographic, and random factors [84, 86]. During surgery, the number and distribution of markers implanted into the bone affects the reliability of rigid-body measurement. During follow-up patient examinations, incorrect setup of the RSA equipment reduces the accuracy of calculation of the x-ray source centers, thereby reducing the accuracy of locating markers and implant. Non-simultaneous exposure of x-rays introduces motion of the patient between the radiograph pair. Inappropriate selection of x-ray parameters (kV and mAs) decreases the quality of the x-ray images by either washing-out the features in the image (power too high), or by over-attenuation of the x-rays (power too low) which results in a grainy, fuzzy image. Poor patient positioning may cause occlusion of the implanted markers which can affect the quality of the marker rigid-body. Mislabelling of radiographs can result in an incorrect radiograph pair being analyzed.

The radiographic technology being used can also greatly affect the associated errors. New-generation digital radiography (DR) is superior to older, conventional radiography (CR) equipment in both the delivery of the x-rays and collection/absorption of the x-rays

[89]. Pixel density and absorption sensitivity of the exposure plates can affect the level of error. If all of the above factors are properly addressed there remains random errors, such as x-ray diffraction, x-ray attenuation, and non-crossing x-rays that can all affect the precision and accuracy of the RSA system, and over which, we have limited control.

1.5.7 Model-Based RSA

In the past decade, model-based radiostereometric analysis has been developed as an improved tool for detecting *in vivo* motions of implants. As mentioned, model-based RSA estimates the *in vivo* position and orientation (pose) of an implanted prosthesis by matching real and virtual outlines of the implant in both RSA images (Figure 8). Conventional marker-based RSA has greater accuracy and precision than model-based RSA because marker centers are easier to locate and define, whereas implant contours can vary due to manufacturing and processing tolerances. Despite this, mbRSA still attains between 0.05 and 0.3 mm translational precision and between 0.1 and 1.0^{o} rotational precision [90-93]. The main benefit of mbRSA is that the joint prostheses do not need to be pre-marked with tantalum beads; however, markers are still required in the bone to serve as reference points.

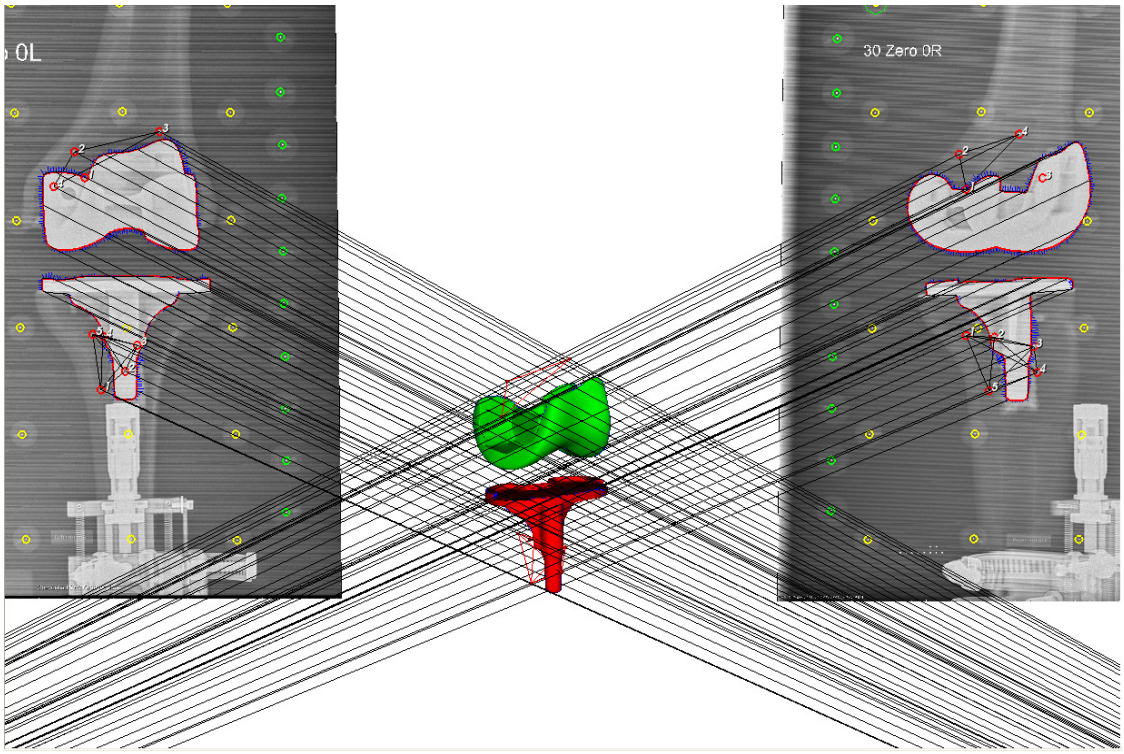

Figure 8: Projection of implant models (red & green) onto the x-ray images in mbRSA.

1.5.8 Validation of RSA

Validation of radiostereometric analysis is performed using *in vitro* models, or phantoms, which generally consist of artificial bone(s) and an attached joint prosthesis. Phantom studies are undertaken to determine both the accuracy and precision (repeatability) of the RSA system. The precision of the RSA system is defined as the closeness of agreement between independent test results under stipulated conditions [94]. Whereas, the accuracy of the RSA system is defined as the closeness of agreement between a test result and the accepted reference, or true value [94]. In both cases, the RSA output is compared to a known amount, thereby providing a measure of the system's repeatability and trueness of

measurement. The purpose of the phantom model is to mimic the joint of interest using real implants and artificial human bones, such that it is anatomically correct and can be precisely controlled during testing.

1.6 Objectives

The goal of this research is to develop a repeatable method for accurately measuring the *in vivo* wear of a polyethylene tibial insert in a total knee replacement. It is hoped that this method will be applied to future clinical studies examining polyethylene wear in total knee replacements at the Concordia Hip and Knee Institute and other RSA research centers.

The main objectives of this research are;

1. To determine the patient-radiograph orientations and knee flexion angles with the greatest *in vitro* precision and accuracy using a TKA phantom.
2. To validate the orientation and flexion angles with the greatest accuracy by applying them to RSA examinations of a physiologically-loaded TKA phantom.
3. To determine the feasibility of MBRSA as a technique for measuring polyethylene wear on TKA bearings, including x-ray acquisition, radiograph processing, and the analysis of wear.

1.7 Structure of Thesis

This thesis is roughly divided into chapters consisting of introductory material, methods and materials, results of experiments, and discussion of the research. Chapter 1 is a brief introduction to total knee arthroplasty, the Genesis II total knee replacement, radiostereometric analysis, analysis of error in RSA, and the objectives for this research. Chapter 2 contains materials and preliminary methods, including the design and construction of two RSA phantoms, the reverse engineering of TKA components, and implantation of the components onto artificial bones.

Chapter 3 contains a brief, but focussed introduction to model-based RSA and error analysis. It also contains the methods and materials of both the experiment looking at optimal patient-radiograph orientation based on MBRSA precision as well as the experiment quantifying the accuracy of those optimal orientations. Chapter 4 consists of a brief introduction to wear measurement in a TKA as well as the methods and materials for the physiologically-loaded phantom experiment. Chapter 5 contains all of the results for the aforementioned three experiments including summarized tables, figures, and images immediately pertinent to this research. Chapter 6 contains a full discussion of the results and outcomes from all experiments as well as discussion of the limitations of this research, an overall conclusion to the thesis, and discussion of possible future work.

Should the reader be interested in reading the accuracy, precision, or physiologically loaded phantom experiments, then the relevant sections of Chapters 2-6 could be read. In each case the material in each chapter relates to accuracy, precision and physiologically

loaded phantom experiments primarily in that order with section headings indicating the content appropriately.

The appendices A through E contain additional data pertaining to the precision experiment. Appendix A contains detailed explanations of the Anderson-Darling test for normality, 95% prediction intervals surrounding a regression line, and analysis of variance tables. Appendix B contains seven tables of precision data for translation and rotation along or about all axes of motion. Appendix C contains the results of normality tests on subsets of precision data as well as a summary table of the results from parametric and non-parametric ANOVAs. Appendix D contains four tables of the weighted scoring process that was applied to subsets of the precision data. Appendix E contains summarized tabulated data of model-to-marker precision data.

Appendix F contains additional data pertaining to the accuracy experiment. This data consists of two tables summarizing the means, standard deviations, and 95% prediction interval widths of accuracy data. Appendix G contains additional data pertaining to the physiological experiment. This data includes: a table summarizing the RSA-measured volume and surface area of the wear areas on each polyethylene insert; a second table consisting of volume to surface area ratios for each insert and each image or combination of images; a third table summarizing the results of the repeated measurements of a loaded and unloaded polyethylene insert and; a series of images showing the RSA-measured wear areas on each insert for each RSA image.

Chapter 2

Instrumentation & Models

2.1 Introduction

In vitro testing using a phantom model is a frequently used methodology that helps quantify the precision and accuracy of a radiostereometric analysis system [85, 95]. A phantom that is designed for measuring precision typically requires repeated measurements of the distance between two or more objects or markers when no relative motion has occurred. Frequently, the phantom construct itself is moved around the image area of the radiographs to create non-identical images, but the objects of interest remain stationary with respect to one another. A phantom that is designed for measuring accuracy typically involves the measurement of a series of induced motions (rotation or translation) that are known to the observer. The motion is most often induced using highly-accurate micro manipulators such as translation slides and rotation tables [93, 96].

2.2 Design Process

The design process for the phantom model to be used in this research has been documented in order achieve the various requirements and constraints. Following the design flow shown in Dym and Little's Engineering Design text [97], figure 2.1, the following aspects were studied.

2.2.1 Problem Definition

The purpose of this research is to build a phantom model to assist in determining the best technique to measure polyethylene wear in a total knee replacement using model-based radiostereometric analysis. The main objectives are to establish the *in vitro* precision of the mbRSA system, establish the *in vitro* accuracy of the mbRSA system, and accurately quantify polyethylene wear in a clinically relevant fashion.

Here the precision of the mbRSA system is defined to be the deviation in position and orientation between the tibial tray and the femoral condyles when no relative motion has occurred. The accuracy of the mbRSA system to be the agreement between a known displacement and what is measured by mbRSA. The primary metric analysed is the superior-inferior (Y axis) translational accuracy as this direction of motion is very important for measurement of polyethylene wear. Secondary metrics include a summation of the remaining directions of translation; medio-lateral (X axis), and antero-posterior (Z axis), as well as a summation of rotation about all axes.

The constraints placed on the design of the phantom model are numerous. The phantom model must be radiolucent (allow x-rays to pass without attenuation) from the front

and sides, and not create large artefacts in the radiographs. The phantom must maintain rigidity during radiographic examination, withstand loading forces of up to 60 kg (590 N), and be useable by one person (e.g., manoeuvrable and liftable). Additionally, the phantom must be representative of a clinical RSA examination; in terms of orientation of the bone segments, alignment of the components, and freedom of movement between the tibia and femur. The cost of the phantom model must also be within a budget of $500 to $1000.

2.2.2 Conceptual Design

The functionality requirements for the phantom model were taken into account before a conceptual design was created. Because the phantom is to be used in three different stages of testing, the required functions have been separated for each stage: precision, accuracy, and then physiological conditions.

Precision phantom requirements

Rigid support of the tibia and femur is essential in order to maintain zero displacement between the components. Minor bumps and vibrations experienced during re-positioning of the phantom and radiographic equipment cannot affect the positions of either component.

The femur segment must facilitate flexion of 0° to 90° with respect to the tibia segment. As an added constraint, flexion must originate from the femur such that contour overlap between the tibial and femoral components is not encountered as this limits the ability of mbRSA to accurately locate each component. The flexion range is notably lim-

ited to 0-90° as this range of motion is achievable by most TKA patients, regardless of their style of prosthesis.

The phantom support frame and fixtures (including fasteners and mounts) must be radiolucent in order to prevent the occlusion of, or overlap with, the phantom components or the calibration cage markers as this affects the accuracy of mbRSA. Additionally, the support frame and fixtures must be radiolucent from all angles in order to facilitate multi-directional radiographs.

The phantom model components must be designed such that a cluster of tantalum-markers can be inserted into, or affixed to the surface of, the artificial bones. A marker cluster is necessary for direct comparison between model-based RSA and the gold-standard marker-based RSA (reference). A grouping of at least 5 markers is required in both the tibia and femur and these markers cannot be occluded by the prosthesis or the support frame, as this reduces the accuracy of RSA.

Accuracy phantom requirements

In addition to the requirements described above, the accuracy stage of testing requires accurate, reproducible displacement and rotation of the femur and/or tibia. Numerous researchers [93, 95] create such displacements and rotations by utilizing highly accurate translation slides and rotation tables. These components are manufactured to high tolerances and have a known accuracy limit, which is well below the previously published detection limit of radiostereometric analysis [95]. The phantom support frame must also be able to affix a translation slide and rotation table in a rigid fashion such that motions can be induced along and about each axis.

Physiological phantom requirements

This final stage of testing does not require the high accuracy of the two previous stages described above. It does however, require additional freedom of movement in the artificial knee joint, as well as the ability to apply force to the joint in order to measure polyethylene wear in a physiologically representative manner.

To ensure that the femoral condyles and the polyethylene insert fit together naturally, some freedom of movement is required in the fixation of the tibia and femur. This freedom of movement will allow the two components to achieve full congruency without condylar lift-off, when load is applied through the joint.

Internal/external rotation of the tibia with respect to the femur is a necessity for physiologically representative testing as this rotation will change the location of contact between the femoral condyles and the polyethylene insert, thereby allowing for a greater surface of the polyethylene to be examined with mbRSA. Similarly, varus/valgus rotation of the femur as well as antero-posterior and medio-lateral motion between the TKA components will help facilitate bearing congruency. Precise measurement of motion is not needed as this motion would be performed clinically by patients, which cannot be precisely measured.

The support frame, fasteners, fixtures, and artificial bones of the physiological knee phantom must be able to withstand a knee force of 575 N in the standing position. As reported by D'Lima et al. 2006 [98], the force experienced by one knee during a two-legged stance is approximately equal to 1.3 times the externally applied force at the foot. Due to the variation in size and weight of TKA patients, an approximate average body mass of 90 kg (198 lb) was selected as this value represents an overweight (body mass

index > 25 kg/m^2), 183 cm (6') male patient. Accordingly, the externally applied force at the foot would be approximately half of the total body mass, 45 kg (99 lb). Therefore, the force applied through the knee joint is 58.5 kg (129 lb) or 575 N. This force does not account for the increase in knee force during flexion, which is reportedly between two to three times the body weight of the individual [99].

Knee force when in sitting in a chair is a result of the mass of the thigh as well as passive tension in the ligaments and muscles surrounding the knee (muscle tone). The approximate knee force in this position was measured as 32.6% (SD: 26.3%) of the patient's body weight (pers. comm. Dr. Darryl D'Lima, Scripps Clinic, La Jolla, CA). Using the same body mass described above, the force through the knee in a passive sitting position is approximately 29 kg (64 lb).

Validation of the developed technique for measuring polyethylene wear is best performed using previously worn polyethylene bearings obtained from explanted prostheses or from knee simulator wear trials. The wear that has occurred on these bearings is representative of true *in vivo* wear, and they are therefore an excellent method of clinical validation. Accordingly, the pre-worn polyethylene tibial inserts must be interchangeable to allow for multiple trials of differently worn bearings. The tibial tray must also be accessible for removal and insertion of different polyethylene bearings.

2.2.3 Preliminary Design

In an effort to remain cost effective, the initially proposed design of the TKA phantom was an attempt to fulfill the requirements of all three stages of testing. The decision was made to mount the artificial knee in an upright (standing) position in order to achieve all

desired angles of radiographs. This meant that the support structure for the phantom had to provide vertical support for the joint components and still remain rigid. A conceptual design was created in AutoCAD 2012 (AutoDesk Inc., Lake Oswego, OR) (Figure 9). The initial design was focussed on modularity, where portions of the phantom frame could be removed or added for the various stages of testing. Since the walls of the phantom frame would be visible in the radiographs, a 1" thick acrylic plastic was selected, as it is both rigid and relatively radiolucent. As well, nylon fasteners were selected for the wall joints, in order to maintain modularity of the frame as well as radiolucency.

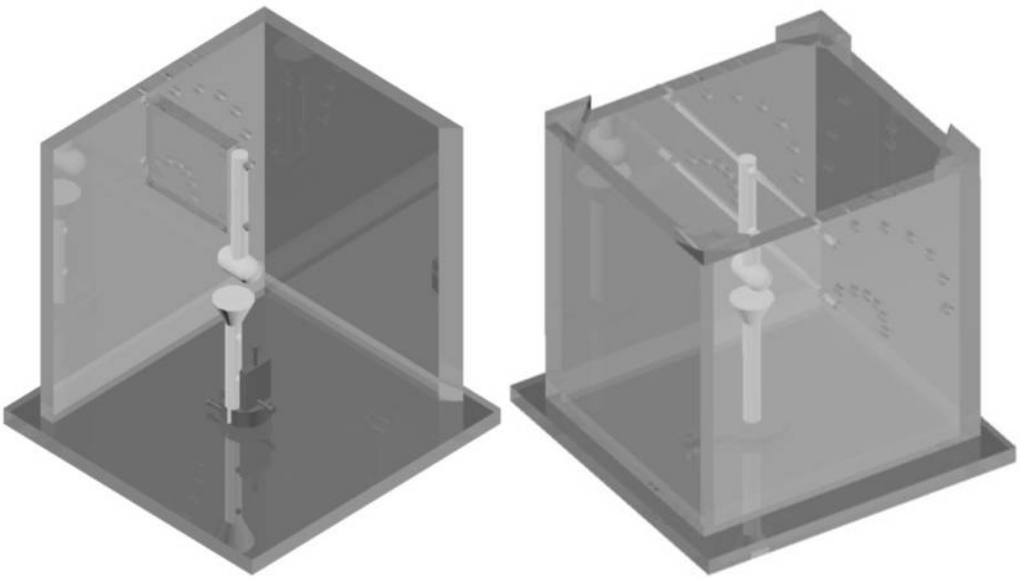

Figure 9: A) Preliminary accuracy phantom design, B) Preliminary physiological phantom design.

The precision stage of testing required rigid mounting of the Sawbones tibia and femur. Accordingly, the femur was to be fixed to the frame using a lateral mount (Figure 9A), whereas the tibia was to be fixed to the base of the frame. Flexion of the joint was to be accomplished using a series of concentric mounting holes drilled in the lateral wall of the support frame, thus allowing the flexion of the femur to match the rotational center of

the femoral condyles. These mounting holes were designed to be spaced at 15° intervals from full extension (0°) to 90° flexion.

The requirements of the accuracy testing stage are very similar to those of the precision stage, with the exception that linear translation stages (Parker Hannifin Corp., Cleveland, OH) were selected to induce the specified displacements. The translation stages were to be mountable at the base of the support frame and at the distal end of the tibia such that they would not be visible in the RSA radiographs (Figure 9A). The base of the support frame was designed such that the stages could be mounted in all directions thereby enabling X, Y, and Z directional displacements. Finally, a rotation table was selected to provide the necessary rotational displacement. The rotation table was to be mounted at the base of the support frame such that X, Y, and Z rotations could be achieved with only minor alteration to the mounting configuration of the rotation table.

For the physiological testing stage (Figure 9B), a number of adjustments were designed into the support frame and the movement equipment was changed. Two additional acrylic walls were to be added to the phantom support frame to provide the support of the loaded femur and tibia. A second set of concentric flexion mounting holes was to be included in the medial wall of the support frame such that two acrylic plastic rods could position the femur at the desired flexion angle. The translation and rotation stages were to be replaced with more robust positioning equipment; an acrylic rotation plate mounted to the base to facilitate internal/external rotation of the tibia, along with a cross-slide vice to facilitate antero-posterior and medio-lateral positioning of the tibia. High-tension rubber straps were chosen to apply the loading force to the knee joint. Four rubber straps were intended to apply loading force on the anterior, posterior, medial, and lateral sides of the

knee joint. The straps were designed to be fixed to the proximal end of the femur and stretch past the knee joint to 4 hooks embedded into the distal tibia.

2.2.4 Design Refinements

The efficacy of both phantom frames described above, required that the acrylic support walls were highly radiolucent such that little x-ray attenuation would occur during testing. Accordingly, the radio-opacity of 1” thick acrylic sheet was determined by obtaining radiographs of some sample blocks of acrylic (Figure 10). The x-ray attenuation was much greater than expected and as a result, it was decided that the artificial knee replacement had to stand alone, without an acrylic backing. To solve this issue, a complete re-design was undertaken to remove all acrylic plastic from the x-ray space.

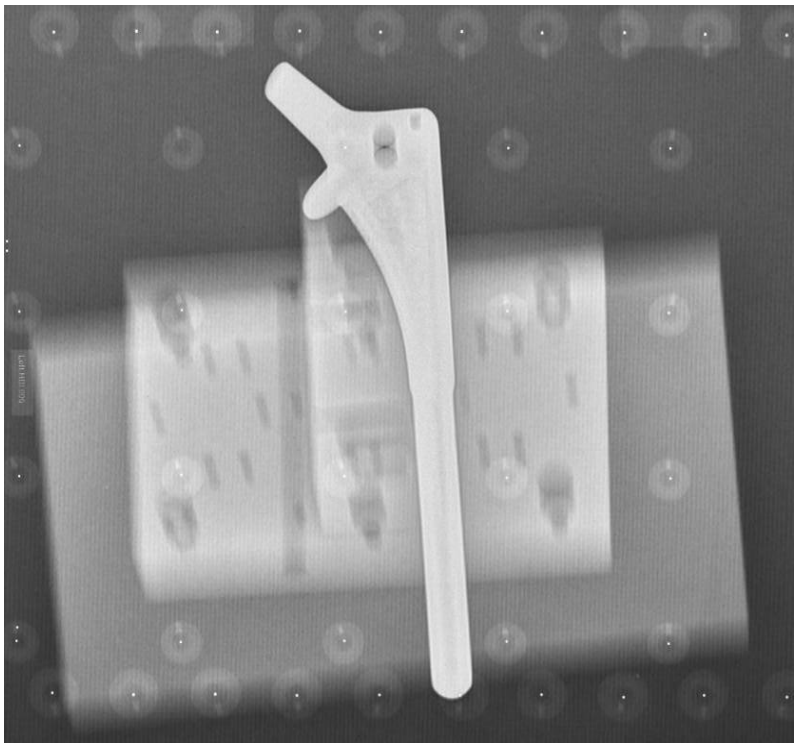

Figure 10: RSA radiograph of stacked blocks of 1” thick acrylic overlaid with a stainless steel femoral hip replacement stem (to represent the metal TKR components).

The artificial knee replacement components remained in an upright position, as previously decided. However, the support frame was designed to hold the leg bones from the top and bottom without a front or rear sheet of acrylic (Figure 11). Dual vertical support posts were positioned on each side of the phantom joining a rigid top and bottom plate, which were the mounting platforms for the artificial knee joint components. Flexion of the knee was facilitated using angled “flexion” blocks cut to 0°, 45° and 90° angles. Orientation of the knee with respect to the x-ray equipment was changed by simply rotating the tibia and femur by 30°, 60° and 90° degrees; the phantom support frame remains stationary.

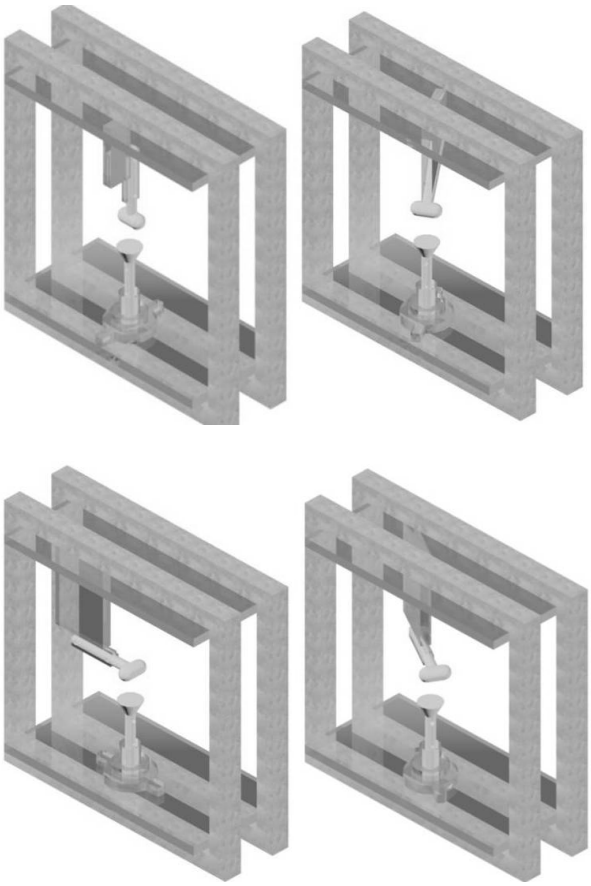

Figure 11: Final conceptual design of the phantom showing the four testing orientations and three flexion angles. Frame posts shown as steel, top and base plates shown as acrylic.

The flexion blocks were designed to bolt directly to the top-plate of the frame and to the shaft of the femur for rigidity. Acrylic plastic was again the material of choice for these flexion blocks as they would be partially visible in the radiographs. The Genesis II total knee replacement components were to be mounted to a Sawbones (Pacific Research Laboratories, Vashon, WA) femur and tibia. The Solid Cortical Shell Sawbones were selected as they are the recommended material for artificial prosthesis implantation. The Genesis II components were fixed to the Sawbones as described in Section 2.4.

Physiological Phantom

Despite the simplicity of the tension strap loading system, no simple method was available for measuring the compressive force on the knee joint. As well, four rubber straps were unable to provide a physiological loading force of up to 90 kg. Therefore, an external mechanical loading mechanism was needed to apply the required compressive force. Because the femur undergoes flexion, application of the force from the tibia was much more feasible since the tibia remains vertical for all tests. It was decided that a load frame would be required to apply the required physiological loads. A Chatillon ET-1100RS2 instrumented load frame (John Chatillon & Sons, New York, NY) was selected to be the physiological phantom support frame. The Chatillon frame is ideal as it is small enough that it is reasonably portable. This was important as it needed to be moved to the Concordia Hip & Knee Insitute x-ray suite. Additionally, the load frame provided sufficient space to allow RSA x-rays to pass though the frame without being blocked.

This load frame is ideal for physiological loading as it is a fully instrumented with a load and displacement display and is available with two load cells; a 100 lb_f load cell (U62-100-0506, John Chatillon & Sons, New York, NY), and a 1000 lb_f load cell (U62,1K-0506, John Chatillon & Sons, New York, NY). The load cell is fixed to the top of the load frame which, for accurate load measurement, required that force be applied vertically with minimal shear forces. For this reason, the Sawbones were designed to be inverted with the tibia fixed to the load cell and the femur fixed to the moving base plate of the load frame.

For the physiological phantom, it is crucial that full contact be achieved between the femoral condyles and the surface of the tibial insert, as this contact is used to determine

polyethylene wear. To ensure this contact, the bone mounts are required to have some freedom of movement. In the standing position, both varus/valgus and internal/external rotations must be available to ensure complete contact (Figure 12). In the sitting and 45° flexion position, internal/external rotation of both the tibia and of the femur must be available (Figure 12). To accomplish these degrees of freedom, it was decided that multiple bone mounts were required. To withstand the loading force, the bone mounts were designed using steel plate and box beam. The mounts were also designed to avoid interference or overlap relative to the metal TKA components as steel mounts are radio-opaque.

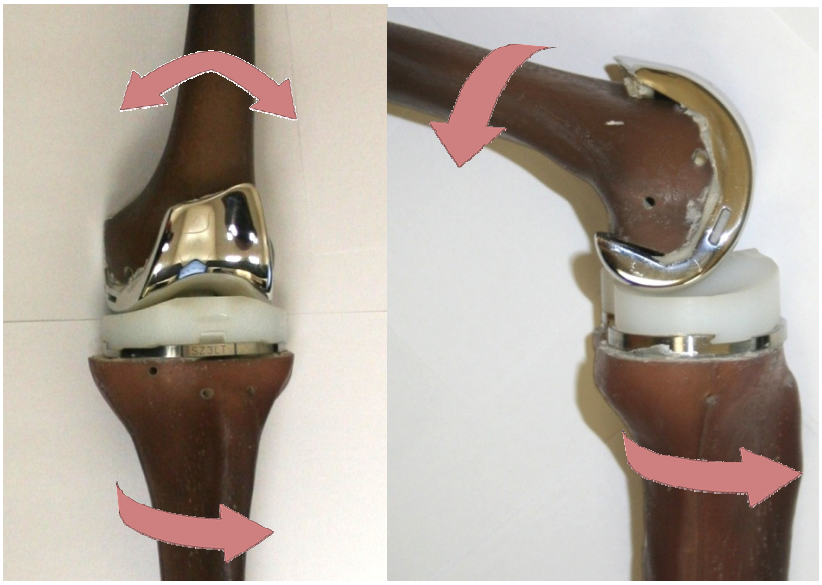

Figure 12: A) 0° flexion of the artificial knee showing internal/external rotation of the tibia and varus/valgus rotation of the femur. B) 90° flexion showing internal/external rotation of the tibia and femur.

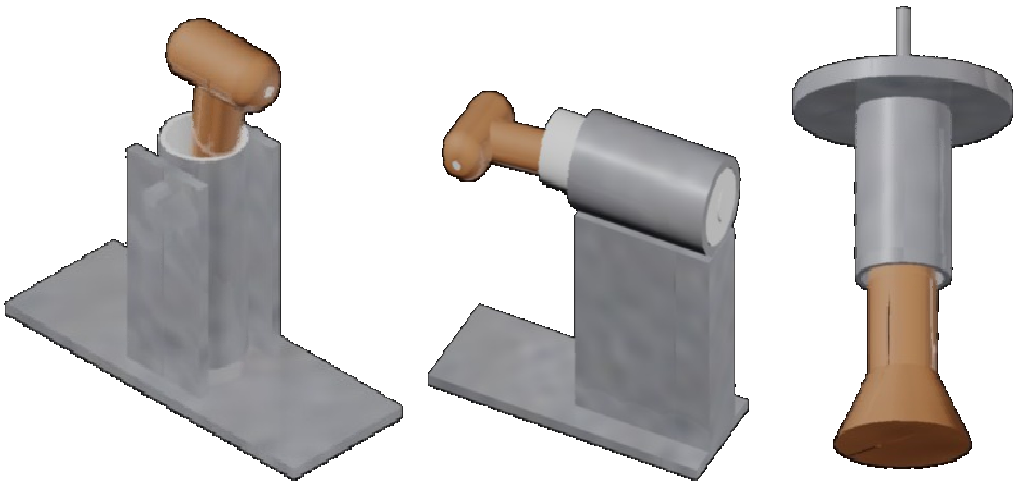

Figure 13: AutoCAD renderings of the physiological phantom bone mounts; A) inverted tibia mount with bolt matching that of the load cell, B) standing femur mount with high-pivot, C) sitting femur mount (cylinder inside a cylinder).

The simulated femur was designed to be embeddable into a steel tube with the remaining space being filled with epoxy resin. For the standing flexion cases, the embedded femur was designed with a pivot point located as close to the TKA component as possible in order to achieve varus/valgus rotation while simultaneously supporting the full loading force without the mount buckling (Figure 13A). For the flexed case(s), the femur mount was designed as a cylinder inside of a cylinder to allow for internal/external rotation of the femur and still provide support under load (Figure 13B). Similar to the femur, the tibia was embedded in a steel tube filled with epoxy resin, but was fixed to a circular base (Figure 13C). A 3/8” fine thread bolt was welded to the center of the circular base to allow the mount to mate with the 100 lb_f load cell. The design achieves an internal/external rotation of the tibia by allowing rotation of the load cell (with tibia attached) with respect to the load frame.

2.3 Reverse engineering of implant models

2.3.1 Three-dimensional laser scanning

A ShapeGrabber SG102b 3D laser scanner (ShapeGrabber Inc., Ottawa, ON) was used to scan the tibial and femoral components as well as the tibial insert. The ShapeGrabber obtains a highly accurate 3-dimensional scan of an object by recording the reflection of a low-intensity laser beam off the object. It is also fitted with a high precision automated rotation table which allows the user to obtain multiple scans of all sides of the object in a single run. The ShapeGrabber collects the reflected laser beam and stores it as individual object points, known as a point-cloud.

The y-axis (vertical axis) resolution of the ShapeGrabber was set at 0.05 mm for all scans. Due to the highly reflective surfaces of both the tibial tray and the femoral condyles, both components were coated with Spotcheck Developer spray (Magnaflux, Glenview, IL). Coating was applied at a minimum distance of 30 cm in multiple passes. The spray was allowed to develop for a minimum of 5 minutes before the component was scanned (Figure 14A). Sticky-tac adhesive clay was used for most scans to help position and hold the components to the rotation table of the ShapeGrabber (Figure 14B).

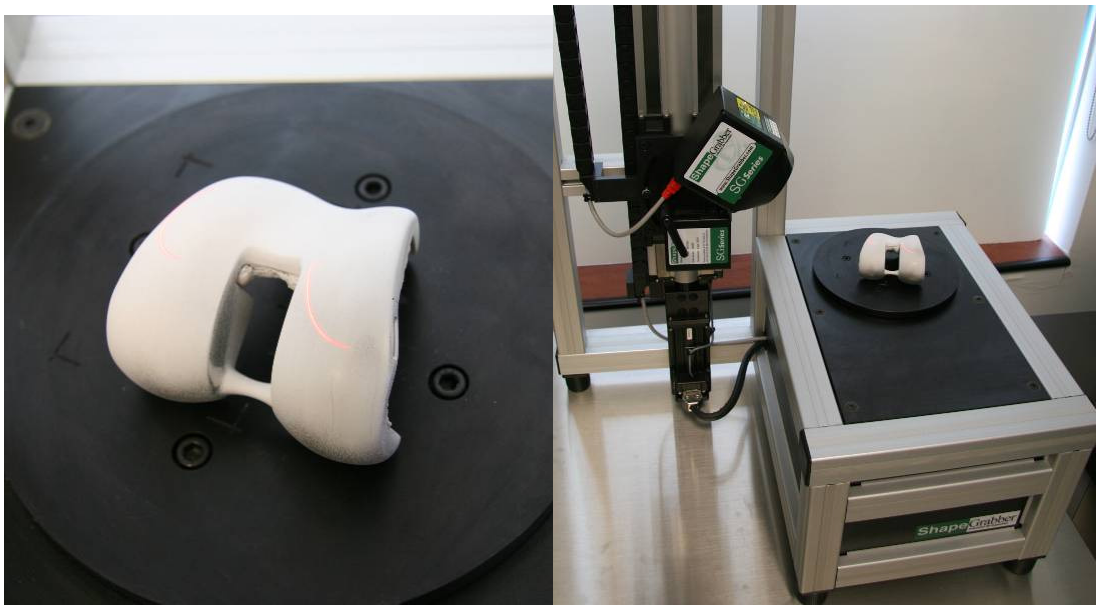

Figure 14: A) Femoral condyles coated in developer spray. B) Laser scanning setup with ShapeGrabber.

Five scans were performed on the femoral component, with three scans of the entire object at 6 to 12 rotational intervals in order to obtain the exterior surface of the condyles and the majority of the interior backside surface features. Two additional scans were performed to obtain the anterior face of the inter-condylar box, as this was not obtained on the previous three scans.

Six separate scans were performed on the tibial tray. Three scans were performed of the entire object, using 10-12 rotational intervals with the tray at different orientations. The remaining three scans were of the tray's top surface and edges where finer detail was required of the peripheral locking mechanism and the exterior edge of the tray.

Three scans were performed on the polyethylene tibial insert at 10-12 rotational intervals. No additional scans were required as the exterior surface detail of this component was minimal. The tibial insert was also coated in developer spray in order to prevent the

scanning laser from penetrating into the polyethylene surface, as this would affect the dimensions of the insert.

2.3.2 Model Re-construction

Geomagic Studio version 12 (Research Triangle Park, NC), was used to reconstruct the 3-dimensional scans into full computer models. Most object scans were imported into Geomagic Studio with a laser angle exclusion criterion of 75°, which prevents erroneous, high-angle laser reflections from being imported into the object space. One set of scans entails all of the scans of the object with one particular position, but at all 10-12 rotational angles. Each set of scans was cleaned for unwanted laser reflections and extraneous points by manual user selection, as well as built-in tools; outlier removal (selects all points which are statistical outliers of the true surface), and disconnected points (selects all clusters of points which are well separated from the true object).

Once all of the individual sets of scans were imported into Geomagic Studio, the scans were aligned with 9-point user-selected keypoint alignment (Figure 15). Careful selection of common points between the various sets of scans ensured that high accuracy was maintained in the final, compiled model. Once 9 common points were selected, an automated registration algorithm performed the final alignment of each set of scans. If the automated alignment did not perform correctly (uneven distribution of points between the two sets of scans across a common surface), the registration was rejected and the process was restarted.

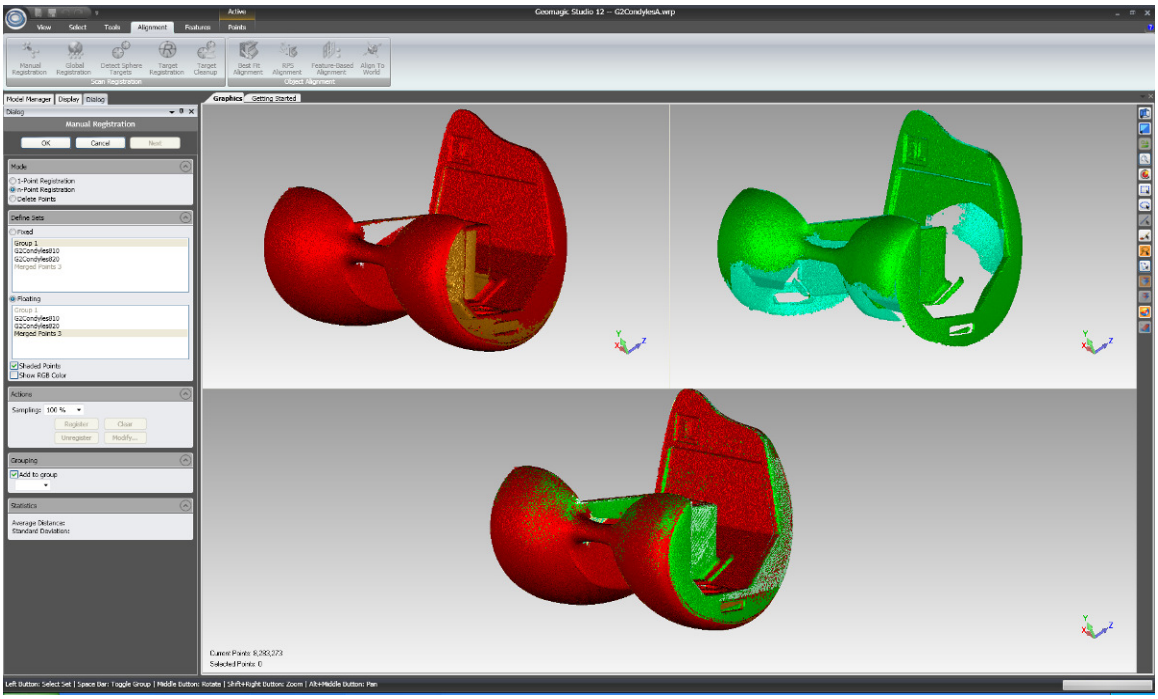

Figure 15: 9-point registration of a group of scans (red condyles) with an additional scan (green condyles), and the resulting overlay (lower object).

Due to the high y-axis precision of 0.05 mm, and the number of 3D scans that were combined to construct the model, there was often too much data (between 4 and 10 million individual points) to be handled properly by Geomagic Studio. Geomagic's curvature sampling algorithm was used to reduce the number of object points down to a manageable number (approximately 1 million points). Curvature algorithms increase the sampling priority along curved surfaces and around sharp edges thereby preserving the original exterior geometry of the object. The remaining object points were then merged into one object and wrapped into a large polygon mesh consisting of approximately 2 million triangular elements.

Cleaning and refinement of the mesh object began by filling the large holes in the mesh. In the case of the tibial tray, the concave surface of the peripheral locking system

had a substantial hole that was filled using the curvature-fill setting, which fills a hole based on the curvature of the surrounding surfaces. In the case of the femoral condyles, the interior faces of the inter-condyle box also had substantial holes that were filled with the flat-fill setting, which fills a hole with a planar mesh surface. Some holes did not fill correctly, so a manual bridging function was used to divide the complex holes into more manageable holes that were subsequently filled using the case appropriate curvature- or flat-fill settings. Geomagic Studio's automatic tools were used to fill the remaining small holes.

Once the object was fully surfaced (all holes filled), various other algorithms provided within Geomagic Studio were used to clean the triangle mesh. Removal of spikes in the mesh (triangle elements at sharp angles to each other) was performed to improve the smoothness of the object. All non-manifold edges (i.e., edges with no clear "inside/outside" directions) were repaired using the Mesh Doctor function of the software, as well as remeshing to remove high internal angles in triangle elements, and other irregularities in the object surface (Figure 16).

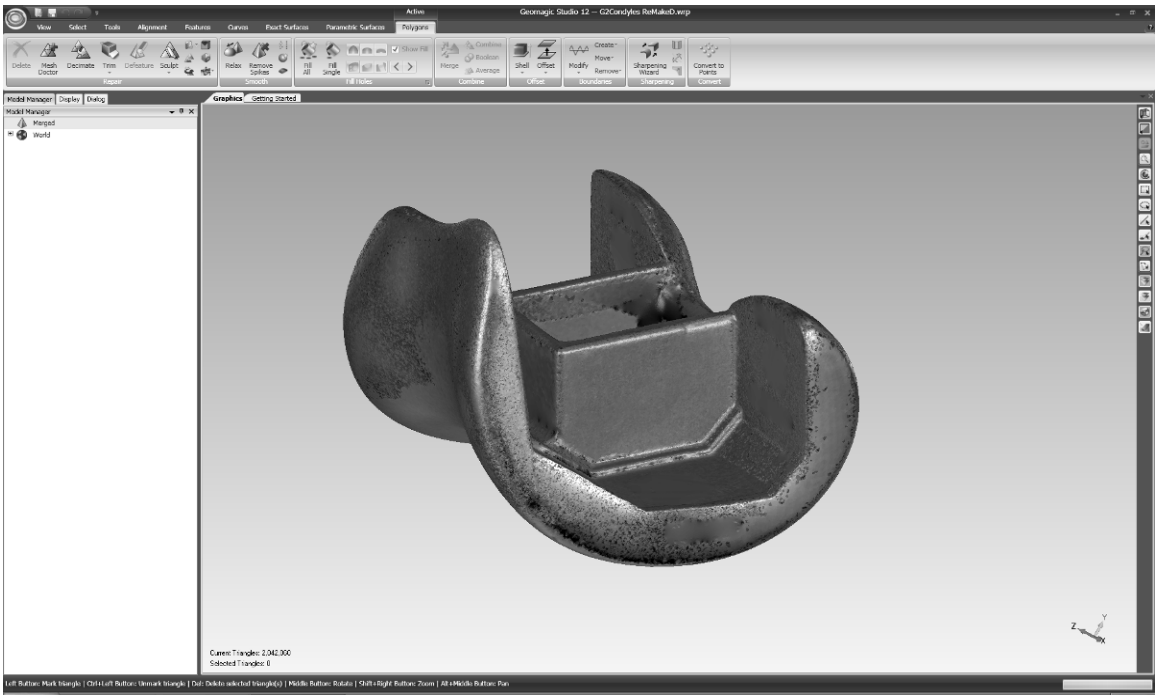

Figure 16: Final reconstructed model of the femoral component consisting of ~2 million mesh elements.

The final step in the model reconstruction process was to reduce the number of mesh elements down to the recommended number for model-based RSA; 5000 elements. The decimate function of Geomagic Studio was used to reduce the 1~2 million element mesh down to 5000 elements. Two sets of implant models were created in order to test how different software settings can affect model reconstruction. The first set, known as the 'Original Models', were decimated using the default settings of Geomagic's decimate function. The settings used were medium mesh priority (triangle elements should be almost equal-sized) and medium curvature priority (distribution of triangular elements over the whole model surface is skewed to favour curvature). The second set, known as the 'Revised Models' were decimated using the following settings; low mesh priority (allows for high variation in mesh element size), high curvature priority (large skew towards ele-

ments at edges and curves), and fixed boundaries (exterior dimensions fixed). These settings were chosen in an attempt to obtain an object model with a high density of elements at the edges and curved areas while maintaining the external dimensions as much as possible.

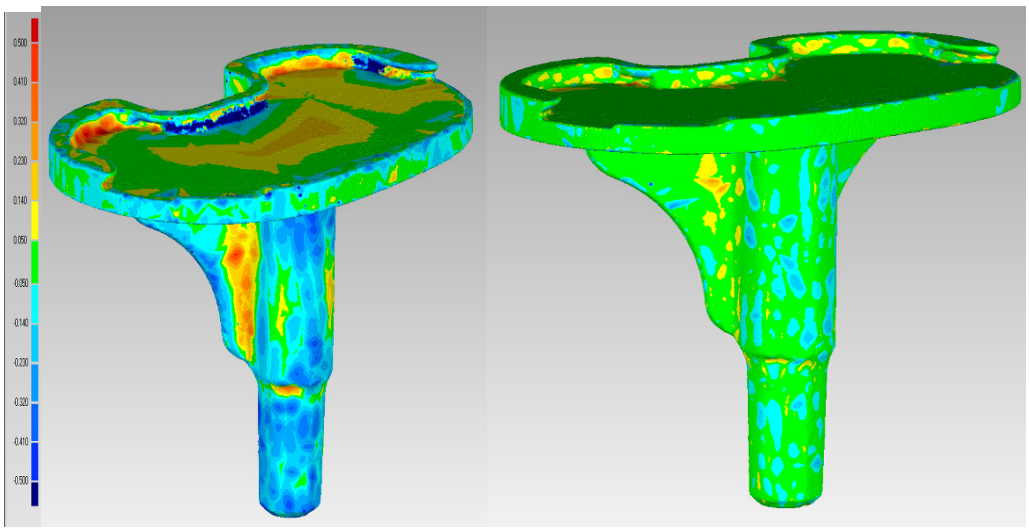

Figure 17: Comparison of the A) “original”, and B) “revised” tibial tray models, with their respective 1,000,000 element models. Colour scale units are in millimetres, the 1,000,000 element model is the reference.

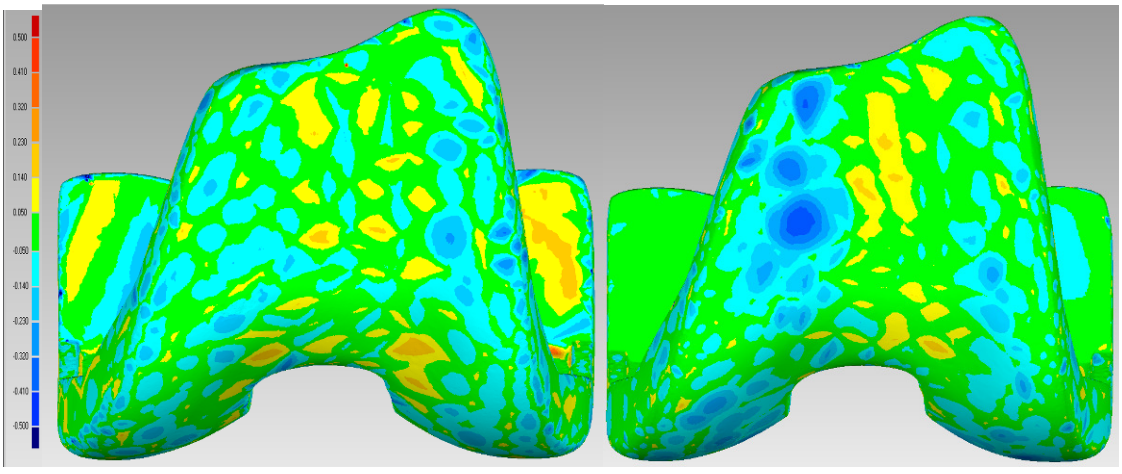

Figure 18: Comparison of the A) “original”, and B) “revised” femoral condyle models, with their respective 1,000,000 element models. Colour scale units are in millimetres, the 1,000,000 element model is the reference.

Verification of the accuracy of the decimated implant models was performed using the deviation analysis tool in the Geomagic Studio software. The 5000 element models of both the original and revised femoral and tibial components were aligned with a ~1 million element model using the same 9-point registration technique, and compared using the deviation analysis tool (Figure 17 and Figure 18).

The original tibial tray model showed substantial negative deviations in the post and fin compared to its high resolution counterpart. However, the revised tibial tray showed excellent dimensional agreement with only small inaccuracies at select points on the post and rim of the tray. The femoral component models showed a fair amount of deviation compared to the 1 million element reference, particularly on the curved surface of the condyles. However, these deviations are a result of the large size of mesh elements. The effect of selecting greater curvature priority in Geomagic Studio can be seen in the edges of the revised model, which have somewhat less deviation than the edges in the original model.

Upon approval of the above TKA models, the 5000 element versions were then exported as stereolithography (STL) files, which were then transferred to Medis Specials (Leiden, The Netherlands). The engineers at Medis then applied a model-repair algorithm to repair any remaining shells (non-closed sections) and inverse normals (inwards-facing elements). The center of mass of each model was centered on a pre-selected global coordinate system, with the x axis corresponding with the medio-lateral axis of the implant, the y axis with the superior-inferior axis, and the z axis with the antero-posterior axis. The left-sided implant scans were then mirrored about the Y-Z plane in order to convert them to right-sided; as is required by mbRSA. A final STL version (repaired, centered) as

well as a converted mbRSA model file (MBM file) of each model was the received from Medis Specials electronically.

2.3.3 Polyethylene Insert Scanning

As an unworn reference for the wear computations performed in Chapter 4, a new Genesis II size 3 PS tibial insert (13 mm thickness) as well as 5 retrieved tibial inserts of the same thickness were scanned in the same manner as the tibial tray and femoral condyles. Developer spray was applied to all surfaces of the inserts to prevent penetration of the laser into the polyethylene, which would result in a dimensional difference. The y-axis resolution of the scanner was set to 0.1 mm for all scans. Two scanning runs, each consisting of 18 increments of 20°, were imported into Geomagic Studio, cleaned of extraneous points, aligned and converted into a solid mesh object. Any holes in the mesh surface were closed using the automated filling tool in Geomagic Studio, and the models were decimated to 100,000 elements in order to be manageable while remaining dimensionally accurate. Because of the errors encountered with the “revised” models described in Section 6.1, the mesh and curvature priorities were kept at the default setting of medium and the Fix Boundaries option was off for the decimation process.

2.4 Implantation of TKA Components

2.4.1 Solid-foam Sawbones

For the first two stages of analysis, the Genesis 2 total knee replacement components were implanted onto solid-foam Sawbones. The necessary implantation tools, jigs, and implements were obtained from Smith & Nephew as part of a Sawbones practice kit.

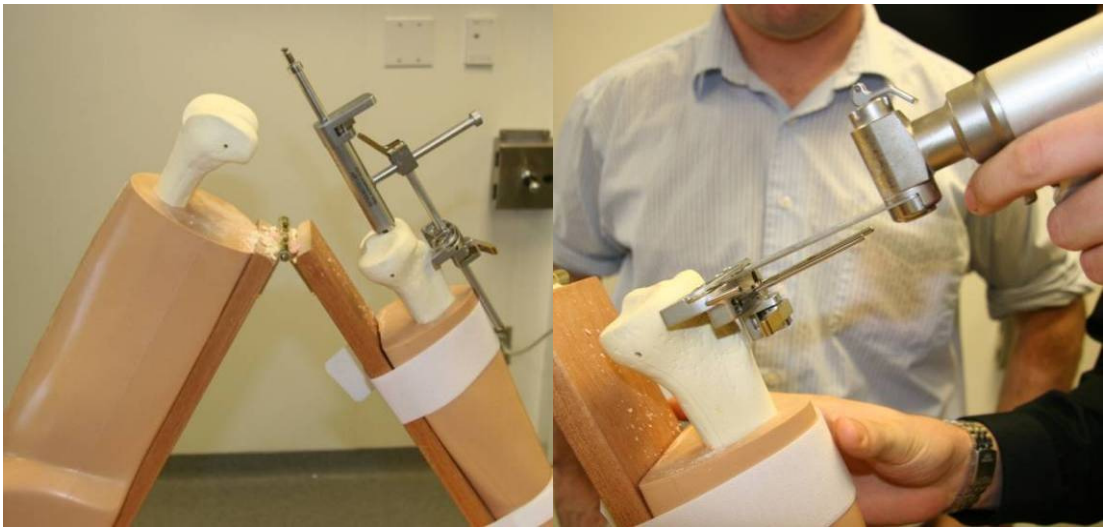

Figure 19: A) Sawbones implantation jig, with S&N alignment tool fixed to the artificial tibia. B) Proximal tibial cut using a reciprocating saw.

The first step of implantation was to mount the artificial tibia and femur into the rubber leg jig, simulating human flesh. The jig is designed such that the knee can be held in a highly flexed position, necessary for surgical implantation (Figure 19A). An alignment tool for the tibia was used to properly align the cutting block for the tibia. A reciprocating blade saw was then used to cut off the proximal surface of the tibia (Figure 19B). A dovetail punch was then used to indent the inner material of the artificial bone to provide space for the fins of the tibial tray.

The femoral alignment tool was temporarily fixed to the distal artificial femur using three surgical pins. It was decided that the size medium femur was too large for the size 3 femoral component, however, it was the only size of Sawbone that was available for this research. For this reason, the femoral cuts were referenced from the anterior face of the femur (Figure 20A), such that the majority of artificial bone was cut away from the posterior condyles. Using the same reciprocating saw, an anterior cut was made into the Sawbones femur. Special care was taken to not create a notch in the anterior femur. The femoral cutting block was adjusted for a size 3 femoral component and the remaining 3 cuts were made (Figure 20B).

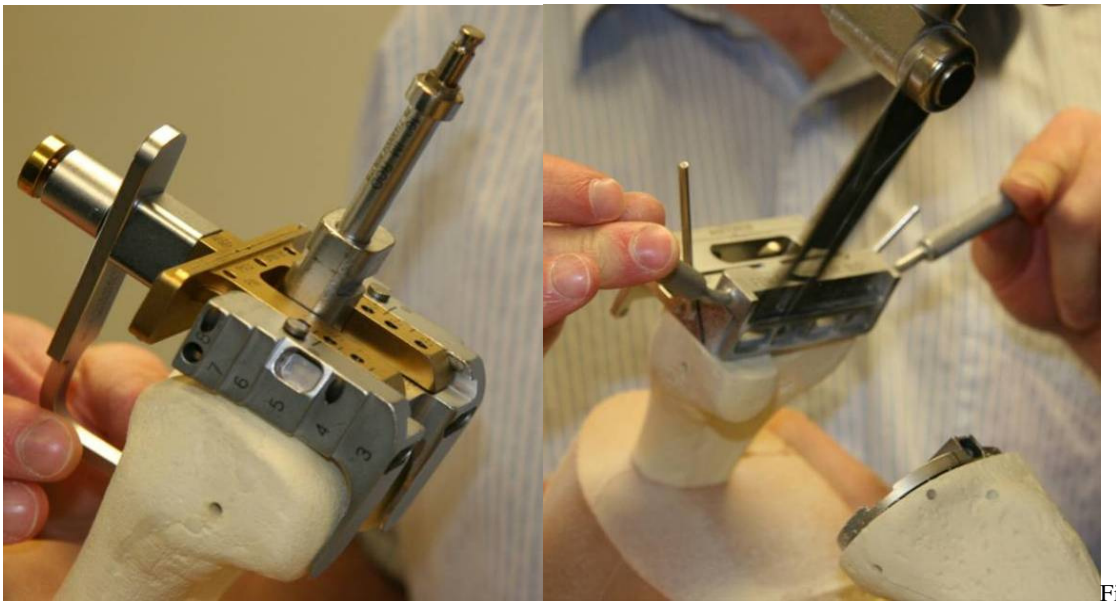

Figure 20: A) Anterior referencing of the femur. B) Distal femoral cuts using a reciprocating saw.

Sample sizing components were pressed onto the tibia and femur to examine the approximate fit of the true TKR components. Versabond (Smith & Nephew, Memphis, TN) bone cement was prepared and applied to the cut surfaces of the artificial bones as well as the TKR components (Figure 21A). The components were pressed onto the bones and pressure on the components was maintained for 5 minutes until the cement became rigid (Figure 21B).

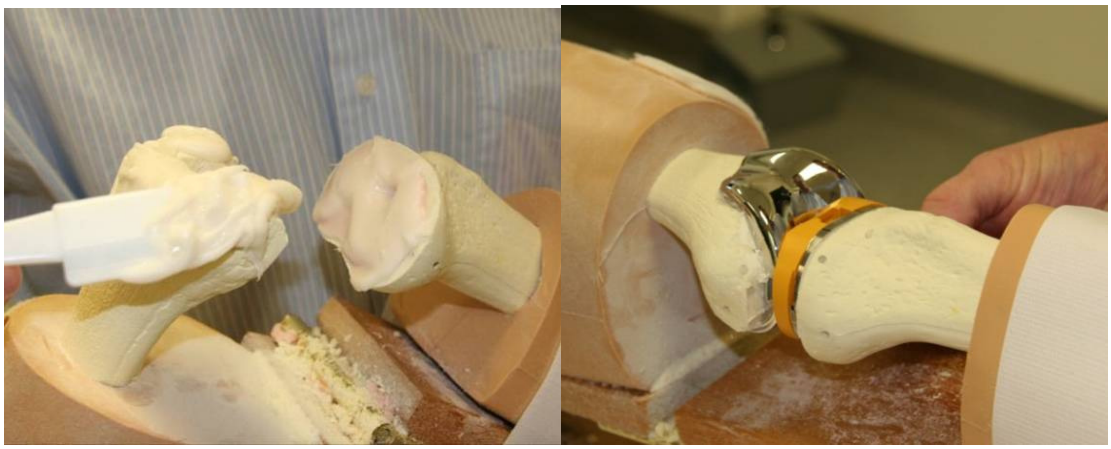

Figure 21: A) Application of Versabond bone cement. B) Pressurization of the TKR components.

The bone cement was allowed to cure for 24 hours to ensure the components were rigidly fixed to the Sawbones. A tantalum bead inserter (Halifax Biomedical) was used to insert 5 tantalum markers into the artificial bone surrounding the tibial post and 5 tantalum makers surrounding the femoral component (Figure 22).

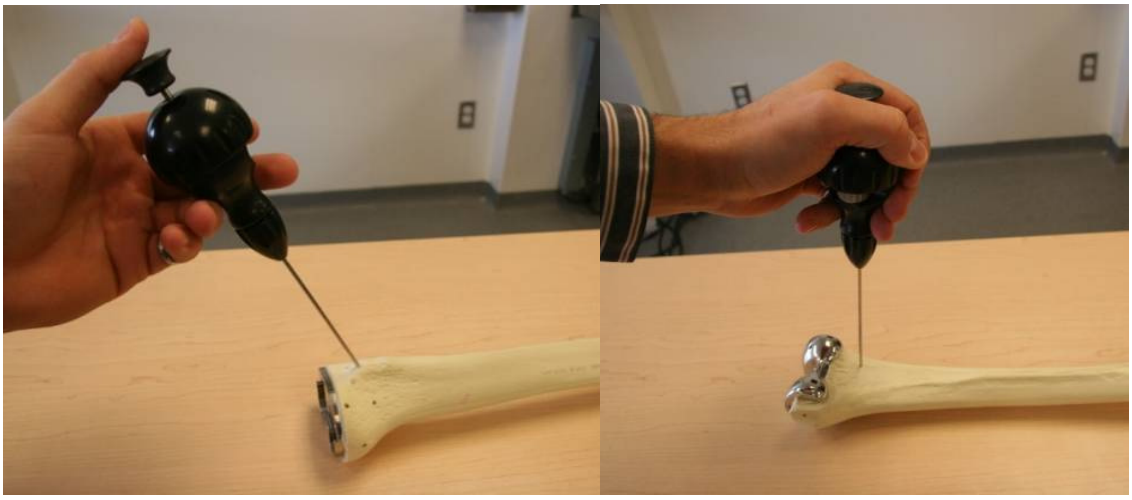

Figure 22: A) Insertion of tantalum markers into tibia. B) Insertion of tantalum markers into femur.

Since the TKA implantation equipment was on temporary loan from Smith & Nephew, it was decided that the necessary cuts should be made to the composite Sawbones (for the physiological phantom) at the same time. The cuts were performed using the same method and equipment as described above. A smaller size of the composite femur Sawbone was selected due to the size mismatch between the femoral TKA component and the solid foam Sawbone described in the previous section.

2.4.2 Composite Sawbones

The solid cortical foam Sawbones previously used were not suitable for the physiological phantom because of the applied load. Instead, Composite Sawbones were selected as they have similar strength to human bone and would therefore withstand the loading forces placed on the phantom model. The TKA components were removed from the solid-foam cortical bones using a drywall cutting drill bit. Once the bulk of the solid-foam bone was

removed, the acrylic bone cement was carefully hand-chipped away from the components using a small flat-blade screw driver and wood chisel.

Tantalum markers were not inserted into the composite bones as model-to-marker precision and accuracy was previously quantified in with the solid-foam Sawbones components. Versabond bone cement was used to fix the TKA components onto the composite Sawbones, as previously described.

2.5 Construction of Precision/Accuracy Phantom

The precision/accuracy phantom was constructed out of medium density fibreboard (MDF) in order to test out the dimensions, spacing, and overall design of the phantom. Due to time and budgetary constraints, it was decided that this MDF frame was sufficiently rigid for the precision and accuracy testing stages. The dimensions of the frame (Figure 23A) were such that the majority of the supporting fixtures for the Sawbones remained out of the visible x-ray space. The width and depth of the frame were selected such that the support posts would also not be visible in the x-ray space, but still provide support for the Sawbones in all orientations and flexion angles.

The support posts (vertical and horizontal) as well as the base and top plates were cut out of the MDF sheet using a table saw (Figure 23A). The components were fastened together using 2” wood screws, as radio-lucency was not a concern for the support frame. The mounting surface for the tibia was an acrylic block that was obtained from a previous RSA phantom, as this block already had numerous holes drilled and tapped for the at-

tachment of the micromanipulators. This block was also used as the rotation table for the tibia by fastening it to the MDF base plate with a single screw to act as a pivot point (Figure 23B). The shaft of the tibia was rigidly attached using two 3" hose clamps fastened tightly around a right-angle bracket that was bolted to the micromanipulators slides (Figure 23B).

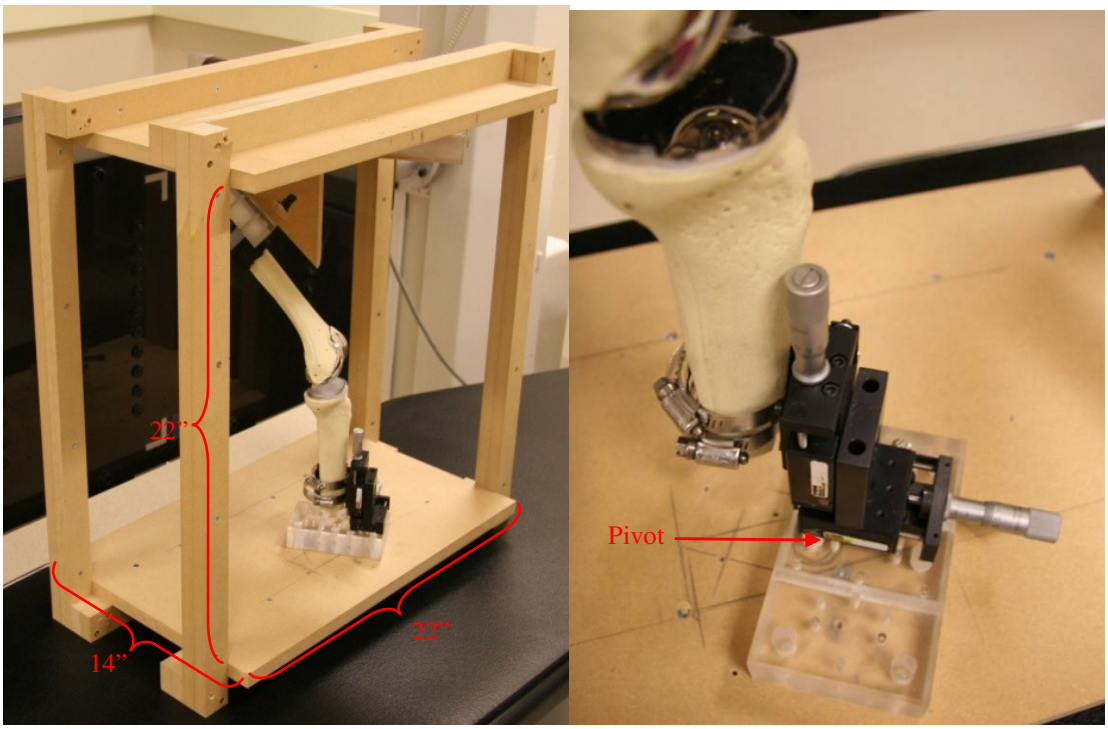

Figure 23: A) MDF phantom frame; B) Acrylic mounting block for the tibia, attached with hose clamps to the micromanipulators. A single fastening screw provides a rotational center (arrow).

The acrylic flexion blocks for the femur need to be rigidly fixed to the top-plate of the phantom while remaining adjustable for positioning with respect to the tibia. To accomplish this, a t-groove and t-bolt fastening system was designed by Dale Bourns and Robert Lavalee, of the Biosystems Engineering Machine Shop. The flexion blocks and

corresponding mounting blocks were designed out of acrylic to maintain radio-lucency. The t-groove system was constructed of 3 parts, a long rectangular top plate, three angled flexion blocks, and a backing plate that was fixed to the shaft of the femur. A t-groove was milled along the centerline of the rectangular top plate (Figure 24A). Corresponding "shoulders" that fit into the t-groove were milled along the top edge of each of the three flexion blocks. A t-shaped hole was milled into each of the flexion blocks to provide space for loosening and tightening of a locking bolt and t-nut. Three 2" nylon bolts were cut down to approximately 1" (for spacing requirements) and inserted into a hole that was drilled through the edge of each flexion block into the space of the t-shaped access hole. A set of t-nuts were milled out of a thin section of acrylic and were drilled and tapped to fit with the nylon locking bolt inserted into each flexion block (Figure 24B). This assembly allowed the flexion blocks to slide along the t-groove in the acrylic top-plate and to be rigidly fixed at the desired position using the t-nut and bolt combination.

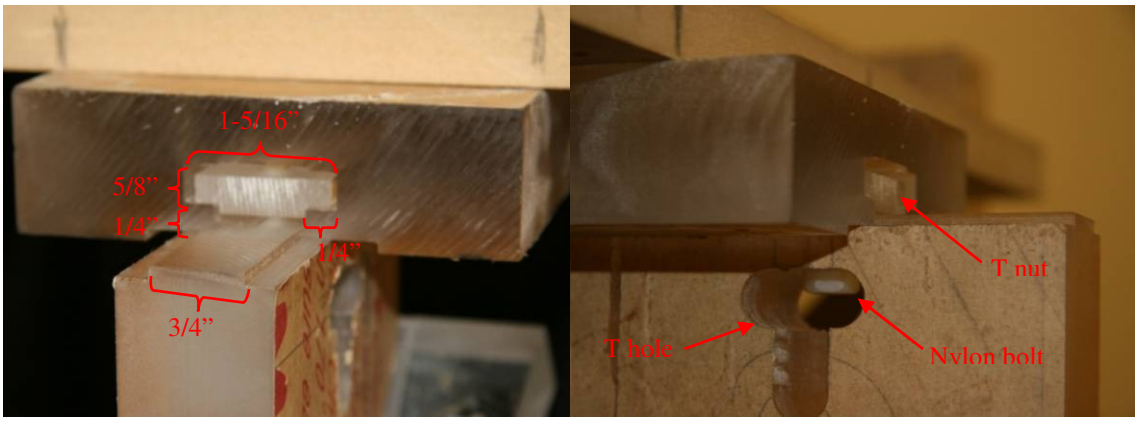

Figure 24: A) T-groove and corresponding "shoulders" dimensions. B) T-shaped hole in flexion block, nylon tightening bolt, t-nut.

The backing plate for the femur was cut in the shape of a parallelogram, with the long sides being approximately 10° off right angle to account for the angle of the femoral shaft with respect to the femoral condyles (Figure 25A). Six holes were drilled and tapped into the backing plate in order to fasten the shaft of the femur using three polyvinylchloride (PVC) conduit clamps (Figure 25B). Polyethylene pipe insulation was added to the shaft of the femur to improve the stability of the mount. The backing plate was fastened to the flexion blocks using the same t-groove and locking system as described above. A t-groove was milled down the backside of the backing plate, "shoulders" were milled into the corresponding edges of the flexion blocks, and the necessary holes were drilled and tapped for the t-nut and locking bolt system. As a whole, this dual t-groove system allowed for forward/backward and up/down freedom of movement for the femur, while still being a rigid support system when everything was tightened (Figure 26A).

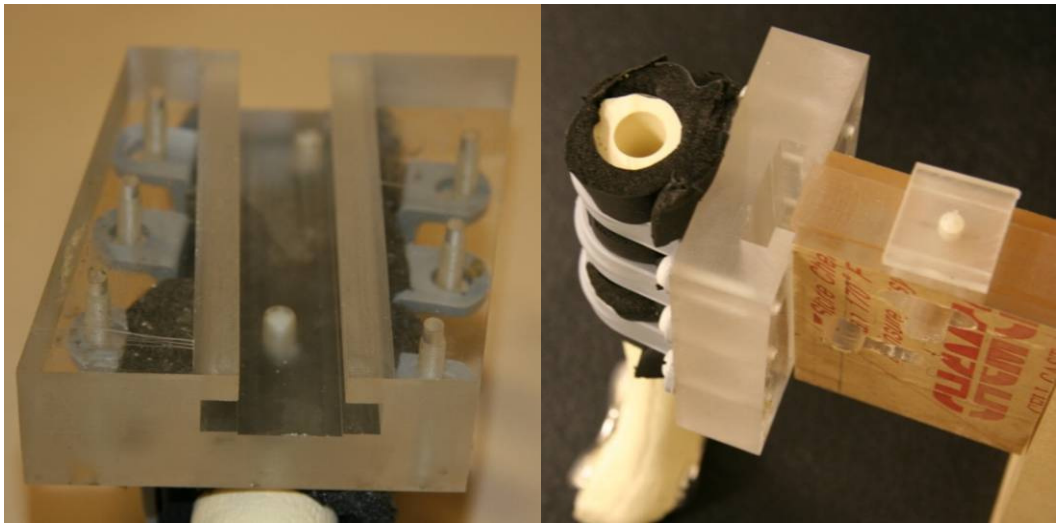

Figure 25: A) Femoral shaft fixed to the angled backing plate with 3 PVC conduit clamps. B) T-groove milled into backside of the backing plate.

The acrylic top-plate was mounted to the MDF top-plate such that it could rotate concentrically with the rotational center of the tibia (on the base-plate) to allow the leg bones to align properly at all imaging orientations (Figure 26B).

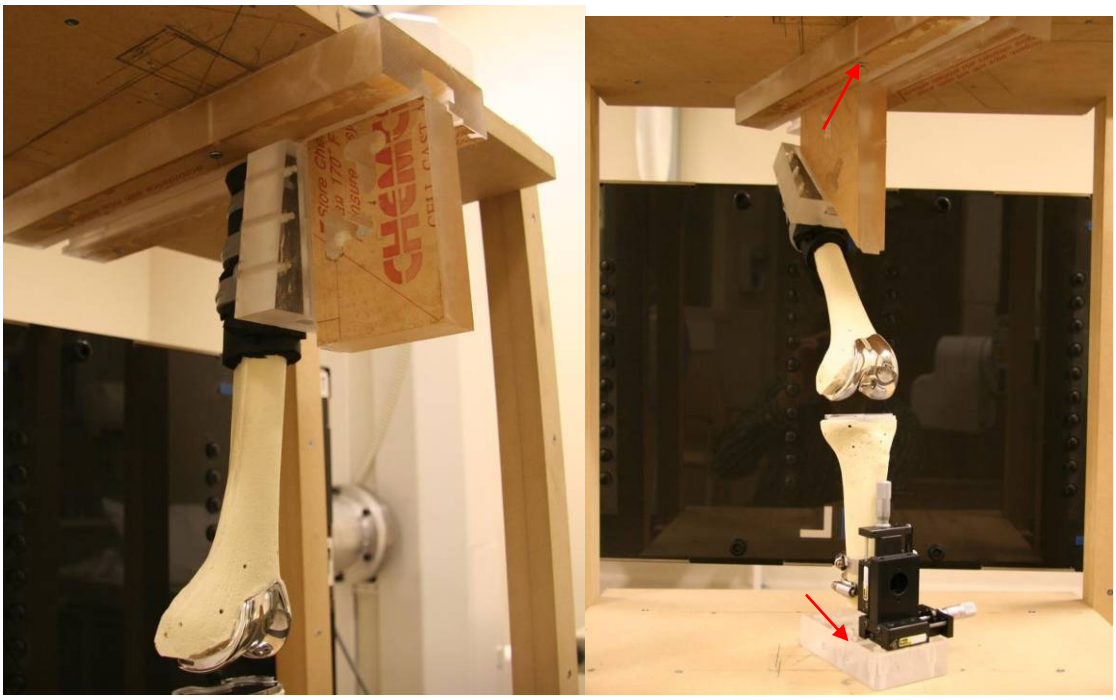

Figure 26: A) Assembled t-groove locking system. B) Top and bottom acrylic blocks fastened with common pivot point (arrows).

Once the RSA phantom was constructed and all components were installed, a number of modifications were made to improve rigidity of the frame and the bone mounts. After performing an initial run of precision RSA x-rays, it was discovered that the wooden phantom frame was not as rigid as was required. To remedy this issue, four right-angle brackets were fastened to opposing corners on the base of the frame (2 brackets) and on the top of the frame (2 brackets), as shown in Figure 27A. Additionally, two wooden braces were added to each side of the frame, between the vertical posts to prevent fore and backward flexing of the frame. These additions were constructed from MDF and fas-

tened to the frame with wood glue and 2” wood screws. The improvement was substantial with no visibly detectable movement (base relative to top) under a physical load.

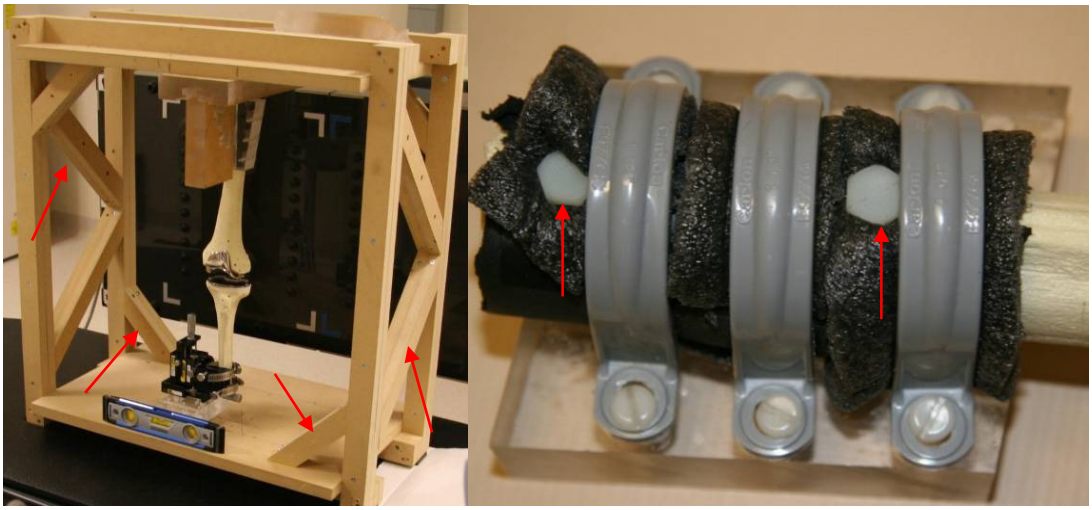

Figure 27: A) Corner braces and post-braces installed on the RSA phantom frame (arrows). B) Two nylon bolts added to the femur mount to improve rigidity (arrows).

The method of fixing the femur to the acrylic mounting block was also found to be insufficient, as vibrations resulting from movement of the x-ray table caused measureable movements of the femur. The rubberized plastic (polyethylene) foam pipe insulation did not hold the femur sufficiently rigid and thus, two 2” nylon bolts were added to the femur mounting block (Figure 27B). The bolts were passed through the shaft of the femur and were threaded into the acrylic mounting block and fastened tightly to ensure no movement of the femur.

2.6 Construction of Physiological Phantom

The bone mounts for the physiological phantom were constructed out of steel to withstand the required loading forces. The Sawbones tibia was cut approximately 7” from the proximal surface using a band saw. The proximal section of the tibia was then mounted inside the cylindrical section of the tibia bone mount using high-strength epoxy resin (Loctite 9460 Hysol Epoxy, Henkel Corporation, Düsseldorf, Germany) (Figure 28).

Figure 28: Tibia bone mount with the proximal section of the Sawbones tibia inserted.

The Sawbones femur was cut approximately 8” from the distal surface (condyles) using a band saw. The distal section was then mounted inside the cylindrical femur bone mount using epoxy resin. After the epoxy had set, a ½” hole was drilled through this assembly 1” from the distal edge of the cylinder to act as the varus/valgus pivot point. The standing bone mount was constructed from 3/8” thick steel plate. A ½” hole was drilled into each of the uprights (Figure 29A) which were then welded to the base-plate. The positioning holes were milled out larger than initially specified to allow for more freedom in positioning. A ½” diameter steel rod was inserted through the uprights and the bone-

mount assembly to serve as the varus/valgus pivot. Both ends of the pivot rod were drilled and tapped to fit ¼" Allen bolts, which with washers, held the pivot bar in place (Figure 29B).

Figure 29: A) Sitting (90° flexed) femur bone mount with dimensions, B) Standing femur bone mount with dimensions.

The tibia bone mount was fixed to the 100 lb_f load cell using a 3/8" fine thread bolt, whereas the femur bone mounts were fixed to the lower crossbar of the Chatillon frame using two Allen bolts with large washers (Figure 30).

Figure 30: A) Tibia bone mount fixed to the load cell which is fixed to the frame, B) Femur bone mount fixed to the lower cross bar of the load frame.

Chapter 3

Precision & Accuracy Methodology

3.1 Background and Related Work

The ability of radiostereometric analysis to detect motions of less than 0.1 mm and rotations of less than 0.5° in all directions is what makes RSA so useful in the orthopaedic field. High accuracy measurement allows researchers to predict implant survivorship in terms of wear and fixation over a short-term period of 2 to 3 years [100-102]. Phantom model experiments have been performed by many researchers on many different RSA systems, and have become the accepted method for validating both the precision and accuracy of radiostereometric analysis [95, 96, 103, 104].

3.1.1 RSA Precision & Accuracy

The precision of any given system is the ability to obtain the same result when performing repeat measurements of a single entity under controlled conditions. Accordingly, the precision of an RSA system has been generalized as the difference in position and orien-

tation between multiple examinations of an implant when no relative displacement between the components and/or bone has occurred [84, 95]. Specifically, precision is recorded as the standard deviation of the mean absolute displacement that is measured between the multiple examinations [103, 105].

Accuracy is determined by inducing a known (i.e., accurate and precise) displacement, for example with a micromanipulator or micrometer, and examining the motion that is detected by the RSA system. Accuracy, in the field of RSA, has been defined in two ways; the mean ± standard deviation of the difference between measured and true displacement [79, 90, 93], and as one half of the average width of the 95% prediction interval surrounding the least-squares regression line of measured versus predicted motion [96, 103, 105].

3.1.2 Considerations for Model-based RSA

Model-based RSA relies on the ability to accurately define contours or outlines in the radiograph pair in order to determine the 3-dimensional pose of an object. Additional factors come into play in this situation, such as the robustness of the edge detection algorithm, the method of pose estimation [106], and the accuracy of the computer model being used to project a 'virtual' contour [79].

Model-based RSA utilizes one of three different contour matching algorithms in order to determine the *in vivo* pose of the implant. The first algorithm that was developed involves the minimization of non-overlapping area (NOA). The position and orientation of the virtual implant model is altered in an iterative process to find its optimal position by

minimizing the contour area that is not common to both implant silhouettes. The second algorithm is the iterative inverse perspective-matching (IIPM) algorithm in which a series of closest points between the virtual and actual contours are selected and an iterative closest point algorithm reduces the distance between the series of closest points. The third algorithm is the contour difference algorithm (known as DIF). This algorithm minimizes the mean distance between each point on the virtual and actual contours. The DIF and IIPM algorithms are the most robust methods for pose estimation [106]. This research utilized the IIPM algorithm as it is designed to equalize the contour error around the entire implant model, whereas the DIF algorithm tends to weigh the contour error to one side of the model as it simply minimizes the total contour error.

The agreement between a computer-aided design (CAD) model and the manufactured object has become an important topic in recent years due to the advent of model-based RSA. If a CAD model differs from the physical implant by much more than 0.1 mm, the accuracy of the RSA system may be reduced [79, 107]. As a result, this research utilized reverse-engineered (RE), 3-dimensionally scanned, computer models of the prosthesis being used in the RSA phantom.

Due to the complex geometry of a total knee replacement, such as the Genesis II prosthesis, finding the exact 3-dimensional pose of the implant is not an easy task. One area that is thought to cause such problems is defining the projected outline of the femoral condlyes. All published literature on model-based RSA of the knee has examined the joint from the front, that is, in the coronal plane [90, 92, 93, 104, 108], with the exception of Gill et al., 2006 [49] who used a unique triangular RSA calibration frame, and Trozzi et al., 2008 [104] who used a bi-planar (square) calibration frame. However, in the saggi-

tal plane, the knee prosthesis has sharp, orthogonal edges that are visible in a radiograph. Contour detection of these sharp edges may potentially improve the accuracy of mbRSA and thus improve polyethylene wear analysis of knee prostheses.

3.1.3 Measuring Polyethylene Wear

Research into *in vivo* wear of the polyethylene (PE) bearings in TKAs has become increasingly important as long-term survivorship of the prosthesis depends on low wear rates and few wear particles. Because of the toughness of newer generation PE bearings, short-term measurement of wear is on the sub-millimeter scale. The high sensitivity of RSA makes it a candidate for clinical analysis of short and long term PE wear.

Wear in a TKA can be approximately measured as the change in proximity between the femoral condyles and the top surface of the tibial tray. Therefore, it is crucial that RSA is able to detect relative micromotion between the femoral condyles and the tibial tray of less than 0.1 mm [109]. Other factors such as cold-flow (creep) of the polyethylene and deformation under load also affect the proximity of the components. However, the effect of PE cold-flow is not examined here as it is outside of the scope of this research.

For the remainder of this thesis we refer to the measured relative displacement between the TKA components (proximity), as model-to-model precision. Similarly, we refer to the measured displacement of the TKA components with respect to a series of tantalum markers embedded the surrounding bone as model-to-marker precision.

3.1.4 Objectives

The main objective of this research is to determine which of four RSA imaging orientations as well as three knee flexion (bending) angles obtain the greatest model-to-model precision using model-based RSA. The second objective of this research is to determine the *in vitro* best-case accuracy of those imaging orientations and flexion angles with the greatest model-to-model precision. The tertiary objective is to quantify the model-to-marker precision for use in longitudinal TKA migration studies. The precision/accuracy phantom described in Chapter 2 has been used to attain these objectives.

3.2 Equipment

The equipment available at the Concordia Hip and Knee Institute (CHKI) for model-based RSA is a combination of the mbRSA software, version 3.4, from Medis Specials (Leiden, The Netherlands) and the Carbon-Fibre uni-planar calibration box (Figure 7) from Halifax Biomedical Inc. (HBI) (Mabou, Nova Scotia, Canada). The phantom model described in Section 2.2 was placed on a wheeled support stand to aid in manoeuvrability of the phantom. Two ceiling mounted X-ray sources (Varian Medical Systems RAD-92) were aimed horizontally at the calibration box at 30° to the perpendicular of the box (Figure 31). The x-ray sources were located approximately 160 cm away from the digital radiography (DR) imaging plates (Canon CXDI-55C, Canon Inc., Lake Success, New York) that were slotted in behind the calibration box. The phantom model was placed approximately at the crossing point of the x-rays as shown in Figure 31.

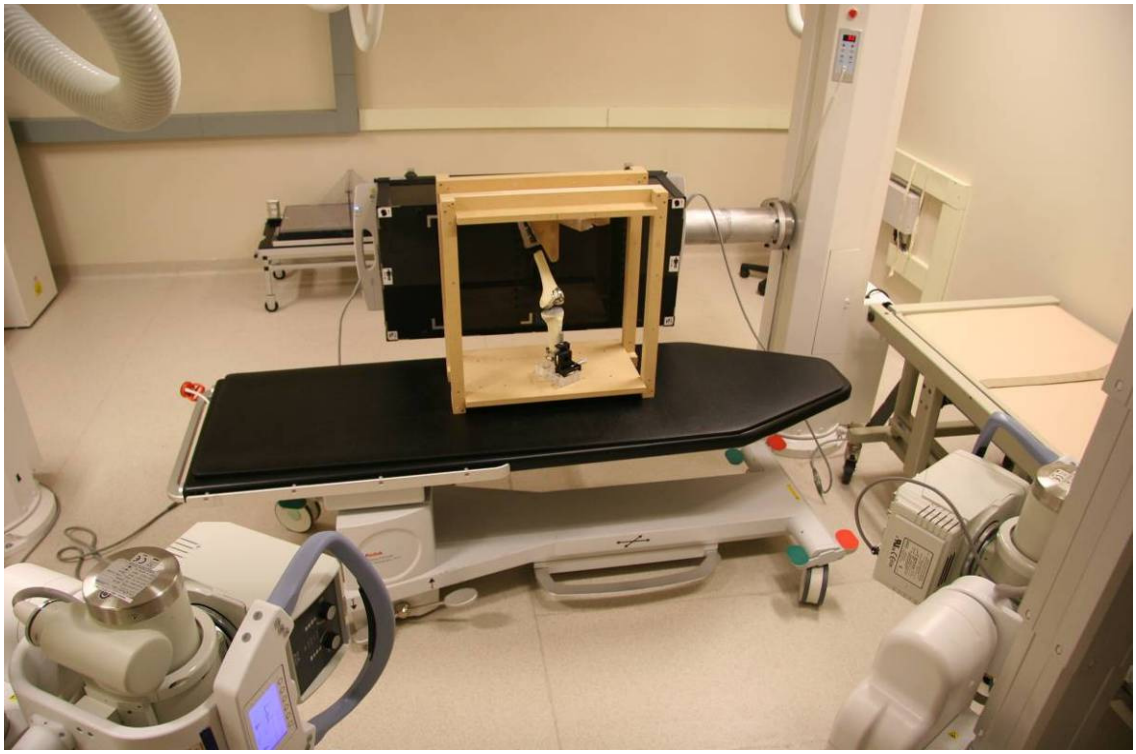

Figure 31: RSA setup with HBI calibration box, DR imaging plates, precision phantom model on wheeled support, and dual x-ray tubes positioned horizontally at 30° to the perpendicular of the calibration box.

3.3 Radiograph Processing

All radiographs were transferred from the x-ray workstations to the analysis workstation via internal computer network. Image pairs were labeled according to their individual circumstances (flexion, orientation of RSA exam), numbered from 0 (reference image pair) to n (precision stage n=9; accuracy stage n=6), and labelled as left or right (L or R) images. All x-ray images were imported into mbRSA along with the model files of each component and empty marker files for the tantalum markers in both the femur and the tibia (Figure 32A). RSA image pairs were initialized and calibrated automatically by

mbRSA based on the fiducial and control marker locations. Markers in the tibia and femur were then automatically detected and any markers that were not detected automatically were selected manually (Figure 32B).

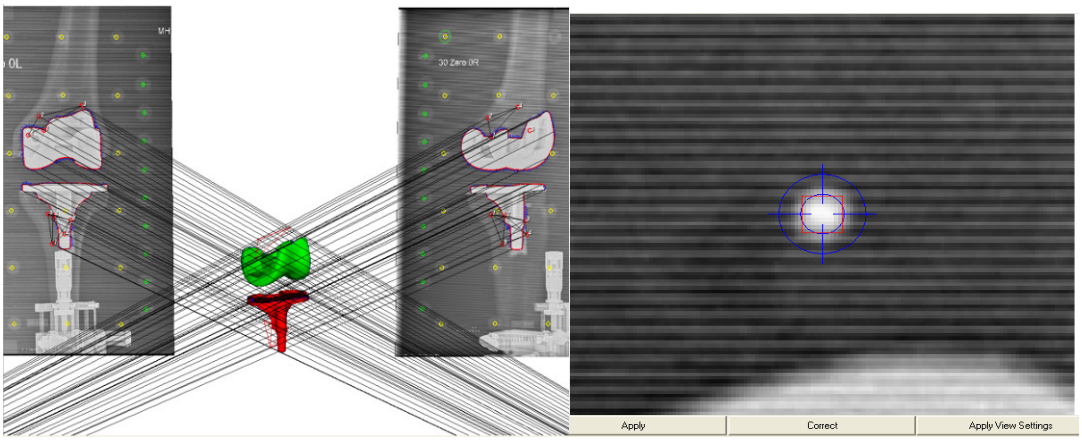

Figure 32: A) Model-based RSA workspace with image pair and TKA models. B) Manual marker selection tool.

The external contours of the TKA components were detected within a user-specified region of interest. A pixel smoothing value of 3 and edge detection threshold of 500 was used for contour detection of the femoral and tibial component contours. Only external contours were selected as the mbRSA pose algorithm cannot utilize internal contours and features of the implants. The contour of the underside of the tibial tray was not selected as it was difficult to distinguish between the tibial tray and the radio-opaque bone cement immediately underneath (Figure 33A). Any disruptions in the implant contours (presence of marker beads, micromanipulators) were de-selected from the contour of the component.

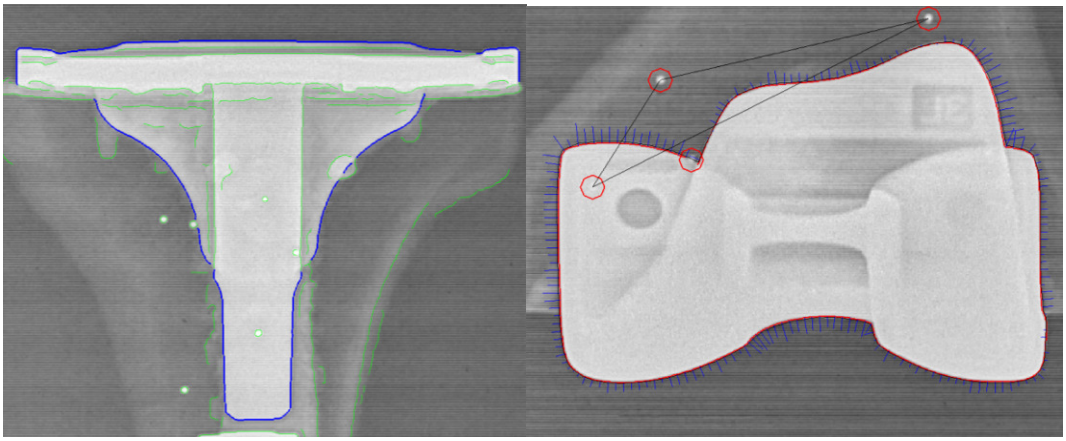

Figure 33: A) Contour selection of the tibial tray (blue contours). Underside of tray and interruption by marker beads not selected. B) Contour mismatch of the femoral condyles; blue lines indicate 10x the error (difference between contour and model).

Pose estimation of each TKA component was performed using the Iterative Inverse Perspective Matching (IIPM) algorithm utilizing 10% of the points on the contour (Figure 33B). Ten percent of the object contour was chosen to improve the quality of fit between the projected and image contours without compromising computation time [106]. The error of fitting (sum of difference between image contour and projected contour) was recorded for each component for each image pair.

3.4 Precision Experiment

This stage of experimentation examines the effects of altering imaging orientation and knee flexion on the precision, or repeatability, of mbRSA pose estimation. The error measured on 12 sets of 10 non-identical RSA radiographs is used to determine the overall precision of the mbRSA system. Multiple analysis metrics, image comparison techniques,

and statistical tests have been applied to the radiographs in order to examine differences in translation and rotational precision between the imaging settings.

3.4.1 Imaging Procedure

Four different imaging orientations were examined using the knee phantom: x-ray sources at 30^{o} to the antero-posterior (AP) axis of the knee joint (hereafter referred to as AP orientation), Figure 34A, x-ray sources at 30^{o} to the medio-lateral (ML) axis of the joint (hereafter referred to as ML orientation), Figure 34B, one x-ray source centered along the AP axis with the other at 30^{o} offset from the ML axis of the knee (hereafter referred to as 30° offset orientation), Figure 34C, and one x-ray source centered along the ML axis with the other at 60^{o} offset from the AP axis of the knee (hereafter referred to as 60° offset orientation), Figure 34D. Three different flexion angles were also examined using the precision phantom: standing (0° flexion), 45° flexion, and sitting (90° flexion) (Figure 34).

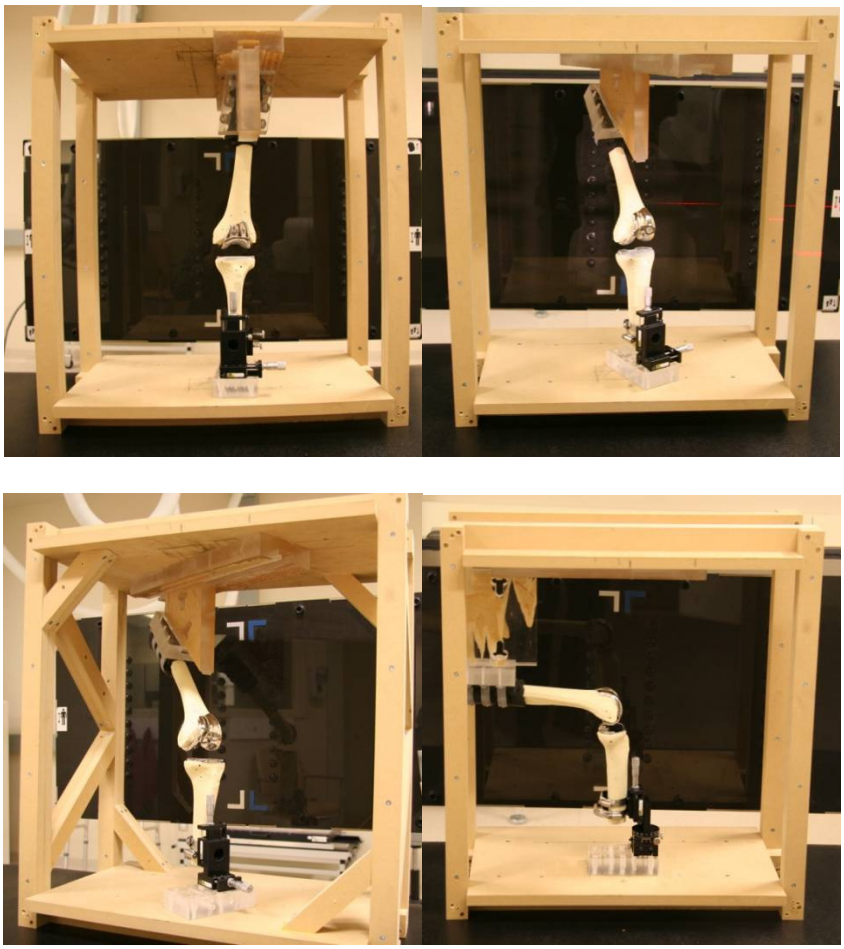

Figure 34: Knee phantom; A) standing, AP orientation; B) 45° flexion, 30° offset orientation; C) 45° flexion, 60° offset orientation; D) sitting, ML orientaion.

Each RSA image pair was obtained using 2 mAs and 125 kV settings on the x-ray sources. The tibia and femur Sawbones were rigidly fixed to the frame such that relative movement was minimized between the two TKR components. The frame was placed on a specialized radiography bed such that the phantom setup could be moved around the image area (to obtain non-identical images) using the lateral slide and vertical lift features of the bed. This allows our findings to be more transferrable to clinical precision, as patient RSA images are never obtained in exactly the same position.

3.4.2 Experimental Design

A full-factorial experimental design was selected with 2 factors with 3 and 4 levels of each factor (Orientation: AP, 30°-Offset, 60°-Offset, ML; Flexion: 0°, 45°, 90°). This design allowed for a complete analysis of the effect each of these parameters on the precision of mbRSA. The number of replicates required for statistical power in this 2-factor experiment was determined using the following equation [110].

$$n = \frac{2a\sigma^2\Phi^2}{bD^2}$$

Where α is the number of levels in factor A, b is the number of levels in factor B, σ is the approximate or anticipated standard deviation of the experiment metric and D is the difference we are trying to detect. The parameter Φ^2 is approximated from a psychrometric chart [110] which relates the degrees of freedom of the numerator and denominator to the probability of accepting the null hypothesis when it is in fact true (1-β, or power) based on the selected level of significance.

To determine the approximate standard deviation (σ) required for the sample equation a sample set of 10 RSA image pairs (9 RSA migration comparisons) were obtained of the Genesis II TKA components in the typical AP axis orientation with no flexion of the joint. The relative translation between the tibial tray and femoral condyles in the y direction (superior-inferior direction) was decided to be the primary measurement metric for this experiment, as measurement of polyethylene wear is most dependant on this axis of movement. The standard deviation of locating the components in the y-direction was found to be better than 0.05 mm.

Given that a=4, b=3, σ = 0.05 mm, a selected level of significance α = 0.05, with β = 0.80, and Φ = 1.85 ($numerator_{df}$ = 3, $denominator_{df}$ = 2 factors * 3 levels * n >5 = 30 or greater) a table of values was created to determine the minimum statistical difference that could be detected within a reasonable number of replicates. A detectable difference of 0.05 mm was chosen as the required number of replicates for the factorial experiment was reasonable at 7 (8 images, 7 image comparisons). To account for unforeseen changes in the standard deviation of y-direction movement, the number of replicates was increased to 9 (10 images, 9 comparisons).

3.4.3 Analysis Methods

Deviation in y-directional distance between the femoral and tibial components was used as the primary metric for determining which imaging orientations and knee flexion angles attained the greatest precision. However, three additional metrics were also examined; the absolute deviation in the y-direction, maximum total point motion (MTPM) for translation, and MTPM for rotation. Maximum total point motion is the vector sum of deviation in 3-dimensional position, summarized as $\sqrt{(dx^2 + dy^2 + dz^2)}$. Similarly, rotational MTPM is summarized as a "vector sum" of rotational deviation about all three axes, $\sqrt{(x_r^2 + y_r^2 + z_r^2)}$. These additional metrics allowed for all three degrees of translational freedom, and all three degrees of rotational freedom, to influence the analysis and comparison of each experimental factor.

Four different techniques were used to obtain the deviation(s) in position between the femur and the tibia for each of the 10 radiographs. Initially, the 0^{th} image in each set of 10 images was used as the reference RSA image pair, and the remaining 9 image pairs

were compared to this reference (hereafter referred to as the reference dataset). However, this technique was highly dependent on any errors present in the 0^{th} image. The second technique employed was to randomly select the reference image in each set of x-rays (hereafter referred to as the random-reference dataset). The third technique was to compare each image to each other image, or to obtain all pairs of comparisons, which results in a total of 45 data points (hereafter referred to as the all pairs dataset). However, the all pairs technique had to take into account that the number of individual observations (degrees of freedom) remained at 9. The fourth technique was to compare 5 pairs of RSA images, such that the comparisons were fully independent (not dependent on a single reference image). The 0^{th} and 1^{st} images were compared, as well as the 2^{nd} and 3^{rd} images, the 4^{th} and 5^{th} images, etc (hereafter referred to as the independent pairs dataset). Assessment of the 4 imaging orientations and 3 flexion angles was carried out with each of these four techniques and the results were compared to ensure that the four techniques were in general agreement.

An Anderson-Darling test (described in Appendix A) for normal distribution was applied to each subset of the data (separated by model type, image comparison method, and outcome metric), in order to validate the use of parametric statistics. To account for any non-normal distributions in the data, non-parametric statistical methods were performed in parallel with the parametric methods. The results of these methods were subsequently compared to ensure overall agreement in the final outcome.

Parametric analysis of the factorial experiment was performed using Minitab version 15 (State College, PA). Main and interaction effects plots were created for each factor and each outcome metric. Main effects plots show the effect of an experimental factor

(orientation/flexion) on the overall precision while removing the effect of the second factor. As well, Tukey's pair-wise comparisons were computed to determine statistical significance between individual levels of each factor. Analysis of variance (ANOVA) tables were calculated in Microsoft Excel to allow for adjustment of the degrees of freedom in the all-pairs dataset.

Non-parametric analysis was facilitated using a technique from McDonald, 2009 [111] in which the dataset is converted from measurement values (in mm) to number ranks. The minimum value in this dataset was ranked as 0, the next lowest as 1, etc., up to the maximum value as n. An analysis of variance was then performed in MS Excel on the ranked dataset.

Due to the large amount of data collected (2 types of mbRSA models, 4 outcome metrics, and 4 image comparison methods) a scoring summary was created to simplify the numerous results down to a concise outcome. Using the visual results from the main and interaction effects plots as well as the statistical results from the ANOVA tables and Tukey's tests, each level of knee flexion and imaging orientation was ranked. A weighted scoring scheme was applied to the 4 measurement metrics according to their perceived importance; Yt = 4 points, Abs Yt = 2 points, MTPM (t) = 3 points, and MTPM (r) = 1 point. Translational precision was deemed to be the most important, particularly in the Y direction as this is a direct measure of linear penetration and wear. Absolute deviation in Y translational precision (Abs Yt) and rotational precision (MTPM (r)) were given lower importance as these metrics are not directly related to wear measurement. The weighted scores of each measurement metric were used to grade the imaging settings individually. A negative score was applied to the image setting if it was statistically worse (lower pre-

cision) than the other settings, whereas a positive score was applied if the setting was statistically better (greater precision) than the other settings. For example, if the AP orientation setting showed statistically better Y_t precision than the other orientations, AP was given a score of +4. Conversely, if the AP setting showed statistically worse MTPM (t) precision, AP was given a score of -3. The scores for each imaging setting were summed to obtain a subtotal score. The subtotals for each of the four methods of image comparison were combined and to obtain a grand total score for each imaging factor. The imaging factors with negative scores were removed from further experiments.

Precision of the TKA component models to the surrounding marker bead cluster (embedded in the Sawbones) was calculated as the standard deviation of motion under zero-displacement conditions. The 0^{th} image of each set of x-rays was used as the reference image, and the subsequent 9 images were compared to the reference. Only those images with 4 or more visible markers were used in the analysis to reduce the effect of rigid-body error on the migration calculations. The results of this experiment are presented in Section 5.1.

3.5 Accuracy Experiment

This experimental stage built off of the overall outcome of the precision experiment. The imaging settings with the greatest precision were further tested to establish the approximate accuracy of each setting. Known increments of translational and rotational displacement were applied to the TKA components which were subsequently measured us-

ing mbRSA. The difference, or error, between the known and measured displacement was analyzed using two different methods to establish the limits of mbRSA accuracy.

3.5.1 Imaging Procedure

Based on the results of the precision stage, two orientations and two flexion angles with the greatest precision were selected for further analysis of translational and rotational accuracy. The same imaging procedure described above was used in this stage of testing. The phantom frame was placed on the radiography bed and moved around the imaging area to obtain non-identical RSA images. However, as this experiment involved highly precise movement of the TKA components, the phantom had to be aligned with the RSA coordinate system. A bubble-level was used to level the phantom frame in both the X (medio-lateral) and Z (antero-posterior) axes of motion (Figure 35A). The phantom frame was aligned to the calibration box using a triangle-square to ensure that movements of the micromanipulators were along or about the axes of the RSA coordinate system (Figure 35B).

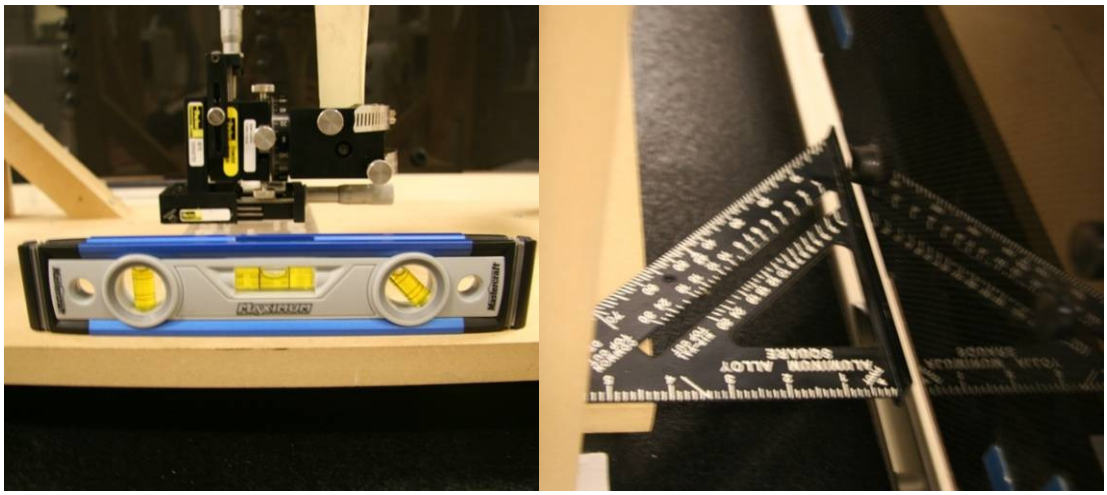

Figure 35: A) Leveling the phantom frame. B) Aligning the phantom frame with the calibration box.

3.5.2 Experimental Design

The purpose of this experimental stage was to obtain numerical values for the accuracy of the mbRSA system for each imaging orientation and flexion angle that were determined to be optimal from the precision testing stage. Accuracy was defined as the mean, plus or minus the standard deviation of the difference between measured and actual displacement [79, 90, 93]. A secondary definition of accuracy was also examined; half of the average width of the 95% prediction interval about the predicted versus measured regression line [96, 105]. Accuracy was determined for each axis of motion for both translational and rotational movement.

Following previous accuracy studies [96, 105] a series of incremental linear motions and rotations were selected for accuracy analysis of the mbRSA system. The reported accuracy of the translation slides (Parker Hannifin Corp., Cleveland, OH) was 0.002 mm, which was increased to 0.005 mm as the trays were non-new and were loaded with Sawbones, TKA components, and other fittings when used. The rotation table had a Vernier scale with 12 arc-minute increments (1/5 of a degree) which was chosen as the accuracy tolerance of this device. Taking these accuracy limits into consideration, the translational increments were selected as 0.02, 0.05, 0.10, 0.20, 0.50, and 1.00 mm, whereas rotational increments were selected as 0.2, 0.4, 0.6, 2.0, 4.0 and 6.0°. These increments were selected to weight effects toward small micromotions that are more difficult to detect. Using this scheme of increments, 6 comparisons were made between a reference image and 6 subsequent images. Thus, a total of 168 RSA images (7 increments * 6 degrees of

movement * 4 imaging/flexion settings) were collected, providing 144 image comparisons for the accuracy stage.

3.5.3 Analysis

Unlike the precision testing stage, image comparisons were only made between the reference image (0^{th} image) and each of the following images, as displacement in each subsequent image could only be compared to the reference image. As well, only the measured motion along or about the particular axis of interest was used in the analysis of accuracy. No vector summations were examined as any movement that occurred along or about the remaining axes was assumed to be looseness or non-linearity in the micromanipulators, and not a result of misalignment of the phantom frame.

The mean and standard deviation of error (measured displacement – actual displacement) was used as the primary assessment of mbRSA accuracy for all imaging settings. As well, linear regression was performed between the measured and actual displacements and the 95% prediction intervals (PI) were computed for each displacement increment (each 'x' value) using SAS Enterprise Guide Version 4.2 (SAS Institute, Cary, NC). The width of these 6 intervals was averaged and halved to obtain the required mean ½ width of the 95% prediction interval. An analysis of variance was then performed on both the error and the ½ PI widths using Minitab Version 15, to determine if either of the 2 imaging orientations and 2 knee flexion angles showed significantly greater accuracy.

Model-to-marker precision between the TKA components and the surrounding tantalum markers was calculated as the standard deviation of motion under zero-displacement conditions. The 0^{th} image of each set of x-rays was used as the reference image, and the

subsequent 6 images were compared to the reference. The precision data was separated according to the 4 imaging settings, providing 36 data points for each setting. The results of this experiment are presented in Section 5.2.

Chapter 4

Physiological Phantom Methodology

4.1 Background and Related Work

Accurate measurement of polyethylene wear in a total knee replacement is more complex than measurement of wear in total hip replacements due to the greater kinematic complexity of the knee joint. Hip joints undergo simple ball-in-socket articulations [112] in which wear is typically measured as the penetration of the femoral head into the polyethylene liner of the acetabular cup [48, 113, 114]. The knee joint undergoes both rolling and sliding motions of the femoral condyles against the tibial bearing surface, and can experience a wide range of motion; flexion, internal/external rotation, and varus/valgus rotation. The area of contact, and therefore the area of wear, between the tibial insert and the femoral condyles will differ depending on the activity being performed, the implant type/design, and positioning of the components in each patient [115, 116].

Assessment of short term wear is important to determine the long-term mechanical survivorship of a TKA by estimation of an annual wear rate. National joint registry data

from Australia, New Zealand, and Scandinavian Countries, has shown that approximately 30% of all TKA revisions are due to aseptic loosening [117-119], which is most commonly caused by implant wear-induced osteolysis [120]. The introduction of cross-linked polyethylene (XLPE) in total hip replacements (THAs) has shown a substantial increase in both the mechanical life of this joint replacement and long-term survivorship through reduction of osteolysis [48, 113]. It is likely that the benefits of using XLPE in THAs will be seen in TKAs, particularly given the evidence of extremely low XLPE wear rate from knee simulator studies [41, 44, 121]. However, orthopaedic surgeons are somewhat reluctant to implant cross-linked polyethylene in TKAs due to a concerns including; the production of smaller, possibly more bioactive wear particles, fracture of the liner and/or posterior stabilized post, and fracture of the liner locking mechanism [122-124]. Therefore, strong clinical evidence of the benefits of XLPE in TKAs (reduced wear) must outweigh the potential risks before a widespread switch is made from conventional UHMWPE to XLPE.

The risk of over exposure to ionizing radiation from RSA imaging is greatly reduced when imaging the knee compared to other joints near the torso, such as the hip, shoulder, and spine. The lack of vital organs and soft tissue surrounding the knee joint results in a far lower effective dose, on the order of 100x less than an antero-posterior hip x-ray [125]. Subsequently, multiple RSA examinations of the knee can be performed at each follow-up period without risking over exposure. This allows for the combination of data from multiple radiographs to obtain a more complete measurement of polyethylene wear [49].

A study by Gill et al, 2006 [49] is the only published study to examined *in vivo* wear of the polyethylene insert in 15 TKA patients using a model-based RSA analysis software that was developed and validated in-house [126]. Radiographs of the each patients' TKA were obtained at four different flexion angles; 0°, 30°, 45°, and 60°. Gill was able to estimate polyethylene wear by combining the penetration of the condyle surfaces observed in each of the 4 RSA radiographs of each patient. From this study, it is evident that *in vivo* measurement of polyethylene wear in a TKA is dependent on the flexion of the patients' knee. A second study by the same research group used a similar technique to examine polyethylene wear in a unilateral knee replacement [127]. The reported accuracy of measurement was better than 0.2 mm [49], whereas the precision of measurement of bearing thickness (2 * the standard deviation of the error) was 0.131 mm [127].

An unpublished pilot study from a research group in Halifax, NS [128], examined polyethylene wear in a medial-pivot TKA (Advance Medial-Pivot Implant, Wright Medical) phantom, in which the medial condyle and the corresponding polyethylene surface are fully congruent. This congruency results in pivoting of the tibial during internal/external about the medial condyle, while the lateral condyle moves fore and back across the non-congruent lateral side of the polyethylene insert. The technique employed by the researchers was to obtain five x-rays of the TKA phantom in the sitting (90° flexion) position; a reference image with no tibial rotation, two x-rays with internal rotation of the tibia, and two with external rotation. Analysis of the RSA x-rays at these positions allowed the researchers to obtain five measurements of wear depth in the lateral condyle in five different positions which could then be interpolated to estimate the average wear volume of the lateral condyle. Applying this technique to a non-congruent tibial insert,

such as the Genesis II TKA, it may be possible to obtain wear depths across both the lateral and medial condyles in two or more locations (depending on the number of x-rays taken). These multiple measurements can then be combined, and through interpolation of the wear depths, the total polyethylene wear volume can be approximated.

To the author's knowledge, no published studies of *in vitro* TKA phantoms have used previously worn polyethylene inserts in the experimental assessment of polyethylene wear. As well, no published studies have applied compressive force to the artificial knee joint while obtaining RSA radiographs. Compression the femoral condyles against the tibial insert in a physiological manner creates deformation of the polyethylene which mimics a true, *in vivo* knee RSA examination. Although both cold-flow of the polyethylene (creep) and deformation under load are not wear (removal of material), they are both effects which reduce the thickness of the poly underneath the condyles. However, precise measurement of polyethylene cold-flow over time and deformation under load is outside of the scope of this project.

The purpose of this experiment is to determine an accurate, simple, and repeatable process for measuring polyethylene wear in a TKA. It is hypothesized that RSA examinations under load-bearing conditions, flexion and internal/external rotation of the knee joint, and combination of RSA-measured wear pools will improve the ability of model-based RSA to estimate TKA wear.

4.2 Methods and Materials

4.2.1 Equipment

The same x-ray equipment and setup described in Chapter 3 was used in this experiment, with the exception of the Chatillon load frame and composite Sawbones, described in Section 2.2. The load frame was placed on the floor of the x-ray suite and aligned to the RSA calibration frame. The load frame was positioned 16” from the calibration frame such that the TKA components were at the approximate center of the crossing-x-rays (Figure 36).

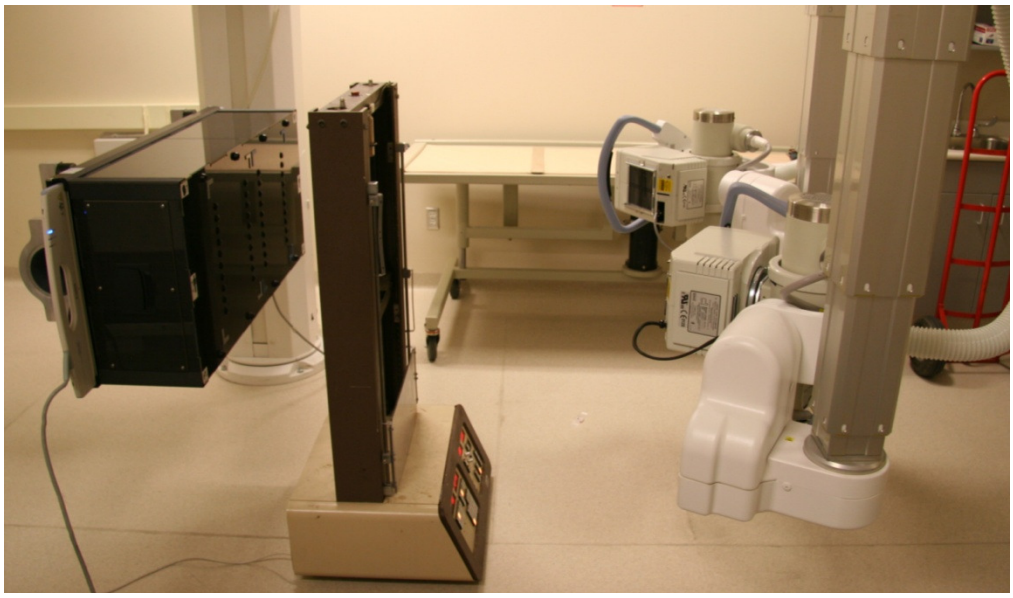

Figure 36: Physiological knee phantom and RSA setup.

For this study, a single new polyethylene insert was obtained to serve as an unworn reference against which retrieved polyethylene inserts were compared to. For accurate comparison, similar tibial inserts were obtained from the implant retrieval database at the

Concordia Hip and Knee Institute. Five, Genesis II, size 3, posterior stabilized, 13 mm thickness, retrieved polyethylene inserts with visible wear were obtained. Each insert was subsequently mounted into the peripheral locking mechanism of the tibial tray, and five RSA radiographs of each insert were obtained under the imaging conditions described below.

4.2.2 Imaging Procedure

Based on the results of the precision experiment (Section 5.1), the AP, ML, sitting, and standing imaging settings were applied to the physiological experiment. Accordingly, the physiological phantom was designed to replicate 5 possible knee/leg positions; AP orientation with standing flexion (Figure 37A), ML orientation with standing flexion (Figure 37B), and ML orientation with sitting flexion (Figure 37C) both with and without approximately 10° of internal and external rotation. Each polyethylene insert was installed by an interference fit into the peripheral locking system of the tibial tray, and removed by prying the anterior notch of the insert with a flat-blade screw driver (Figure 38).

The tibia bone mount was threaded into the 100 lb_f load cell mounted to the top of the load frame. The standing femur bone mount was placed on the lower, moving cross-bar of the load frame and fastened using two Allen bolts with large washers (in the AP orientation) and with two large quick-clamps (in the ML orientation) as shown in Figure 39. The sitting femur bone mount was placed on the lower cross-bar of the load frame and fasted using the same Allen bolts and washers as the standing mount in the AP position.

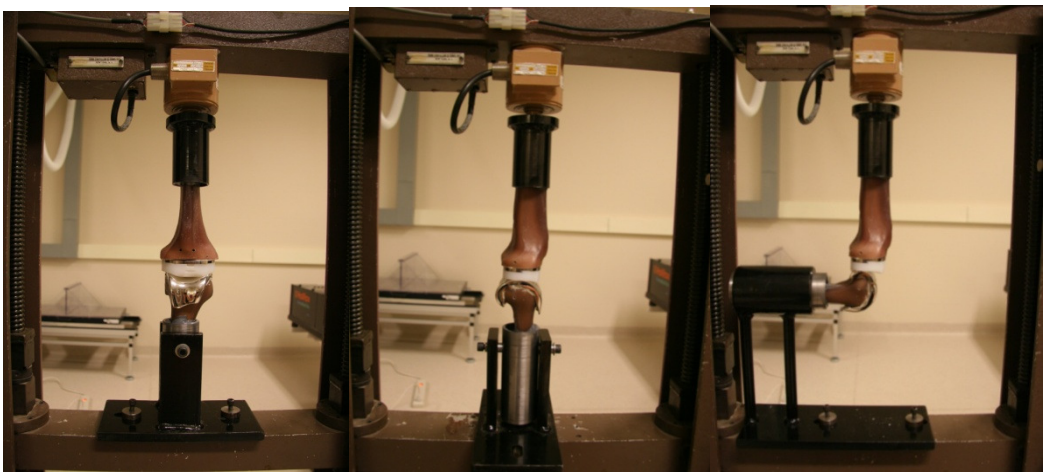

Figure 37: A) AP standing position, B) ML standing position, C) ML sitting position.

Figure 38: Removal of the polyethylene insert with a large flat-blade screw driver.

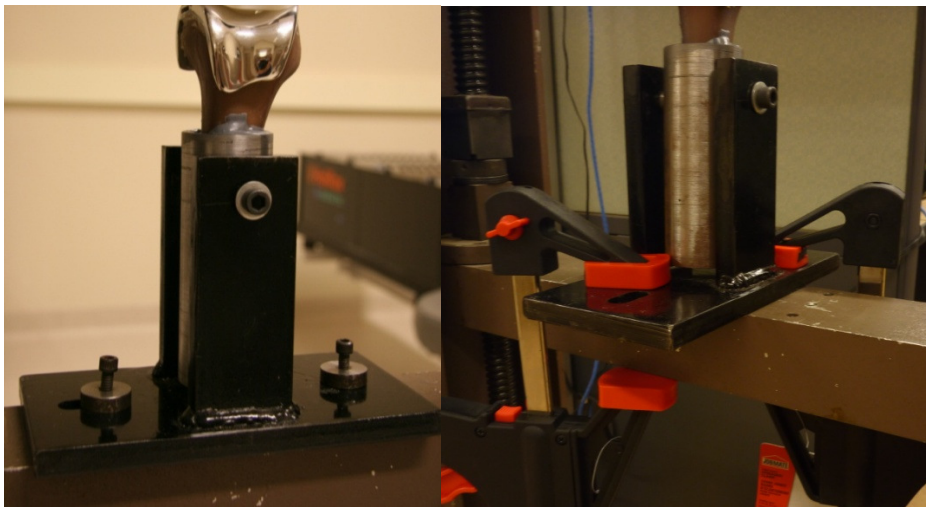

Figure 39: A) Allen bolts and large washers for fixation to the Chattilon cross-member. B) Quick clamps for fixation when in the ML standing position.

Load was applied through the artificial knee joint by moving the lower cross-bar of the load frame upward, to apply compression. When the tibial and femoral components were in contact with each other, the compressive force was applied as slowly as possible by reducing the movement increments of the lower cross-bar to 0.2" per minute. For the AP and ML standing cases, compression was stopped when the load cell reached 125 lb_f. Due to relaxation of the plastic joint components (polyethylene insert, composite Sawbones, epoxy resin), the 125 lb_f could not be maintained. After approximately 30 seconds, plastic relaxation had slowed sufficiently and additional compressive force was applied to again reach 125 lb_f. This process was repeated for each RSA x-ray that was obtained. Re-application of compressive force occurred whenever the load cell dropped below 115 lb_f. Similarly for the ML sitting cases, compression was stopped when the load cell reached 40 lb_f and was re-applied when the load cell dropped below 35 lb_f.

To determine the repeatability of wear measurement, three sets of 10 x-ray pairs were obtained of the phantom in the AP standing position (with 120 lb_f load), the ML standing position (with 120 lb_f load), and the ML 90° flexed position (under 35 lb_f load). An additional set of 10 x-ray pairs was obtained of the phantom in the AP standing position with less than 5 lbs of load, enough to ensure contact but without causing polyethylene deformation. The set of x-rays at 120 lb_f load was compared to the set of x-rays at <5 lb_f load in order to determine the approximate effect of polyethylene deformation on RSA wear measurement. The Chattilon load frame was moved around the imaging area for each x-ray pair in the repeated measurement sets such that non-identical images were obtained. RSA image analysis was performed in the same manner described in Section 3.3.

4.2.3 Pose Reconstruction/Computation

As described in Section 2.3.3, 1 new and 5 previously worn polyethylene inserts were scanned using the ShapeGrabber 3-D laser scanner. The scans were reconstructed in Geomagic studio and 100,000 element RE models of each of the 6 inserts were obtained. Each of the previously worn polyethylene inserts was compared to the unworn insert to determine the approximate depth and volume of the worn areas (hereafter referred to as wear pools) which were outlined in ink.

Each polyethylene insert model was seated within the peripheral locking system of the tibial tray model in Geomagic Studio. To ensure exact positioning of the insert model within the tray, a scan of the assembled tray and insert was obtained and the tray and insert models were aligned to the scanned assembly using the 9-point manual registration tool in Geomagic Studio (Figure 40).

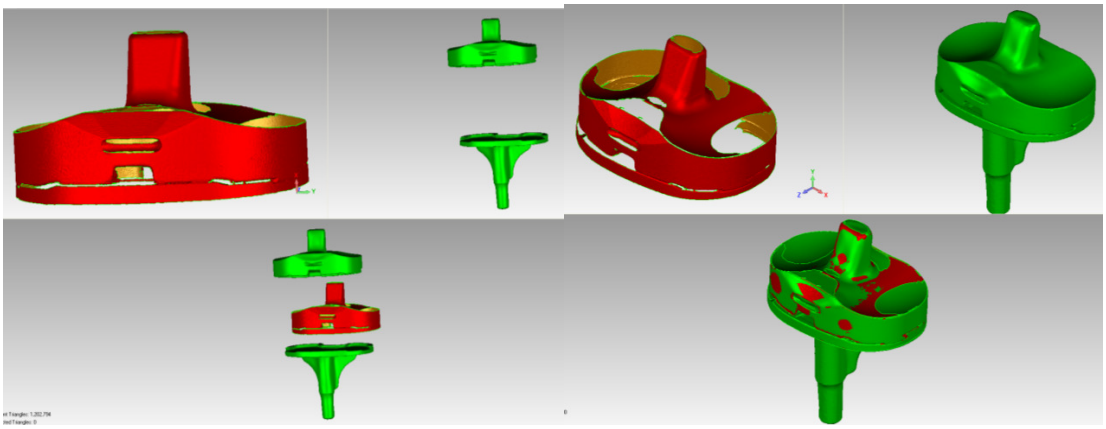

Figure 40: Alignment of polyethylene insert in tibial tray RE models (green) using a 3-D scan of the assembled insert and tray (red), A) beginning of alignment process, B) finished alignment.

Using pose data obtained from mbRSA, the 100,000 element TKA components models were re-positioned in Geomagic Studio in the same pose calculated by mbRSA. First,

the TKA component models had to be mirrored across the Y-Z plane at their center of mass, because they had been stored as right-sided implants by Medis Specials during conversion in mbRSA-specific files. The components were then translated to the origin (0,0,0) of the 3-D space within Geomagic Studio such that rotations could occur about the helical axis of each model. Rotations were entered in a specific order based on the order of geometric manipulation in mbRSA; rotation about the Y axis was performed first, followed by rotation about the X axis, and finally rotation about the Z axis. The components were then translated along each axis by the displacement specified by mbRSA using the transformation matrix operator in Geomagic Studio. The tibial insert was given the same rotations and translations as the tibial tray, which ensured that the fit between these components (as described above) was maintained after rotation and translation.

4.2.4 Wear Measurement

The areas of visible wear (defined as burnishing, scratching, and pitting of the polyethylene surface) on each of the previously worn polyethylene inserts were outlined in pen in order to distinguish the areas of "known" wear (Figure 41A). The inserts were scanned in the manner described in Section 2.3 and reconstructed in Geomagic Studio. The base and sides of the pre-worn and unworn inserts were aligned in Geomagic Studio, and the Boolean subtraction function was used to compute the volumetric difference between the pre-worn and unworn inserts. This volumetric difference was manually cleaned (deletion of extraneous areas) to obtain only the outlined areas of "known" wear (Figure 41B). The volume and surface area of these outlined areas was computed and defined as the "known" wear volume/area for each of the 5 pre-worn inserts.

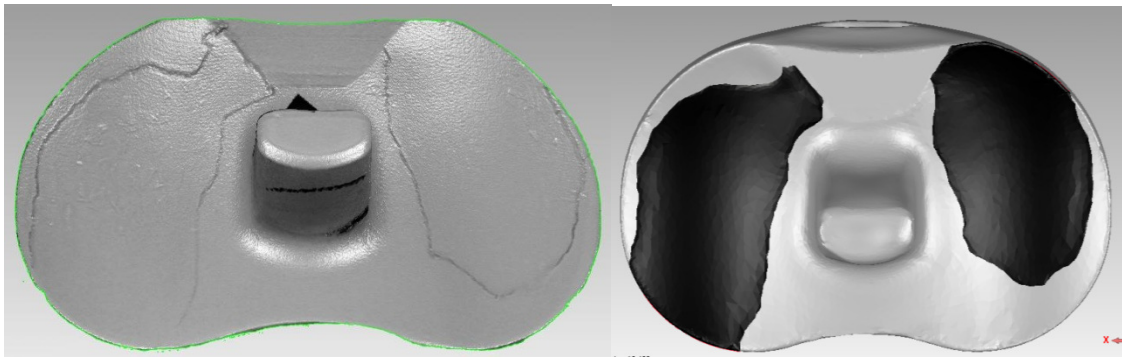

Figure 41: A) Surface of a worn polyethylene insert with visible wear areas outlined in marker, B) finished model of "known" wear areas of the polyethylene insert, shown in black.

Computation of polyethylene wear using the mbRSA pose data was performed by first positioning the TKA components in Geomagic Studio according to the pose data from mbRSA, as described in Section 4.2.3. A Boolean Intersection function was then applied to compute the overlap between the model of the femoral condyles and the model of the unworn polyethylene insert (Figure 42A). The volume and surface area of the overlapping areas (wear pools) was then computed and recorded. As well, the overlapping area was subtracted from the unworn polyethylene model which resulted in an "RSA-worn" insert for each RSA reconstruction (Figure 42B).

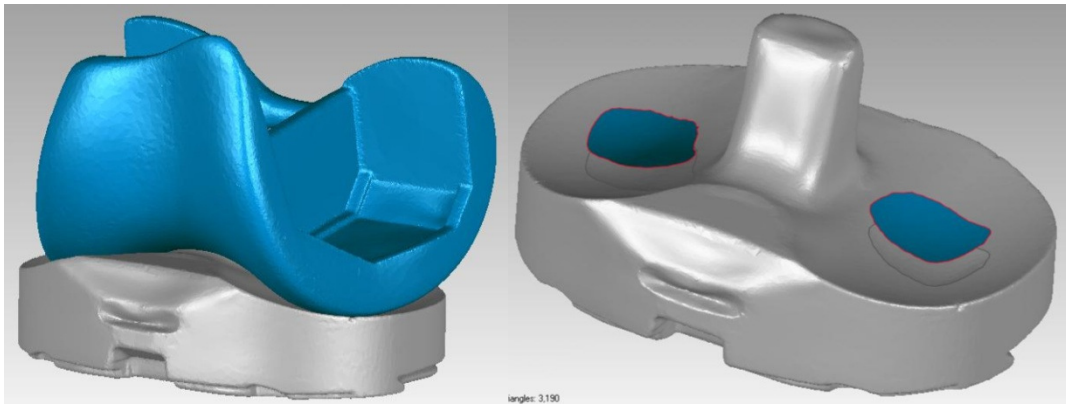

Figure 42: A) Reconstruction of overlapping femoral condyles and unworn tibial tray models using RSA pose data, B) Intersecting area between the two models (shown in blue) and RSA-worn polyethylene insert showing the wear pools outlined on the articulating surfaces.

Wear measurement was performed on each of the 5 phantom positions individually as well as 7 unique combinations of the RSA image pairs, for a total of 35 wear measurements. The combinations were designated as shown in Table 1.

Table 1: List of combined RSA images for wear calculation.

Combination	Images Combined
1	AP & ML standing
2	AP standing & ML sitting
3	ML standing & sitting
4	ML sitting, internal/external rotation
5	AP standing, ML sitting, internal/external rotation
6	ML standing, ML sitting, internal/external rotation
7	AP standing, ML standing, ML sitting, internal/external rotation (all 5 images)

The 5 individual RSA-measured wear pools for each pre-worn insert were combined according to the 7 image combinations described above. Combinations were performed by first grouping each RSA wear pool with the respective RSA-worn polyethylene insert (Figure 43A). The groups were then aligned to each other using the 9-point registration system in Geomagic Studio. Once fully aligned, the RSA-worn polyethylene inserts were removed from the workspace, leaving behind the wear pools in proper alignment. The wear pools were then amalgamated, according to the 7 unique image combinations, into cumulative wear volumes using the Boolean Union function in Geomagic Studio (Figure 43B). The volume and surface area of the combined wear pools were computed and compared to the “known” wear volume determined above.

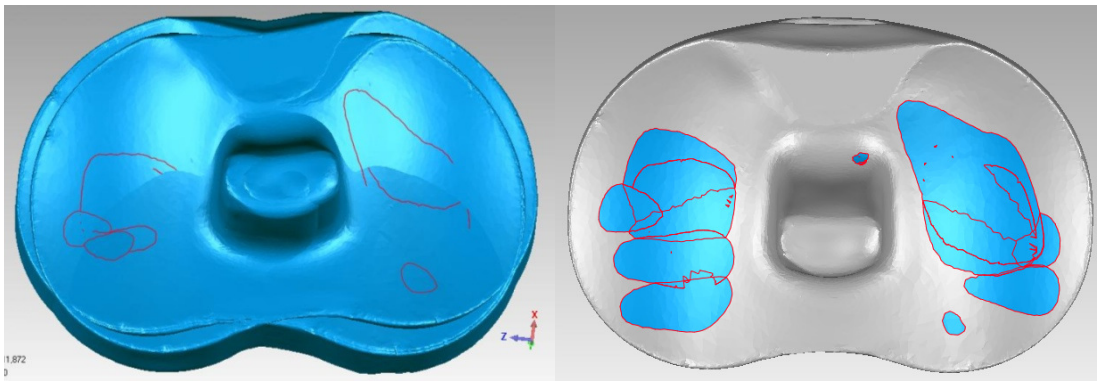

Figure 43: A) Pre-alignment of RSA-worn polyethylene inserts and wear pools, B) aligned inserts and combined wear pools (shown in blue).

The precision of wear measurement was defined as the standard deviation of the volumetric wear measured on each set of 10 repeated RSA images of the phantom with the unworn polyethylene insert. The effect of deformation of the polyethylene on the measurement of wear was determined through comparison of the loaded and unloaded sets of 10 RSA images in the AP Standing position. The wear measurement process described above was performed on these RSA images. The results of this experiment are presented in Section 5.3.

Chapter 5

Results

5.1 Precision Phantom

Precision of the mbRSA system was quantified, as shown in Table 2, as the standard deviation of zero displacement motion (error) [96]. Maximum total point motion for translation and rotation shown in Table 2 are the average MTPM values for each subset of data. Additional precision data for the all-pairs, random-reference, and independent pairs comparison datasets for original and revised models have been included in Appendix B. The reference comparison dataset is presented in the body of this thesis as it is the most common method of image comparison used by other researchers ([93, 96, 129, 130]).

In-plane model-to-model translational precision (Xt and Yt motion) was better than 0.050 mm in all cases of flexion and orientation, whereas out-of-plane translational precision (Zt motion) was better than 0.125 mm in all cases. Rotation about the Y axis was the least precise with up to 0.293° of error. Rotation about the X and Z axes were markedly

better at less than 0.119° (Xr motion) and 0.093° (Zr motion) of error. Overall, translational precision was better than 0.1 mm (MTPM translation), and rotational precision was better than 0.25° (MTPM rotation).

Table 2: Precision of mbRSA (standard deviation) calculated for all axes of motion (t = translation, r = rotation) and maximum total point motion for the reference image dataset (n=9), original models. The top 50% of cells in each column with the greatest precision (lowest error) are shown in bold.

Knee Flexion	Imaging Orientation	Xt (mm)	Yt (mm)	Zt (mm)	Xr (°)	Yr (°)	Zr (°)	MTPM t (mm)	MTPM r (°)
Standing	AP	**0.019**	**0.015**	0.036	**0.043**	**0.131**	0.044	**0.022**	**0.046**
	30° offset	0.034	**0.015**	0.084	0.093	0.293	0.071	0.048	0.203
	60° offset	0.026	**0.015**	0.118	0.083	0.147	**0.012**	0.116	**0.074**
	ML	**0.009**	**0.011**	**0.030**	**0.052**	**0.132**	0.054	**0.017**	0.079
45°	AP	**0.013**	0.018	**0.034**	**0.028**	**0.132**	**0.031**	**0.012**	**0.069**
	30° offset	0.047	0.030	0.080	0.066	0.183	0.046	0.058	0.123
	60° offset	0.045	0.028	0.123	0.075	**0.118**	0.068	0.068	0.078
	ML	0.034	**0.014**	**0.029**	**0.042**	**0.087**	**0.035**	**0.024**	**0.036**
Sitting	AP	**0.014**	**0.009**	**0.010**	0.062	**0.115**	**0.030**	**0.007**	**0.052**
	30° offset	0.033	0.027	0.073	0.072	0.161	0.037	0.046	0.165
	60° offset	**0.025**	**0.013**	**0.027**	**0.022**	0.182	**0.028**	0.027	0.130
	ML	**0.018**	**0.009**	**0.025**	**0.024**	**0.118**	**0.026**	**0.010**	**0.047**

The Anderson-Darling normality test (described in Appendix A) showed the majority of subsets of the data to be normally distributed (complete analysis data presented in Appendix C); reference dataset 70% normal, random-reference dataset 79% normal, all-pairs dataset 53% normal, independent pairs dataset 87% normal.

Parametric and non-parametric analysis of variance tables were calculated manually in MS Excel in to allow for manual adjustment of the degrees of freedom in each analysis. The two experimental factors, imaging orientation and knee flexion were included as factors in the model as well as an interaction effect. Table 3 is an example of the manually computed ANOVA tables. Further explanation of the ANOVA table is presented in Appendix A. Comparison of the statistical outcomes from both parametric and non-parametric analyses of variance showed 89.5% and 79.2% agreement, original and re-

vised models respectively (complete comparison data presented in Appendix C). As a result of these findings, parametric statistics were used for analysis of the data.

Table 3: Example of ANOVA table for Y translation. Reference comparison dataset, original models.

Yt Metric	Sum of Squares	Degrees of Freedom	Mean Square	Computed F ratio	Critical F value	P value
Orientation	9027.1	3	3009.0	6.16	2.7	Sig
Flexion	41370.8	2	20685.4	42.32	3.1	Sig
Interaction	78067.0	6	1301.2	2.66	2.2	Sig
Error	46925.6	96	488.8			
Total	105130.4	107				

The effect of imaging orientation, knee flexion, and the interaction between these two experimental factors on overall mbRSA precision (standard deviation) was examined using main and interaction effects plots. The factorial experiment analysis tool in Minitab was used to create individual effects plots for the 4 outcome metrics, the 4 image comparison methods and both the original and revised TKA models. A total of 32 main and 32 interaction effects plots (4 measurement metrics * 4 image comparisons methods * original & revised models) were generated for analysis. An example of these plots is shown in Figure 44.

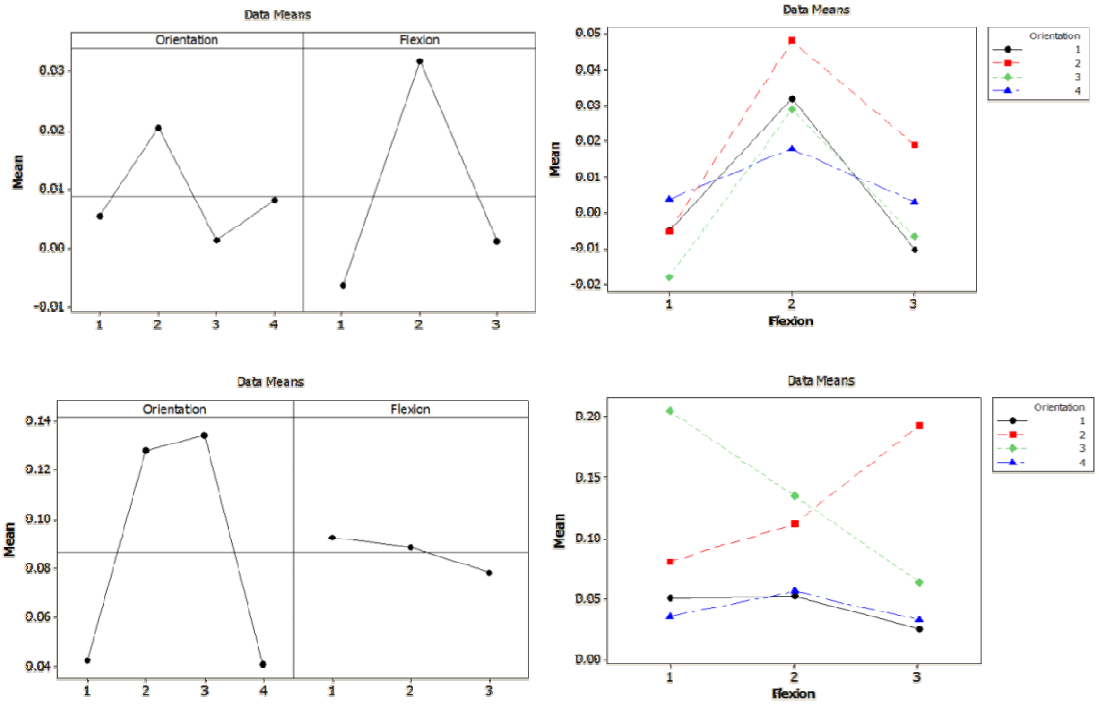

Figure 44: Plots of the effect of orientation and flexion on mean error (precision); A) Main effects and B) interaction effects for Y translation. C) Main effects and D) interaction effects for MTPM translation. Reference comparison data, original models. Orientation 1-AP, 2-30° Offset, 3-60° Offset, 4-ML. Flexion 1-Standing, 2-45° Flexed, 3-Sitting.

Using the weighting and scoring schemes described in Section 3.4, scoring tables were compiled to determine the overall effect of knee flexion and image orientation on mbRSA precision. A net positive score indicated a beneficial imaging setting whereas a net negative score indicated a detrimental setting. The summary scoring table (summation of scores for all image comparison methods) is shown in Table 4. The 4 individual scoring tables are presented in Appendix D. As shown in Table 4, the AP and ML imaging orientations were shown to be the most precise, as well as the standing (0° flexion) and sitting (90° flexion) knee flexion angles (shown in bold).

Table 4: Summary of scoring tables for imaging orientation and knee flexion settings. A positive score indicates improvement in precision, whereas a negative score indicates a reduction in precision.

Setting	Reference		Random Reference		All Pairs		Independent Pairs		Average Score
	Original models	Revised models	Original models	Revised models	Original models	Revised models	Original models	Revised models	
AP	0	-3	-4	2	0	3	4	2	**1**
30° OS	-10	-3	0	-3	-10	-1	-7	-7	-10.25
60° OS	-4	-9	-8	-9	-5	-9	-1	-5	-12.5
ML	3	7	3	7	3	7	4	6	**10**
Standing	4	3	-1	5	3	5	-1	0	**4.5**
Flexed	-6	-4	-5	-3	-6	0	-6	-5	-8.75
Sitting	0	0	2	-5	3	0	2	3	**1.25**

Five tantalum markers were inserted into both the tibia and the femur surrounding the TKA components to be used as a 'gold standard' reference to measure precision and accuracy. However, due to marker occlusion in the femoral condyles in some imaging orientations, all 5 markers could not be selected as part of the rigid body model. This resulted in reduced accuracy of the rigid body localization and greater error in the markers than in the mbRSA models. For this reason, the marker data was restricted to model-to-marker precision and was not used for marker-to-marker (tibia-to-femur) zero displacement analysis, as the 'gold standard' had greater error than the model-based system. A summary of precision results of model-to-marker measurement is shown in Table 5 with detailed results in Appendix E.

Table 5: Average precision (standard deviation) of zero displacement between TKA models and >3 bone markers.

	TKA Models	Xt (mm)	Yt (mm)	Zt (mm)	Xr (°)	Yr (°)	Zr (°)
Tibia	Original Models	0.016	0.013	0.030	0.061	0.142	0.046
	Revised Models	0.018	0.020	0.038	0.094	0.173	0.049
Femur	Original Models	0.028	0.035	0.032	0.097	0.086	0.065
	Revised Models	0.026	0.034	0.031	0.091	0.087	0.067

5.2 Accuracy Phantom

Based on the results from the precision experiment, AP and ML orientations and standing and sitting flexion angles were used for the accuracy experiment. The mean and standard deviation of error (measured versus actual displacement) was calculated for each displacement along or about each axis, for the 4 imaging settings. Similar to the precision experiment, only displacement between the TKA models in mbRSA was analysed. In-plane (X and Y) translational accuracy (standard deviation of error) was better than 0.035 mm (original models) and 0.051 mm (revised models). Out-of-plane (Z) translational accuracy was better than 0.068 mm (original models) and 0.111 mm (revised models), as shown in Figure 45A. In-plane rotational accuracy (Z) was better than 0.12° (original models) and 0.14° (revised models). Out-of-plane rotational accuracy (X & Y) was better than 0.17° (original models) and 0.25° (revised models), as shown in Figure 45B. Tabulated accuracy data is presented in Appendix F.

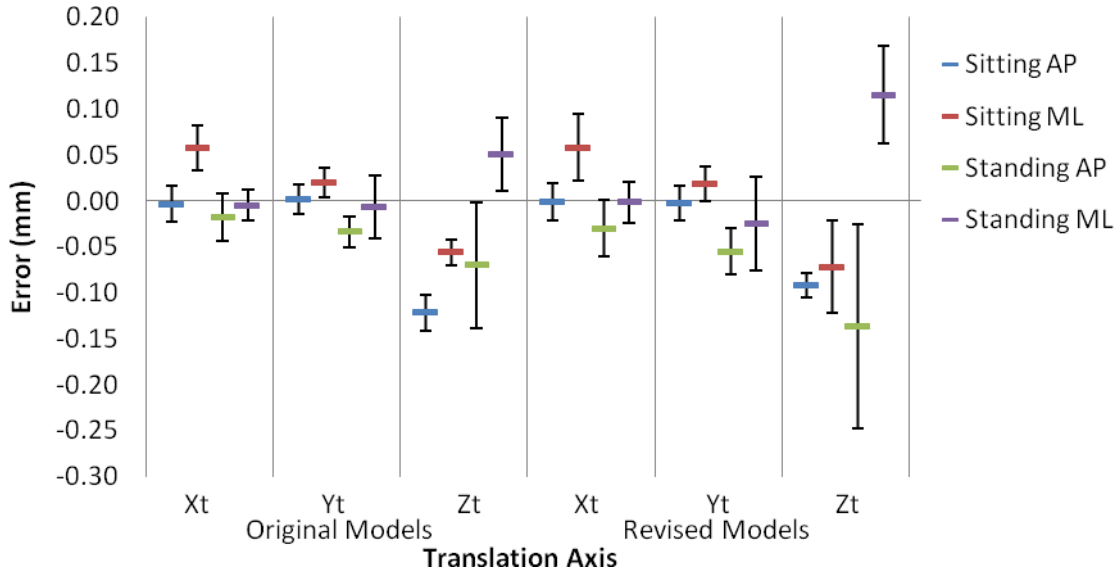

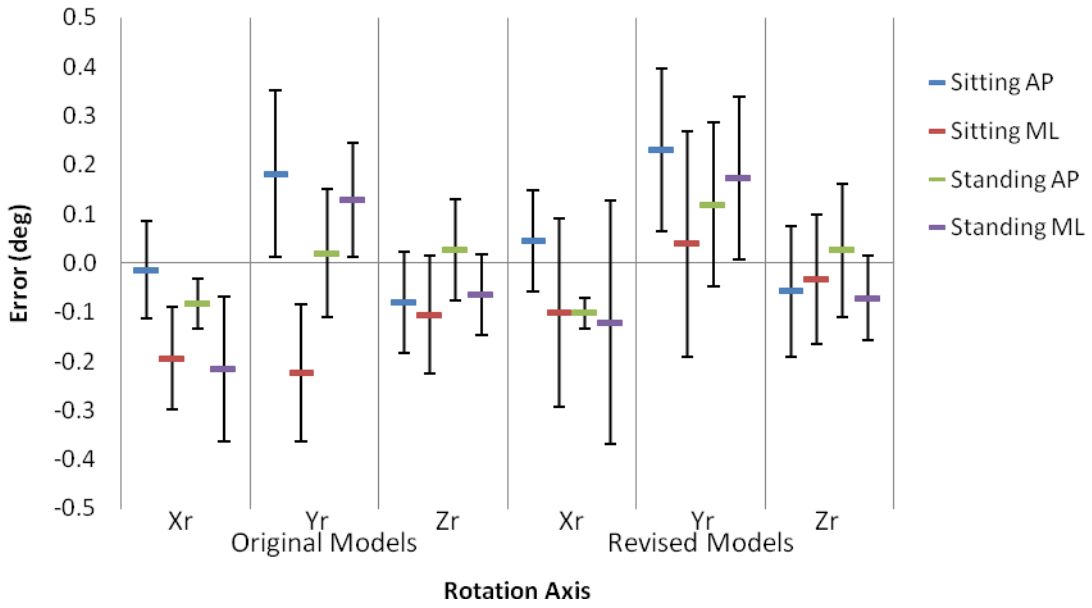

Figure 45: Graphical representation of mean and standard deviation (error bars) of error (measured - actual) for all axes, and all imaging settings A) translation, B) rotation.

The average ½ width of the 95% prediction intervals of error (measured versus actual displacement) were calculated for each axis of motion and each flexion and orientation setting, as described in Section 3.5.3. A total of 48 prediction intervals (6 directions of motion * 4 imaging settings * 2 model types) were computed using SAS Enterprise Guide. Figure 46 is an example of the 95% prediction interval surrounding the linear regression of measured versus actual movement. The mean and standard deviation of the ½ width of the 95% prediction intervals is shown in Figure 47. Tabularized 95% PI data is presented in Appendix F. From Figure 47A, in-plane translation shows reduced PI width compared to out-of-plane translation, for both model types. Similarly in Figure 47B, in-plane rotation shows reduced PI width compared to out-of-plane rotation, particularly rotation about the Y axis.

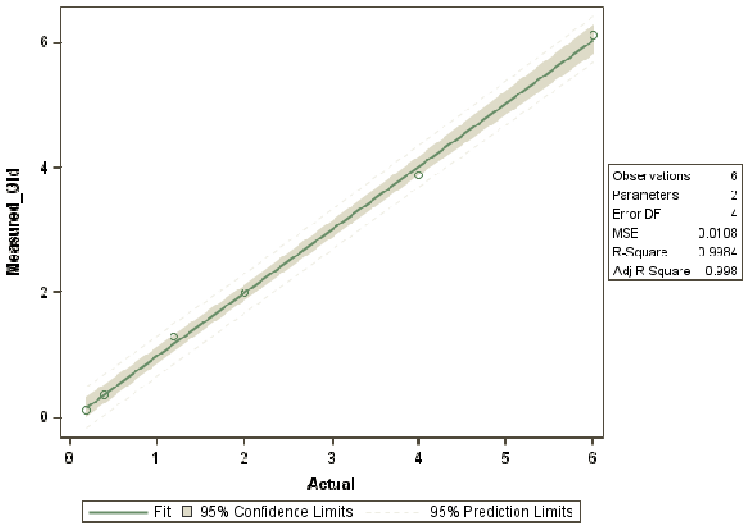

Figure 46: Linear regression of actual to measured rotation about the X axis, showing 95% confidence and prediction intervals of the regression line.

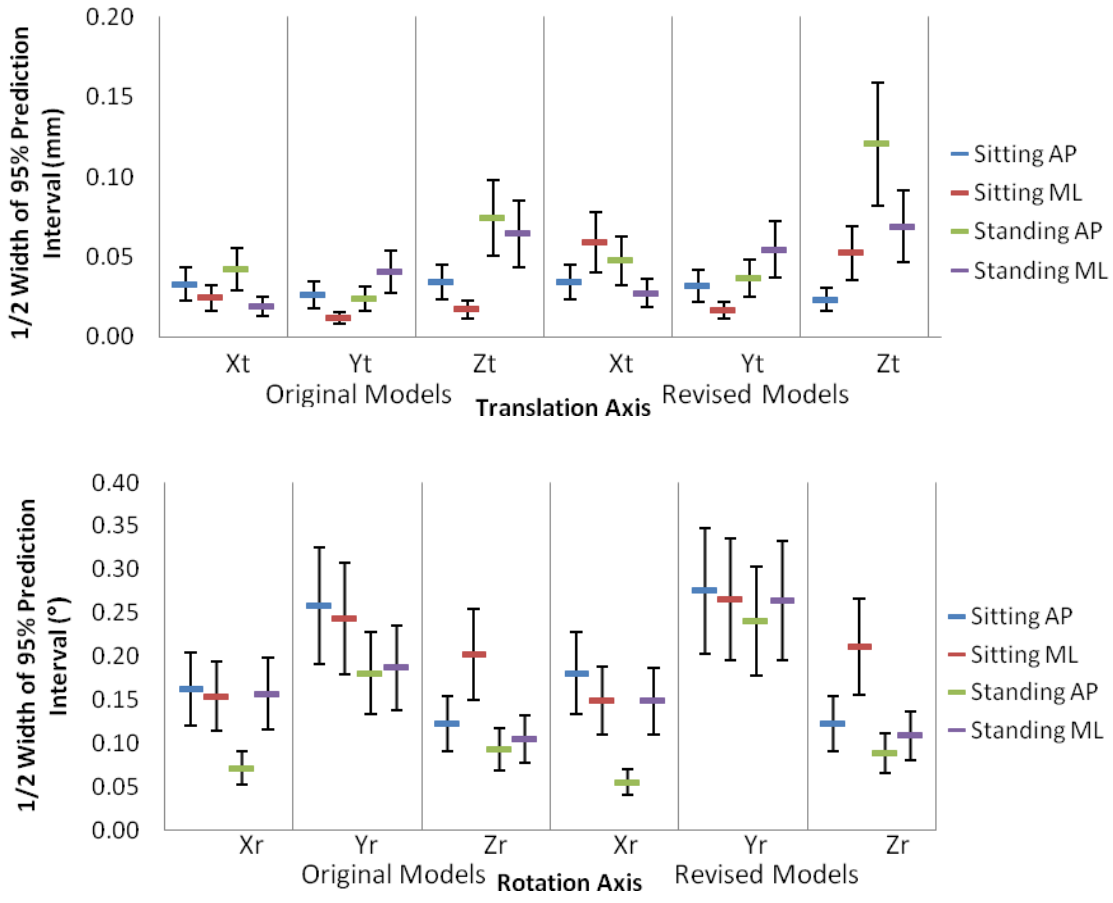

Figure 47: Graphical representation of mean and standard deviation (error bars) of 1/2 the width of the 95% prediction interval of the regression line for A) translation, and B) rotation.

The slope, y-intercept, 95% confidence intervals of each, as well as the R^2 fit of each linear regression was obtained from SAS Enterprise Guide, and tabulated in Appendix F. Table 6 is a summary of the averages of the slope, intercept, and R^2 values for each axis of motion. This data, although useful for describing the closeness of agreement between measured and actual motions, was not analysed in the same manner as the error or 95% prediction intervals. Instead, the regression equation data was used as a visual check for any substantial disagreements between measured and actual motion. From Table 6, we see that Z translation has the highest error of translation in terms of slope, intercept, and R^2. Rotation about the X axis showed high intercept error (furthest from 0.00), but reasonable slope and R^2 values. Rotation about the Y and Z axes had improved intercept and slope values compared to X rotation.

Table 6: Slope, intercept, and R^2 of linear regression, averaged for each axis of motion.

Measured value	Axis	Original Models			Revised Models		
		Slope	Intercept	R^2	Slope	Intercept	R^2
Translation	X	0.999	0.008	0.998	0.986	0.011	0.995
	Y	0.971	0.004	0.998	0.953	-0.001	0.996
	Z	0.951	-0.034	0.992	0.893	-0.013	0.981
Rotation	X	0.988	-0.187	0.999	0.956	0.174	0.999
	Y	1.012	-0.003	0.997	1.042	0.043	0.996
	Z	0.984	0.091	0.999	0.975	0.092	0.999

Analysis of variance was performed on both the mean error and prediction interval widths in a similar fashion to that of the precision experiment with the exception of using interaction plots to determine improvement between the 4 imaging settings, and combinations thereof. The results of the analysis of variance (example ANOVA table shown in Table 3) were combined with the graphical results from the interaction effects plots (ex-

ample shown in Figure 48) in Table 7. A computed F-ratio of greater than the critical F-value of 4.32 indicated a statistically significant difference between the factors. Some cases in Table 7 show significant improvement of a combination of two separate factors (i.e., AP standing in Figure 48B) which indicates that the interaction between these factors showed significant improvement over other combinations of the 2 factors. In some instances, statistical significance is present but no one factor or combination of factors was superior, based on the interaction effects plots.

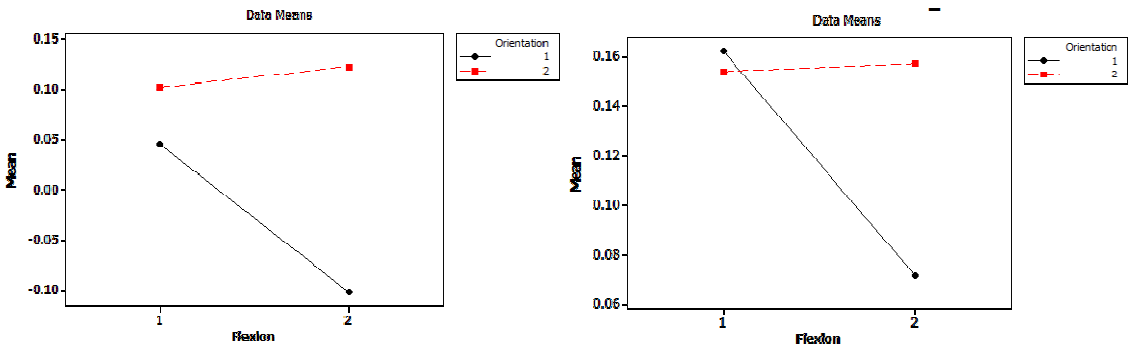

Figure 48: Interaction effects plots showing the interactions of sitting (flexion 1) and standing (flexion 2) with AP (orientation 1) and ML (orientation 2) and the effect on A) mean error, and B) 95% prediction interval width. Rotation about the x axis, original models.

The sitting flexion angle generally showed improved translational accuracy in the Y direction (less error and smaller 95% PI width) compared to the standing flexion angle. ML orientation generally showed improved accuracy for translation in the Y and Z directions, but there was no obvious superiority between the flexion angles. Conversely, the AP orientation and standing flexion angle showed improved accuracy for most directions rotation.

Table 7: Summary of significant improvement between AP/ML and Standing/Sitting factors. Bolded text indicates significantly improved accuracy over the corresponding setting. Critical F value for all factors is 4.32.

		Original Models		Revised Models	
Axis	Factor	Mean Error	Prediction Interval	Mean Error	Prediction Interval
Xt	Orientation	F=17.21	**ML** F=15.51	F=14.43	NS
	Flexion	F=18.67	NS	F=14.60	NS
	Interaction	**AP Sitting ML Standing** F=7.27	NS	**AP Sitting ML Standing** NS	**Standing ML** F=15.70
Yt	Orientation	F=6.19	NS	NS	NS
	Flexion	F=11.49	F=13.82	**Sitting** F=14.39	F=19.25
	Interaction	**AP Sitting ML Standing** NS	**ML Sitting** F=18.73	NS	**ML Sitting** F=11.77
Zt	Orientation	**ML** F=30.38	NS	**ML** F=24.98	NS
	Flexion	F=22.00	**Sitting** F=40.26	F=6.83	**Sitting** F=33.68
	Interaction	NS	NS	F=18.19	**AP Sitting** F=16.75
Xr	Orientation	**AP** F=34.20	F=6.62	NS	NS
	Flexion	NS	F=8.42	NS	F=17.34
	Interaction	NS	**AP Standing** F=9.65	NS	**AP Standing** F=17.23
Yr	Orientation	**AP** F=6.70	NS	NS	NS
	Flexion	NS	**Sitting** F=8.24	NS	NS
	Interaction	**AP Standing** F=20.22	NS	NS	NS
Zr	Orientation	NS	**AP** F=9.77	NS	**AP** F=13.18
	Flexion	NS	**Standing** F=18.85	NS	**Standing** F=20.60
	Interaction	NS	F=5.42	NS	F=5.13

5.3 Physiological Phantom

The volume of condyle-insert overlap (RSA-measured wear) was tabularized for each of the 5 images and 7 image combinations for all 5 pre-worn polyethylene inserts and is shown in Appendix G. Combining the AP Standing and ML Standing RSA wear measurement data accounts for 89.5% +/- 9.9% of the total wear volume as measured by combination 7 (all 5 RSA images), as shown in Figure 49. Whereas, the ML sitting images (ER and IR included) account for between 0.4% and 11.5% of the total wear volume, and between 5.5% and 34.7% when combined (combination 4).

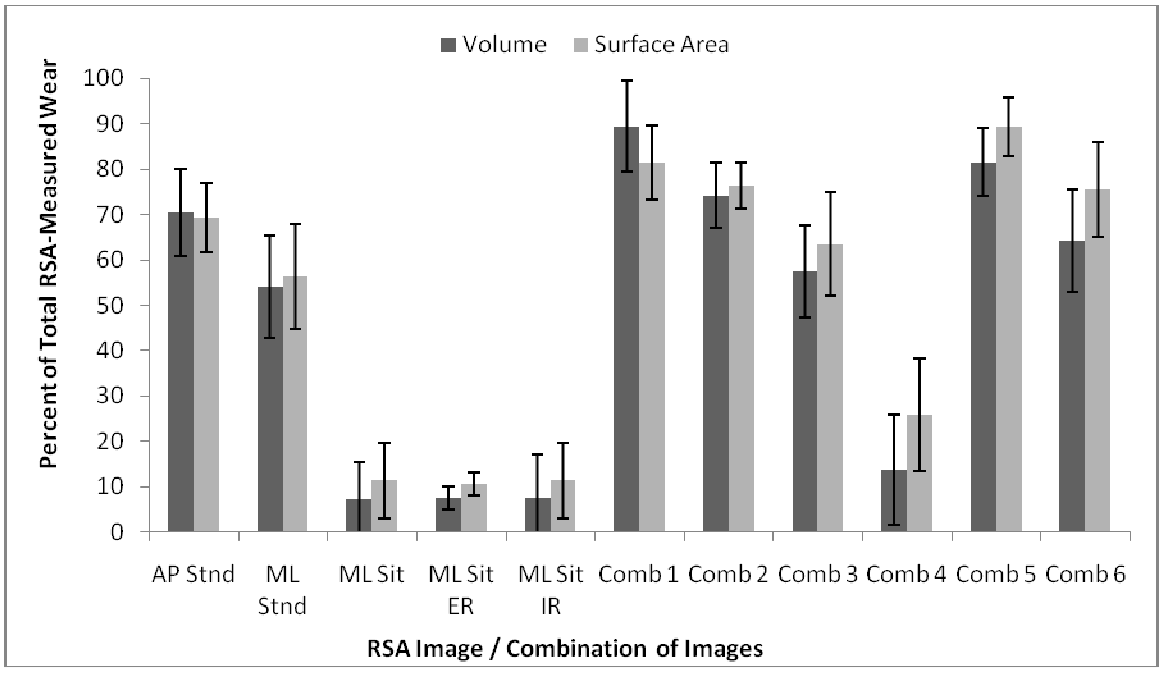

Figure 49: The amount of RSA-measured wear and surface area for each individual RSA image and combination of images, shown as a percentage of the total RSA-measured wear (combination of all images).

.

The "known" wear of each polyethylene insert was determined by comparing a 3-D scanned model of the worn insert to the model of the unworn insert. Only the areas of visible wear on the inserts were used for comparison, as shown in Figure 41, in Section

4.2.4. Total RSA-measured wear volume (combination of all RSA images) was on average only 39.2% of the "known" wear volume (Figure 50).

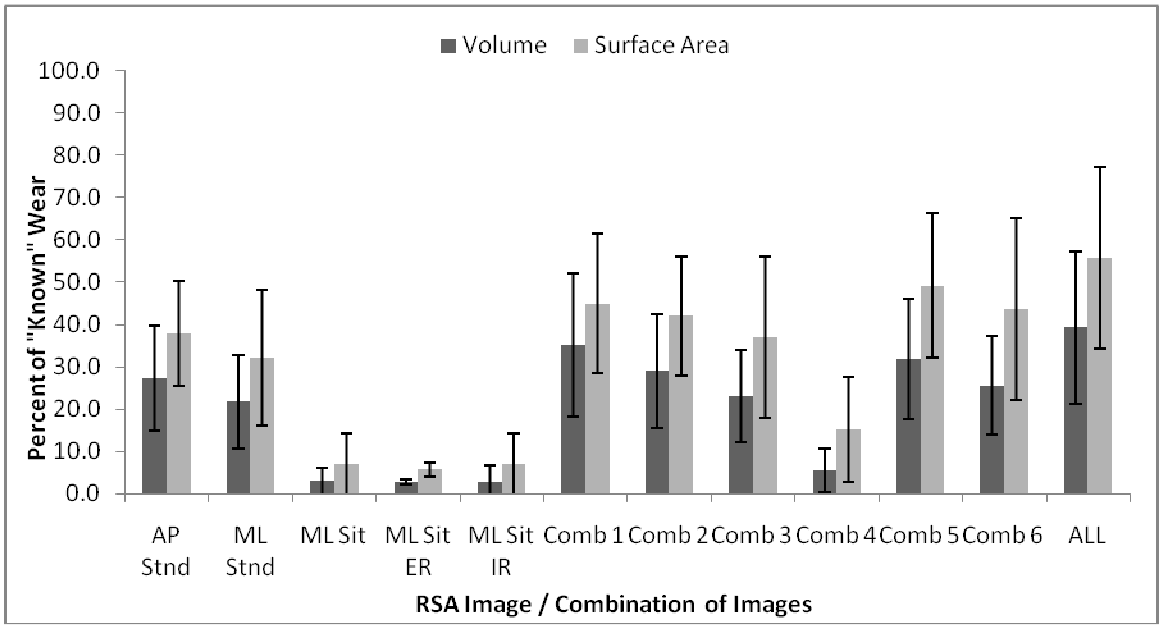

Figure 50: The amount of RSA-measured wear and surface area for each individual RSA image and combination of images, shown as a percentage of the "known" wear.

Cumulative RSA-measured wear areas and "known" wear areas for each of the 5 inserts are shown in Figure 51. Individual RSA-measured wear areas for each image on each insert are presented in Appendix G. The images with sitting (90°) flexion had only small wear areas towards the posterior edge of the insert as well as some wear of the stabilizing post. The standing images covered the largest areas and accounted for the majority of the wear measured. The RSA-measured wear surface areas (left images in Figure 51) were on average 55.8% (range: 32.3% to 80.3%) of the size of the "known" wear surface areas (right images).

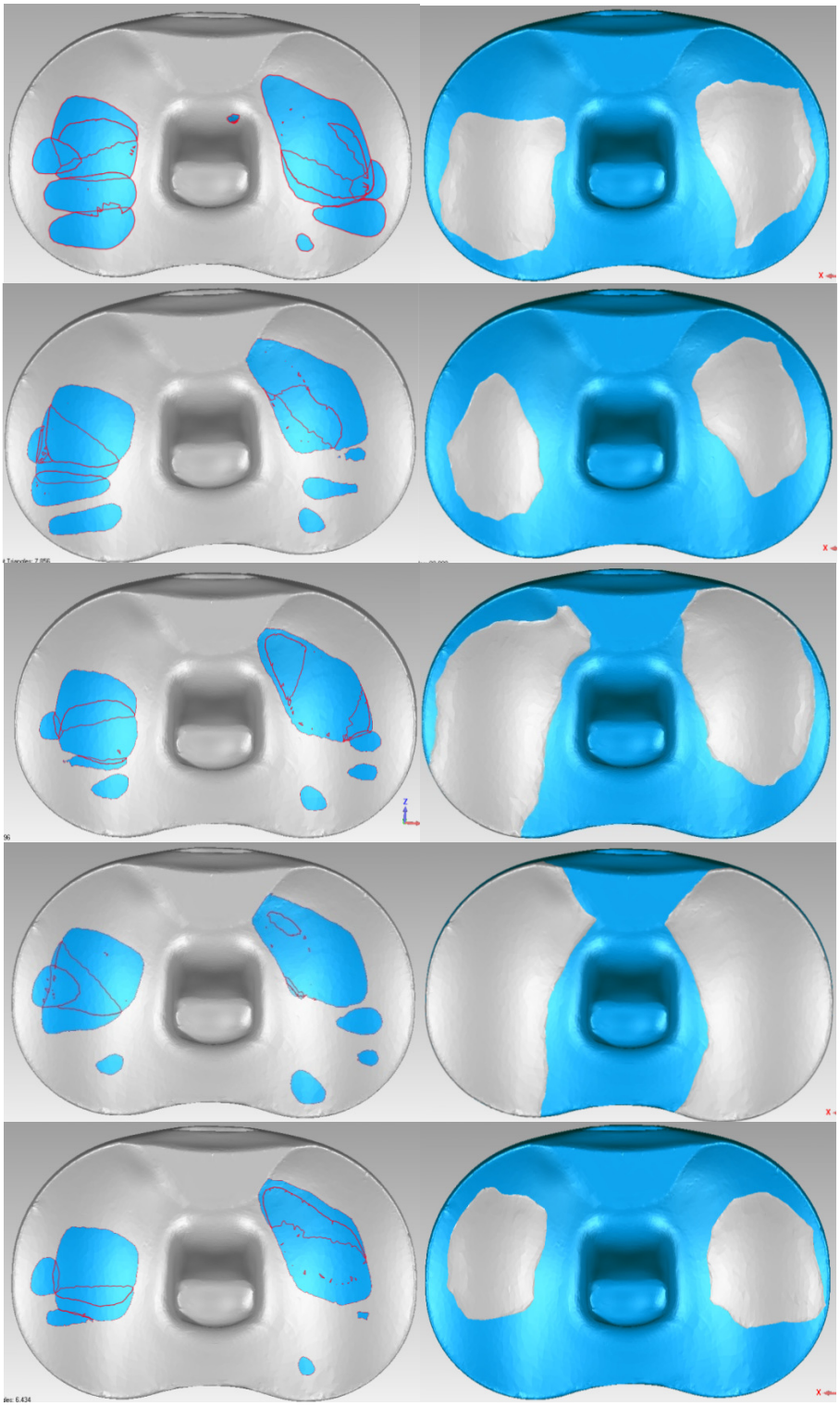

Figure 51: Combined RSA-measured wear pools (in blue) for all 5 inserts (left images), and the “known” wear areas (in grey, right images). In the following order (top to bottom): #620, #625, #633, #1073, #1079.

The clinical information (time *in vivo*, reason for revision, and size of the femoral component) was obtained for each of the 5 pre-worn inserts. The ratio of wear volume to surface area and yearly volumetric wear rate were computed for all images and combinations of the inserts. A summary of this data is shown in Table 8, with the complete data in Appendix G. Combination #1 was included in Table 8 as this combination of images attained approximately 90% of the total RSA-measured wear area. The volume-to-area ratios of the "known" wear areas were substantially greater than the Comb 1 and All entries, with the exception of insert #625.

Table 8: Clinical information, RSA-measured wear volume, and volume-to-area ratio for all inserts. Including; the combination of AP standing and ML standing images (Comb 1), combination of all RSA images (All), and the "known" wear area, of all inserts.

		Insert Number						
		620	625	633	1073	1079	Mean	SD
Time *in vivo* (months)		123	7.4	19.7	13	19	36.4	48.7
Reason for revision		Patella pain	Stage1 infection	Pain	Maltracking, instability	Stiffness	N/A	N/A
Condyle Size		Sz. 4	Sz. 4	Sz. 5	Sz. 5	Sz.4	N/A	N/A
Volumetric RSA-Wear (mm^3)	Comb 1	107.09	102.07	75.65	99.87	72.9	91.52	15.98
	All	149.04	110.97	79.8	106.77	76.58	104.63	29.24
	True	385.10	169.38	237.06	696.4	178.24	333.24	220.62
Volume-to-Surface Area (mm^2)	Comb 1	0.210	0.198	0.167	0.203	0.158	0.187	0.023
	All	0.199	0.172	0.148	0.184	0.149	0.171	0.022
	True	0.414	0.129	0.179	0.389	0.265	0.275	0.125
Volumetric Wear Rate (mm^3/yr)	Comb 1	10.45	165.52	46.08	92.19	46.04	72.06	59.77
	All	14.54	179.95	48.61	98.56	48.37	78.00	64.39
	True	37.57	274.67	144.40	642.83	112.57	242.41	239.69

The repeatability of wear measurement was examined on 3 sets of 10 RSA images and an additional set of unloaded RSA images. However, due to time constraints in the x-ray suite, only 6 of the 10 unloaded images could be obtained. Table 9 is a summary of the mean wear volume and area, with the complete results presented in Appendix G. The

precision (standard deviation) of wear measurement was better than 3.5 mm^3 and 32 mm^2 for volume and area, respectively. Loading of the TKA components in the AP and ML standing positions resulted in a 2.3 to 3.1- fold increase in measured wear compared to the unloaded AP standing case. The volume-to-area ratio remained fairly similar between the three standing cases (Table 9), with the ML sitting case having the lowest volume-to-area ratio.

Table 9: Mean and standard deviation of RSA-measured wear volume and surface area for 4 sets of imaging of the un-worn polyethylene insert.

		Imaging Position			
		AP Stnd (n=10)	ML Stnd (n=10)	ML Sit (n=10)	AP Stnd <5 lb_f (n=6)
Volume (mm^3)	Mean	39.56	29.07	1.78	12.63
	SD	2.67	3.43	0.38	3.46
Surface Area (mm^2)	Mean	660.64	588.31	59.26	258.07
	SD	22.07	29.17	10.20	31.66
Volume-to-Area Ratio		0.060	0.049	0.030	0.049

Chapter 6

Discussion and Conclusions

6.1 Precision Experiment

From the factorial experiment of zero displacement precision, the AP and ML orientations and the standing and sitting knee flexion angles were found to have the greatest precision. The author believes that these findings are robust as two different mbRSA models, four different image comparison techniques, parametric and non-parametric statistical methods, and a weighted scoring table were all used to obtain these findings. On average, in-plane translational precision for model-to-model comparison in the optimal settings was better than 0.025 mm (standard deviation), whereas out-of-plane precision was better than 0.050 mm (original models, all-pairs dataset). The precision of model-to-marker comparison in the optimal settings was very similar at better than 0.035 mm (in-plane) and 0.038 mm (out-of-plane).

It is difficult to compare these results with those of other mbRSA precision studies as here the analysis is of measurement error between the two component models, whereas

other studies analyzed measurement error between component models and a surrounding cluster of markers. Comparison of model pose to a cluster of markers is inherently more precise than model-to-model comparison as marker-based RSA is the current gold standard [69]. However, the results of this precision experiment (Yt: 0.016 mm) have shown that model-to-model comparison precision is well within the range of previously quoted model-to-marker precision for *in vitro* phantom studies; Kaptein et al. 2003 [79] (Yt: 0.045-0.060 mm), and Seehaus et al. 2009 [93] (Yt: 0.009-0.023 mm) (Table 10). This finding suggests that high precision measurement of knee wear is feasible. However, this research was performed in a 'best-case' *in vitro* setup and there is expected to be significant reduction in precision of the mbRSA system in a clinical setting.

Table 10: Summary of published model-to-marker precision (standard deviation in mm) and comparison to the average of the most precise imaging settings (standing, sitting, AP, and ML) of this research. Original models, all-pairs dataset.

Author	N	Component	Xt (mm)	Yt (mm)	Zt (mm)	Xr (°)	Yr (°)	Zr (°)
Kaptein 2003	9	Tibial	0.062	0.06	0.088	0.089	0.172	0.045
		Femoral	0.047	0.045	0.138	0.058	0.104	0.027
Seehaus 2009	10	Tibial	0.012	0.023	0.049	0.027	0.141	0.012
		Femoral	0.013	0.009	0.037	0.026	0.027	0.019
Gascoyne 2012	36	Difference b/w both	0.019	0.016	0.034	0.060	0.156	0.050

The original hypothesis for this experiment was that lateral imaging of the TKA components, particularly at 60° offset, would show greater precision due to the appearance of the more discrete, angular inter-condyle box of the femoral component. However, just the opposite was shown with this experiment, with the exception of the ML orientation. This unexpected result could possibly be explained by a number of different factors, which are discussed below.

The technique employed to reconstruct the scanned TKA component models may have reduced the accuracy of the backside features of the femoral condyles and tibial tray. Five thousand elements is the recommended size of reverse engineered models for use in mbRSA [79] which limits the achievable accuracy of the reconstructed models. As mentioned in Section 2.3.2, the TKA models were initially ~1,000,000 elements before simplification, and reduction to <0.5% of their original size was shown to have a substantial effect on the shape of the model, as shown in Figure 17 and Figure 18 above. The effect of model simplification is particularly evident at the edges and sharp corners of the components. A similar effect can be seen in Figure 1 of a study performed by Hurschler et al. 2009 [108] on a mobile-bearing tibial tray.

The effect that model reconstruction technique has on the accuracy of the RE model can be directly seen in the difference in precision between the original models and the revised models. The original models had an average of 22% less error (improved precision) than the revised models (all-pairs data). Additionally, the pose estimation error in mbRSA (blue error lines in Figure 33B) was typically 45% (tibial tray) and 4.5% (femoral condyles) less for the original models compared to the revised models. The main difference between these two sets of models was simply the application of a “fix boundaries” option during mesh decimation.

The penetrative nature of x-rays may have also contributed to error in the 30° and 60° offset orientations, as the backside features of the femoral condyles and the post-shoulders of the tibial tray are composed of thinner metal than that of the rest of the components. The x-rays may have penetrated the edges of these thinner areas resulting in a

less well defined radiographic outline of the components. However, this effect has not been proven experimentally.

Flexion of the knee also showed somewhat unexpected results as both the standing and sitting flexion angles showed statistically improved precision compared to the intermediary 45° flexion angle. As well, the standing flexion angle was shown to have slightly better precision than the sitting flexion angle. This result was unexpected as Ijsseldijk et al. 2011 [131] found that precision decreased with increasing knee flexion. However, Ijsseldijk did not examine knee flexion beyond 45° (maximum knee flexion during walking).

Difference in precision due to knee flexion may be explained by both the model geometry of the femoral condyles in the flexed position and the RE model reconstruction technique. In the standing position, the external contour of the implant is a projection of the outer curved edges of the component as well as the lower contour of the condyles. In the 45° flexed and sitting positions, the projected contour consists of some portions of the sharp backside edges (Figure 52) which, as mentioned above, were shown to reduce overall precision in the 30° and 60° offset orientations. These sharp backside edges may have reduced precision due to the combining of multiple sets of 3-D scans into a single model, as well as the drastic reduction of mesh elements required for mbRSA. Future research must examine the influence of performing an edge-sharpening algorithm (available in Geomagic Studio) to improve the shape of the edges, on the accuracy of mbRSA in the 30° and 60° offsets orientations and 45° flexion angle.

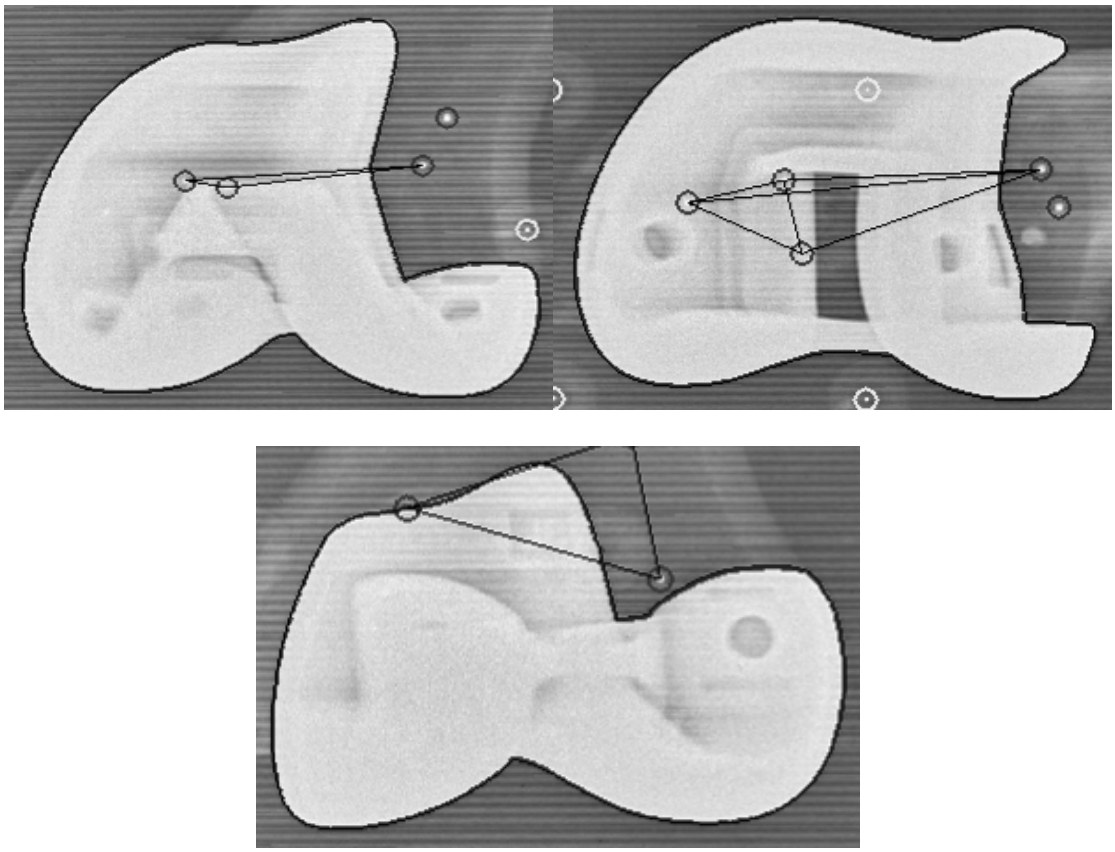

Figure 52: A) 45° flexion, B) 90° (sitting) flexion, C) 0° (standing) flexion of the femoral condyles in the AP orientation. Note the straight edges present in A) and B).

A possible explanation of reduced precision is that in the 30° and 60° orientations, the implant contours are made up of component features that are all on a similar plane, thus providing little pose information on the posterior or lateral features of the TKA components. For example, in the case of the left focus image (Figure 53) for the 60° offset case, the detectable contour on the radiograph is basically a projection of the side view of the femoral component. The structures making up the contour are mainly from the medial side of the implant, with very little from the lateral side of the component. The lack of lateral-side features may increase the potential for pose error, even when combined with the pose information from the opposite radiograph. However, this hypothesis does not

explain the reduction of precision in the 30° offset case, as shown in Figure 54. In this case, there is excellent presence of medial, lateral, anterior and posterior features of the implant making up the overall contour.

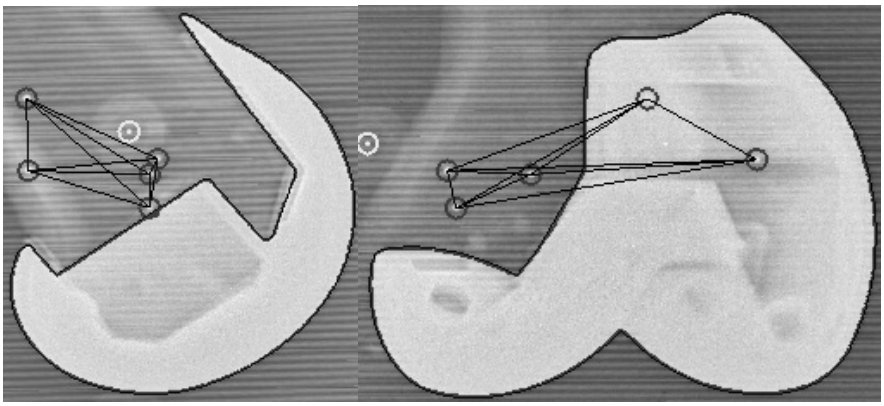

Figure 53: Left and right focus RSA images of the femoral component in the 60° offset orientation, 45° flexion.

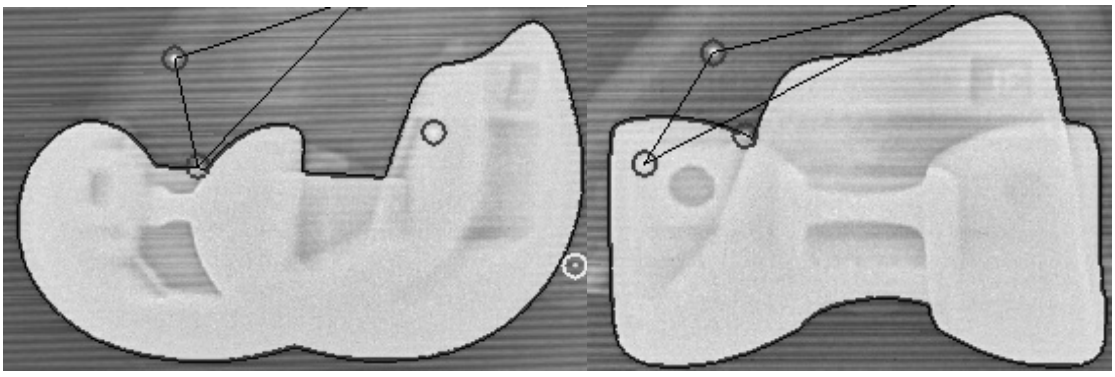

Figure 54: Left and right focus RSA images of the femoral component in the 30° offset orientation, standing flexion.

The appearance of the radio-opaque Versabond bone cement in the RSA images reduced the amount of tibial tray contour that was available for mbRSA contour selection. This reduction of useable x-ray contour may have reduced the accuracy of the pose estimation in mbRSA. Hurschler et al., 2008 [92] showed that reduction of model contour by ~25% has a worsening effect of 0.005 to 0.065 mm on the accuracy of pose estimation (95% confidence interval) depending on the axis of motion. Accordingly, use of radio-

lucent bone cement would allow the RSA analyzer to use the full amount of tibial tray contour, which may increase the precision/accuracy of pose estimation.

A definite conclusion of this research is that a 5000 element model may be too inaccurate for the measurement of minute amounts of wear. It may be beneficial to try 10000 or 50000 element models to determine if increasing the mesh size will significantly improve precision. Kaptein et al. 2003 [79] showed that a 5000 element model had superior precision/accuracy to models with fewer elements; however, they did not show at what point this improvement becomes asymptotic with increasing mesh size. The reason for selecting 5000 element mesh size is that pose estimation takes time, but with an Intel Core2 1.86 GHz computer (2 GB of RAM) it took between 3 and 10 seconds per implant component to compute the pose. Therefore, one would expect pose estimation with a 50000 element model to take 30 seconds to 2 minutes, which is not an unreasonable delay, particularly in a clinical study.

6.2 Accuracy Experiment

The accuracy experiment examined translational and rotational accuracy over an incremental range of displacements. AP and ML imaging orientations in addition to standing and sitting knee flexion angles were selected as the experimental factors based on the results of the precision experiment. In-plane translational accuracy (standard deviation) was better than 0.035 mm (original models) and 0.051 mm (revised models), and in-plane rotational accuracy was better than 0.08° (original models) and 0.10° (revised models). The results of the analysis of variance did not show superiority between the 4 imaging factors.

Translational accuracy along the Y and Z axes was significantly better for the sitting and ML factors, whereas X and Z rotation as well as X translation showed significantly improved accuracy for the standing and AP factors. From these results, sitting versus standing flexion and AP versus ML orientation, have been shown to be virtually equivalent in terms of mbRSA accuracy.

Model-to-marker accuracy of this research is similar to that of previous mbRSA accuracy studies (Table 11). However, similar to the precision experiment, it is difficult to compare the model-to-model results of this research with other studies. Nevertheless, the model-to-model accuracy determined from this research (Y_t: -0.005 ± 0.021 mm) is well within the range of model-to-marker accuracy from previously published *in vitro* phantom studies; Kaptein et al., 2007 (Y_t: 0.003 ± 0.031 mm) [90], Kaptein et al. 2003 (Y_t: -0.003 ± 0.019 mm) [79], and Seehaus et al. 2009 (Y_t: -0.001 ± 0.012) [93] (Table 11).

Table 11: Summary of published model-based RSA accuracy studies (model-to-marker) and comparison to this research (model-to-model and model-to-marker accuracy), average values for all flexion and orientations settings, original models, n=24 in all cases (6 comparisons * 4 imaging settings).

Author	N	Component	Metric	Xt (mm)	Yt (mm)	Zt (mm)	Xr (°)	Yr (°)	Zr (°)
Kaptein 2007	9	Tibial	Mean	0.031	0.003	-0.01	-0.02	-0.012	-0.005
			SD	0.079	0.031	0.107	0.104	0.21	0.098
Kaptein 2003	7	Tibial	Mean	0.002	-0.003	0.036	-0.017	-0.021	0.006
			SD	0.04	0.019	0.08	0.118	0.057	0.027
		Femoral	Mean	-0.004	-0.006	-0.019	0	0.017	0
			SD	0.028	0.029	0.147	0.067	0.044	0.058
Seehaus 2009	10	Tibial	Mean	0.037	-0.005	0.048	0.028	0.007	0.029
			SD	0.022	0.019	0.032	0.047	0.123	0.028
		Femoral	Mean	0.032	-0.001	-0.042	-0.055	-0.06	0.02
			SD	0.028	0.012	0.037	0.033	0.029	0.036
Gascoyne 2012	24	Model-to-model	Mean	0.008	-0.005	-0.049	-0.127	0.026	-0.056
			SD	0.022	0.021	0.036	0.100	0.139	0.102
Gascoyne 2012	144	Model-to-marker	Mean	-0.003	-0.009	0.005	0.030	-0.016	-0.001
			SD	0.025	0.024	0.039	0.082	0.118	0.060

Other clinical studies have compared marker-based to model-based RSA in the same set of RSA radiographs to determine the closeness of agreement between the gold standard marker-based RSA and model-based RSA. Hurschler et al., 2008 [92] found Y-directional agreement (Mean ± SD) to be -0.017±0.039 and -0.023±0.038 mm, tibial and femoral components respectively. Similarly, Kaptein 2007 examined double examinations of 44 patients using mbRSA and found Y-directional accuracy (Mean ± SD) to be -0.003±0.058 mm for a tibial component. The accuracy reported by these studies is noticeably reduced compared to the phantom studies mentioned above due to additional error encountered in clinical studies. Therefore, we expect to see a reduction in accuracy when our mbRSA results are applied in a clinical setting.

Only one published study by Ijsseldijk et al. 2011 [131] has reported the translational model-to-model accuracy of mbRSA by comparing the pose of the tibial tray to the pose of the femoral condyles. Ijsseldijk found Y-directional accuracy (standard deviation of measurement error) of between 0.04 mm and 0.115 mm for two prosthesis models (RE scanned) for all flexion angles. This research found improved accuracy in the Y direction of between 0.017 mm and 0.035 mm for the original models, and 0.019 and 0.051 mm for the revised models. One difference between the results here and those of Ijsseldijk, is that we compared positions of the model centroids, whereas Ijsseldijk measured the lowest point of the medial condyle to the plane of the tibial tray when a 1.0 cm Perspex spacer (0.05 mm tolerance) was placed in between.

This experiment revealed the accuracy of mbRSA to be generally less than the precision. This increase in error when measuring accuracy is expected since relative motion between the components has been introduced as an added variable. The source of this ad-

ditional error stems largely from inaccuracies and non-linearity of the micro manipulators. The linear translation slides used in this experiment have a reported in-line accuracy of 0.002 mm, which due to added load and fixtures, was increased to 0.005 mm. The rotation table did not have a reported accuracy tolerance. Instead, the assumed tolerance was 0.2°, hence the reason for rotating in increments no less than this amount. However, additional error can arise from bending or warping of the components, wobble or non-linearity of the translation/rotation tables, all of which can be particularly exacerbated under loaded conditions, as was the case for this experiment. There was inherent difficulty in rigidly mounting the tibia to the micromanipulators, and thus additional components and fixtures were needed to accomplish this, resulting in an off-centered load.

Alignment of the phantom frame during the accuracy experiment was also a concern, as displacement not parallel to the axes of motion of the RSA calibration box would result in a non-linear measurement. However, using a conservative maximum estimate of 5° of malalignment (<1" of malalignment across the 22" width of the phantom frame) over 1 mm of displacement results in 0.996 mm of displacement in the desired direction. Therefore, because alignment of the phantom frame was carefully corrected for each set of radiographs to an approximate alignment error of 1/8", even with the calibration error of mbRSA and non-parallel imaging plates, the alignment error would be much less than the estimate of 1". Therefore, malalignment of the phantom frame was assumed to be a negligible effect.

Defining the measure of accuracy was also a challenge for this experiment. Quantification of precision is quite simple as it corresponds to the repeatability of a measurement (standard deviation). Accuracy on the other hand, must take into account both repeatabil-

ity of measurement and how close the measurement is to the true value. For the purpose of comparison to literature values [90, 96, 105, 131], we have reported both the ½ width of the mean 95% prediction interval as well as the mean and standard deviation of measurement error.

This accuracy experiment is akin to that of a linear gauge study, in which a device is tested over a range of linear values. Our experiment differs, in that measurements were performed at increasing increments (close to doubled increments) and only one measurement was performed at each increment. This has the effect of altering the leverage of each point along the linear motion line, with those points at 1.0 mm and 6.0° having the greatest leverage, which may greatly affect the regression line. As well, only one measurement at each increment does not provide an estimate of the average measurement at that increment. Random error may cause a single measurement, (e.g. the reference image) to be off by up to 0.1 mm as was sometimes the case for measurement of translation in the Z-direction. Due to time restrictions, multiple radiographs at each increment, as well as a large number of evenly spaced increments were not feasible for this project.

6.3 Physiological Experiment

AP standing and ML standing were the most valuable imaging positions in terms of measured wear volume. Combining these two images resulted in approximately 90% of the total RSA-measured wear. This suggests that the best RSA wear measurement technique, with a minimum x-ray exposure to the patient, is to obtain two standing images in

the AP and ML orientation. Conversely, sitting RSA images were not useful for wear measurement as condyle-insert contact areas were towards the posterior edge of the insert. These contact areas were not only much smaller than the "known" contact areas, but they were not typically within the visible "known" wear areas of the inserts. Accordingly, interpolation between the sitting ML wear pools was not performed.

The "known" wear volume was on average 2.5 times greater (range: 1.5 to 6.5) than the wear volume measured by RSA in all 5 pre-worn inserts. This large discrepancy between "known" and measured wear volume indicates that the method of mbRSA wear analysis employed in this research is inadequate. However, the surface area of the "known" wear was measured to be, on average, 1.8 times greater (range: 1.2 to 3.1) than the area measured by RSA, which suggests that the majority of wear volume discrepancy is a result of insufficient coverage of the articulating surfaces of the pre-worn insert. Furthermore, the true *in vivo* contact between the condyles and the insert were likely not accurately re-created with the physiological phantom for a number of reasons described in the following paragraphs.

The first reason for insufficient surface coverage was that the *in vivo* femoral TKA component (in the patient) was of a larger size than the component used in the phantom. Of the 5 retrieved inserts, three articulated against size 4 femoral components and the other two against size 5 components. A large femoral component will create a much larger wear area which cannot be matched by a smaller, size 3 component (Figure 55). Due to time and monetary constraints, it was not possible to obtain multiple sizes of TKA components for this research.

Figure 55: A) The size 3 femoral component used in the physiological phantom compared to a B) size 4 component used *in vivo* (3 patients) and a C) size 5 component used *in vivo* (2 patients). Note the size of the components with respect to the tibial insert.

A second possible explanation for the lack of articulation area coverage is that only standing and sitting flexions were examined using the physiological phantom. The two previous studies of knee wear using RSA have examined flexion angles of 0°, 30°, and 45° [131] and 0°, 15°, 30°, 45°, and 60° [49], which is the approximate range of flexion during level walking [132]. This research did not apply these intermediate flexion angles of 15°, 30°, and 60° to the physiological phantom due to time constraints and the fact that the 45° flexion angle was found to reduce the precision of the mbRSA system.

The femoral component was slightly misaligned when cemented onto the Sawbones femur with a 5-10° anterior tilt (Figure 56A), resulting in the "standing" position of the components representing hyper-extension of the knee, instead of a comfortable standing position. The effect of this anterior tilt is seen in the standing examinations in which the RSA-measured wear areas tended to be located towards the anterior edge of the insert (Figure 56B). This anterior tilt was partially due to a size mismatch between the TKA component and the Sawbones femur. For future research an appropriately sized artificial femur must be obtained and re-cemented to correct this anterior tilt.

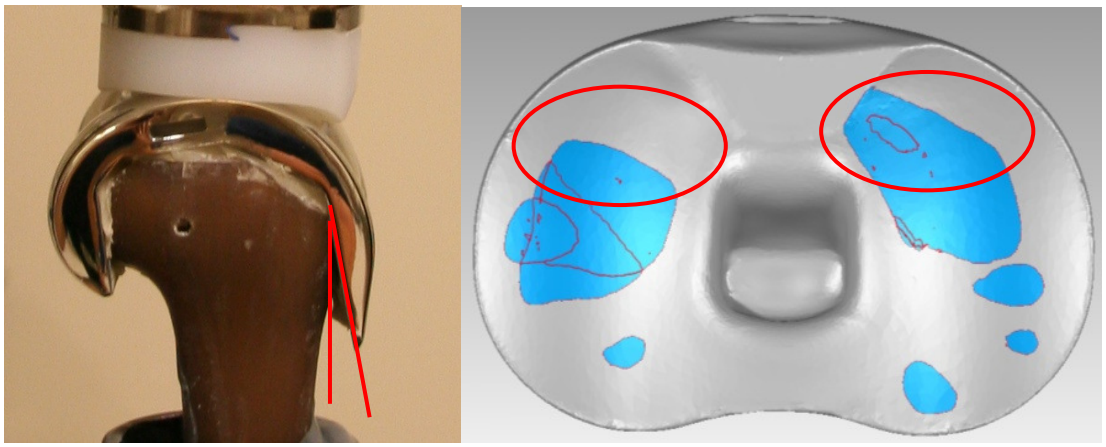

Figure 56: A) Anterior tilt of the femoral component with respect to the femur, B) RSA-measured wear areas located towards the anterior edge (top of image) of the polyethylene insert.

Finally, the pivot point of the femur on the physiological phantom was located close to but not directly perpendicular to the midpoint between the condyles (Figure 57A). This off centered pivot caused a moment on the femur which was countered by contact of the medial condyle against the lateral side of the medial insert surface (Figure 57B). The effect of this countering force can be seen in the standing RSA-measured wear areas of all 5 polyethylene inserts (Figure 51 in Section 5.3). For future research with this phantom, the pivot point of the femur must be located along the midpoint line of the condyles.

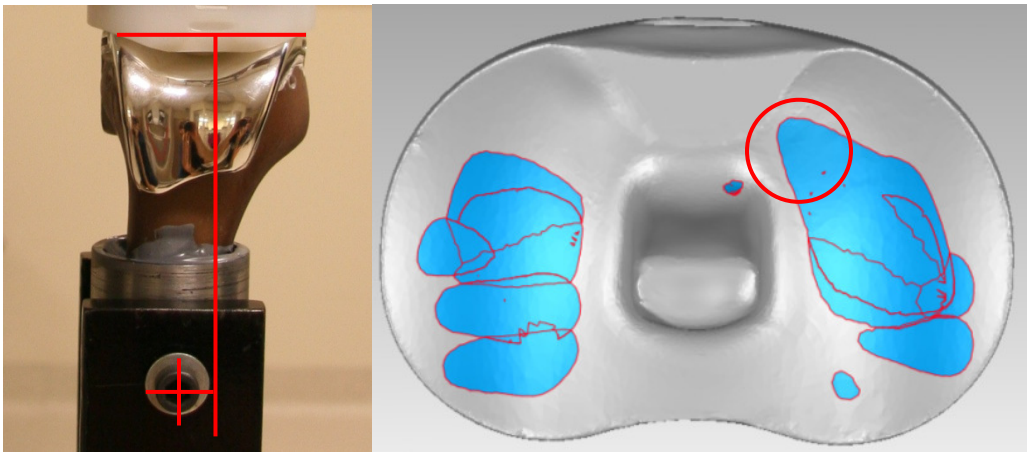

Figure 57: A) The pivot point of the femur mount off-centered from the midpoint between the femoral condyles, B) wear of the lateral edge of the medial articulating surface on the #620 pre-worn insert (circle).

The average yearly volumetric wear rate was calculated as 242.4 mm^3/yr (SD: 239.7 mm^3/yr) based on the "known" wear volume. However, one retrieved insert underwent a very large amount of wear (696.4 mm^3) in a short period of time (13 months), which may have resulted from maltracking of the components (recorded as the reason for revision). When excluding this insert, the average yearly wear rate is 142.3 mm^3/yr (SD: 99.0 mm^3/yr), which is similar to the 100 mm^3/yr rate reported by Gill et al., 2006 [49]. It is important to also consider that the "known" wear measured on each insert is an estimation based on comparison to an unworn reference, in which the alignment between the two models likely introduced some error. The areas of visible wear were designated on the inserts and manually selected in Geomagic Studio by the author. Additionally, the effect of polyethylene cold-flow in the pre-worn inserts was not accounted for. Finally, the inserts were retrieved from poor functioning TKAs, and therefore may not represent the wear rate of well functioning TKAs.

The interference fit of the polyethylene insert and the locking mechanism of the tibial tray is also a potential source of error. The sharp internal contours of the locking mechanisms on both the insert and the tibial are very difficult to 3-dimensionaly scan, making it difficult to attain the true fit between these two components. Aligning the individual component models to a 3-D scan of the assembled components is also subject to error from the alignment of the models in Geomagic Studio.

The insert-tray fit used in this research was examined more closely by taking cross sectional slices along the interface of the two components. The bottom surface of the insert was found to be below the tray surface. However, moving the insert up to the level of the tray surface introduced an abnormal amount of insert-condyle overlap as this analysis was performed on an unloaded image of the TKA phantom. This overlap between the insert and tibial tray surface highlights the difficulty of accurately reverse engineering the interface between these components. Accordingly, the initial insert-tray fit was used for the all wear analyses.

Analysis of the penetration depth of the condyles into the polyethylene surface was not performed in this research, as penetration depth could not be accurately measured in Geomagic Studio. Additionally, wear depth was manually measured on each polyethylene insert and was performed using a micrometer tool with a flat measurement barrel. For future research, a round-tipped barrel is needed to accurately measure the lowest point on the concave polyethylene surface.

6.4 Limitations

The above experiments are generally limited by the fact that they are *in vitro* phantom experiments. In contrast, clinical RSA studies are performed on patient knees in which soft tissue attenuation of the x-rays, patient movement, RSA setup differences, and non-identical TKA components all contribute to overall error. Soft tissue attenuation was not introduced in the above experiments as this was an added variable which was believed to be more difficult to control between different orientations and flexions of the knee joint. The radiographs taken in the precision and accuracy experiment were obtained in four sets due to the availability of the x-ray suite, modifications to the phantom frame and bone mounts, and re-takes of some sets of x-rays due to erroneous images. In order to make the reported precision and accuracy values more transferrable to clinical RSA, one would have to re-assemble the RSA setup between each x-ray, a very time consuming process.

A limitation of this research is that only one TKA model/manufacturer was analyzed. As well, the exact same TKA components that were analyzed in mbRSA were scanned using a high-accuracy laser scanner. It is likely not possible to scan each and every component that is implanted in a clinical study. Typically, researchers will use a manufacturer CAD model of the implant or a reverse engineered scan of a single implant, but never the exact component that is being imaged. This means that our precision and accuracy experiments were for the most ideal case as there is no addition of inter-component differences resulting from manufacturing tolerances. Future research must examine the effect

of dimensional differences between the manufactured components as well as between the manufacturer's CAD models.

The accuracy of mbRSA is based upon the accuracy of the reverse engineering of the TKA components. The 3-dimensional scanning technique (method and settings) used in this experiment has yet to be validated. In particular, the effect of the developer spray coating on the external dimensions of the components must be examined. The coating spray is helpful, but not critical, when scanning highly reflective surfaces such as the polished articular surfaces of the femoral condyles and the top-side of the tibial tray. However, the polyethylene inserts must be coated with an opaque material in order to prevent penetration of the scanning laser into the plastic, which would result in reduced external dimensions. It is the author's belief that that the addition of an opaque coating will likely increase the overall dimensions of the object being scanned, which in turn would result in an overestimation of the insert-condyle overlap (wear).

This research involved a large amount of RE model alignment and manipulation in Geomagic Studio. As with any alignment algorithm, there is always some amount of misalignment that cannot be corrected for. This is an additional source of error that must be further examined in order to determine the true effect on the measurement of wear.

When examining polyethylene wear in a TKA using a single RSA image-pair, one cannot distinguish between wear, plastic cold-flow (creep), and deformation of the polyethylene due to loading. Creep is not wear, in that it does not remove particles, but it does result in a thinning of the PE insert which is significant when estimating survivorship based on wear rates. The effect of plastic cold flow can be accounted for through multiple follow-up examinations over a period of 2 or more years. Cold flow has been shown to

essentially cease within 1 year *in vivo* [59]. Therefore, the difference in wear volume between year 1 and year 2 can be used as an estimate of the true rate of polyethylene wear.

Similar to plastic cold-flow, the effect of deformation of the polyethylene under load can also be accounted for, provided that the patients apply a similar force to their TKA at each follow-up examination. This can be ensured by consistent patient positioning and instruction throughout the clinical research study. Other potential errors arising from positioning of the insert within the tray, alignment of models, or RE discrepancies, can also be accounted for provided these initial errors are kept constant throughout the clinical study.

6.5 Conclusions

The purpose of the first experiment of this research was to determine the optimal patient-radiograph positioning and to obtain 'best-case' precision and accuracy of the mbRSA system. By limiting the effect of RSA setup error, patient movement, soft tissue attenuation, and RE model error, we were able to directly compare the 4 imaging orientations and 3 flexion angles. It is hoped that the findings from this experiment will translate to clinical RSA experiments.

Arguably, the most important conclusion from the precision/accuracy experiment is that AP and ML imaging orientations are for the most part interchangeable in terms of precision and accuracy. Although there are few published RSA studies of total knee replacements, the reported imaging orientation is antero-posterior [90, 92, 96, 108] with the

exception of Gill et al., 2006 [49] whom used a custom-designed calibration frame (120° between x-rays, centered about the AP axis) and Trozzi et al., 2008 [104] whom used a bi-planar calibration frame (1 x-ray along AP axis, the other along ML axis of the knee). The difficulty of AP orientation is that flexion of the knee joint is difficult to achieve, particularly beyond 45° flexion as the contour of the tibial tray becomes overlapped with the femoral condyles (when in a squatting stance) or the calibration cage is obstructive to the patient when the tibia is kept vertical (to prevent component overlap). Overlap of the tibial tray contour with the femoral condyles results in the removal of a substantial section of the model contours, which has been shown by Hurschler et al. 2008 [92] to increase pose estimation error by up to 0.06 mm (95% confidence interval at 25% reduction of contour).

In contrast to AP imaging orientation, ML orientation allows for full flexion of the knee joint while the necessary spacing between the TKA components is maintained. Given that similar precision and accuracy is obtained in ML orientation as AP orientation, there is the added benefit of greater knee flexion in the lateral orientation which allows researchers to examine polyethylene wear through a more complete range of knee motion. As shown in the physiological experiment, high flexion of the knee (90°) in a posterior-stabilised total knee replacement will constrain condyle-insert contact area towards the posterior edge of the insert. As a result, the wear measured on the pre-worn inserts was generally not within the true wear areas of the inserts. For the same reason, internal/external rotation of the tibia was unsuccessful for wear measurement. However, high flexion RSA exams have the added benefit of being able to determine wear of the posterior stabilizing post. Visible wear was noted on all pre-worn inserts and was meas-

ured on the majority of high-flexion RSA images, but this was not examined in this research.

It appears as though previous researchers [49, 131] are correct that knee flexion of up to 45° is useful for wear measurement. It is possible that cruciate-retaining TKA designs may benefit from high flexion and internal/external rotation of the tibia, but this has yet to be examined. The author hypothesizes that the most accurate imaging technique will involve the combination of three RSA examinations of a hyper-flexed knee, a normal standing knee, and 15-20° of flexion. Combination of these data is believed to cover the majority of the insert surface.

A recommendation of this research is to increase the number of elements in the RE models that are used for pose estimation in mbRSA. As described above, significant dimensional inaccuracies resulted from the reduction in mesh elements from over 1 million, to less than 5000. The effect of these inaccuracies must be examined in future research.

The effort involved in measuring polyethylene wear in a TKA is significantly greater than that of a total hip replacement. High quality reverse engineering of all components is required for all sizes of the components, and all thicknesses of the polyethylene bearing. Multiple RSA radiographs are required at each patient follow-up. The RE models used for analysis of wear must be aligned to the mbRSA-specific models. The RSA pose data must be entered into a 3-dimensional modelling program for each individual RSA examination. A Boolean Intersect operation must be performed and the volume of condyle-insert overlap and/or penetration depth for each condyle must be measured. This process must then be repeated for each follow-up for each patient. All aspects are significantly more involved than the analysis of wear in a total hip replacement, resulting in greater

initialization costs (purchasing and reverse engineering of all sizes of components), and continuation costs (radiology time, mbRSA model manipulation, and analysis time). However, this technique has significant potential to measure wear in a total knee replacement after 2-3 years *in vivo*. Additionally, it has the advantage of reporting volumetric wear, which is of greater importance to the prevention of wear particle induced osteolysis.

6.6 Future Work

A large amount of additional work has become apparent throughout the completion of this thesis. To begin, the effect of the developer spray coating on the accuracy of reverse engineering of the component models must be examined. If it is discovered that the coating significantly effects the dimensions of the RE model, an alternative must be used. Carbon sputter coating is one possibility in which an electrical current is passed through a thin carbon rod. The carbon rod disintegrates and is spread over the surface of the object inside the coating chamber. The advantage of carbon coating is that the carbon layer applied is very thin and is reasonably measurable based on the duration of coating application.

Examining the effect of mesh size on mbRSA pose estimation would be a relatively simple experiment in which three or four different RE models of vary mesh sizes (for example; 10,000, 20,000, 50,000, and 100,000 elements) are converted to mbRSA format. These additional models can then be applied to the RSA radiographs already obtained in

this research. The pose estimation error and standard deviation of component pose can be compared between the RE models to determine at what point increased mesh size no longer improves pose estimation.

The effect of inter-component differences, due to manufacturing tolerances, must also be examined. A possible experiment would be to obtain 5 to 10 identical components from the implant manufacturer and perform 3-dimensional scans of each one using the same method of scanning and model reconstruction. Dimensional differences between the components can be analyzed in Geomagic Studio to determine areas of reduced manufacturing tolerance. Additionally, CAD models of the components could be obtained from the manufacturer and compared to the scanned models to examine how closely they match.

In order to improve the condyle-insert contact area, the physiological phantom requires modifications to the size of the femoral component, the location of the pivot point on the femur mount, and anterior tilt of the femoral component on the Sawbones femur. A femoral component which matches the size of the *in vivo* component is crucial for increasing the measured wear area. A centered pivot point and corrected anterior tilt should further improve the condyle-insert contact area and overall wear measurement. Additionally, being able to flex the femur by small increments of 10° or 15° would potentially increase the measured area of the pre-worn inserts.

Additional retrieved polyethylene inserts would further validate the technique of wear measurement developed in this research. Sixteen 11 mm thickness pre-worn inserts have already been designated as possible candidates for wear measurement. Wear meas-

urement on these additional bearings must be performed with the size of femoral component that matches what was implanted in the patient.

The precision of wear measurement must be re-visited to account for differences in RSA and phantom setup between RSA images. The physiological phantom should be reset (unloaded, repositioned, and loaded) between each consecutive RSA image. The developed wear measurement technique should be applied in multiple testing sets on the same insert to determine the repeatability of measurement.

The wear-analysis method developed from this research should also be tested on different TKA types, such as cruciate retaining and mobile bearing designs, in order to determine the robustness of this measurement technique. This technique is likely transferrable to mobile bearing TKA designs however, there is added complexity involved in positioning of the bearing on the tibial tray, as it is not stationary. The author hypothesizes that the lowest point on the articulating surface of the bearing will typically conform to the lowest point of the femoral condyles. From this assumption, the position of the insert can be approximated and the polyethylene wear volume can be estimated.

Finally, this TKA wear measurement technique can be validated *in vivo* by obtaining RSA images of patients whom are scheduled to have their TKA revised in the near future. The optimum imaging procedure, developed and validated via the future research described above, would be applied to each patient. The RSA data can be processed using either manufacturer CAD models of RE models of the TKA components. The volumetric wear can be measured in Geomagic Studio through combination of the RSA image data. Once the patient's TKA is revised and processed through the Implant Retrieval Analysis

Program at the Concordia Hip and Knee Institute, the “known” wear on the polyethylene insert can be compared to the RSA-measured wear.

Bibliography

1. Waddell, J., et al., *Orthopaedic practice in total hip arthroplasty and total knee arthroplasty: results from the Global Orthopaedic Registry (GLORY).* Am J Orthop (Belle Mead NJ). **39**(9 Suppl): p. 5-13.
2. Meunier, A., P. Aspenberg, and L. Good, *Celecoxib does not appear to affect prosthesis fixation in total knee replacement: A randomized study using radiostereometry in 50 patients.* Acta Orthop, 2009. **80**(1): p. 46-50.
3. Manek, N.J., *Medical management of osteoarthritis.* Mayo Clin Proc, 2001. **76**(5): p. 533-9.
4. Ostergaard, M. and P. Halberg, *Intra-articular corticosteroids in arthritic disease: a guide to treatment.* BioDrugs, 1998. **9**(2): p. 95-103.
5. Habib, G.S., *Systemic effects of intra-articular corticosteroids.* Clin Rheumatol, 2009. **28**(7): p. 749-56.
6. A, W.D., O. Robertsson, and L. Lidgren, *Surgery for knee osteoarthritis in younger patients.* Acta Orthop. **81**(2): p. 161-4.
7. Mokdad, A.H., et al., *The continuing epidemics of obesity and diabetes in the United States.* JAMA, 2001. **286**(10): p. 1195-200.
8. Mokdad, A.H., et al., *Prevalence of obesity, diabetes, and obesity-related health risk factors, 2001.* JAMA, 2003. **289**(1): p. 76-9.
9. Gandhi, R., et al., *The relation between body mass index and waist-hip ratio in knee osteoarthritis.* Can J Surg. **53**(3): p. 151-4.
10. Gandhi, R., et al., *BMI independently predicts younger age at hip and knee replacement.* Obesity (Silver Spring). **18**(12): p. 2362-6.
11. Sobieraj, M.C. and C.M. Rimnac, *Ultra high molecular weight polyethylene: mechanics, morphology, and clinical behavior.* J Mech Behav Biomed Mater, 2009. **2**(5): p. 433-43.
12. McClung, C.D., et al., *Relationship between body mass index and activity in hip or knee arthroplasty patients.* J Orthop Res, 2000. **18**(1): p. 35-9.
13. Julin, J., et al., *Younger age increases the risk of early prosthesis failure following primary total knee replacement for osteoarthritis. A follow-up study of 32,019 total knee replacements in the Finnish Arthroplasty Register.* Acta Orthop. **81**(4): p. 413-9.
14. Jacofsky, D.J., *Highly cross-linked polyethylene in total knee arthroplasty: in the affirmative.* J Arthroplasty, 2008. **23**(7 Suppl): p. 28-30.

15. Kurtz, S.M., et al., *Advances in the processing, sterilization, and crosslinking of ultra-high molecular weight polyethylene for total joint arthroplasty.* Biomaterials, 1999. **20**(18): p. 1659-88.
16. Vince, K.G., K. Droll, and D. Chivas, *New concepts in revision total knee arthroplasty.* J Surg Orthop Adv, 2008. **17**(3): p. 165-72.
17. Turgeon, T., E. Bohm, and L. Loucks. *Comparison of registry satisfaction data for primary and revision knee arthroplasty*. in *Canadian Orthopaedic Association*. 2011. St. John's NFLD.
18. Stedman, T.L., *Stedman's Medical Dictionary*. 2010, Franklin Electronic Publishers: Philadelphia.
19. Dorland, W.A.N., *Dorland's Illustrated Medical Dictionary*. 2000, W.B. Saunders.
20. Gray, H., *Anatomy of the Human Body*. 1918, Lea & Febiger: Philadelphia.
21. Kuster, M.S. and G.W. Stachowiak, *Factors affecting polyethylene wear in total knee arthroplasty.* Orthopedics, 2002. **25**(2 Suppl): p. s235-42.
22. Garcia, R.M., et al., *Analysis of retrieved ultra-high-molecular-weight polyethylene tibial components from rotating-platform total knee arthroplasty.* J Arthroplasty, 2009. **24**(1): p. 131-8.
23. Gioe, T.J., et al., *Mobile and fixed-bearing (all-polyethylene tibial component) total knee arthroplasty designs. A prospective randomized trial.* J Bone Joint Surg Am, 2009. **91**(9): p. 2104-12.
24. Hansson, U., et al., *Mobile vs. fixed meniscal bearing in total knee replacement: a randomised radiostereometric study.* Knee, 2005. **12**(6): p. 414-8.
25. Nephew, S., *Genesis II Knee System*, in *Information Brochure*. 2011: Memphis, TN.
26. Reay, E., et al., *Premature failure of Kinemax Plus total knee replacements.* J Bone Joint Surg Br, 2009. **91**(5): p. 604-11.
27. Nieuwenhuijse, M., et al., *Short term excessive migration associated with long term failure of the all-polyethylene acetabular component of the Exeter total hip arthroplasty: 10 to 12 year follow-up.* RSA Conference, 2011. Leiden, The Netherlands(April 6-8, 2011).
28. Vaidya, C., et al., *Reduction of total knee replacement wear with vitamin E blended highly cross-linked ultra-high molecular weight polyethylene.* Proc Inst Mech Eng H, 2011. **225**(1): p. 1-7.
29. Walde, T.A., et al., *Optimized functional femoral rotation in navigated total knee arthroplasty considering ligament tension.* Knee, 2010. **17**(6): p. 381-6.
30. Himanen, A.K., et al., *Survival of the AGC total knee arthroplasty is similar for arthrosis and rheumatoid arthritis. Finnish Arthroplasty Register report on 8,467 operations carried out between 1985 and 1999.* Acta Orthop, 2005. **76**(1): p. 85-8.
31. de Guia, N., et al., *Obesity and joint replacement surgery in Canada: findings from the Canadian Joint Replacement Registry (CJRR).* Healthc Policy, 2006. **1**(3): p. 36-43.
32. Dunbar, M.J., *Cemented femoral fixation: the North Atlantic divide.* Orthopedics, 2009. **32**(9).

33. Fisher, J., et al., *2009 Knee Society Presidential Guest Lecture: Polyethylene wear in total knees.* Clin Orthop Relat Res, 2010. **468**(1): p. 12-8.
34. McEwen, H.M., et al., *The influence of design, materials and kinematics on the in vitro wear of total knee replacements.* J Biomech, 2005. **38**(2): p. 357-65.
35. Charnley, J., *An artificial bearing in the hip joint: implications in biological lubrication.* Fed Proc, 1966. **25**(3): p. 1079-81.
36. Li, S. and A.H. Burstein, *Ultra-high molecular weight polyethylene. The material and its use in total joint implants.* J Bone Joint Surg Am, 1994. **76**(7): p. 1080-90.
37. Jazrawi, L.M., F.J. Kummer, and P.E. DiCesare, *Alternative bearing surfaces for total joint arthroplasty.* J Am Acad Orthop Surg, 1998. **6**(4): p. 198-203.
38. Collier, M.B., et al., *Osteolysis after total knee arthroplasty: influence of tibial baseplate surface finish and sterilization of polyethylene insert. Findings at five to ten years postoperatively.* J Bone Joint Surg Am, 2005. **87**(12): p. 2702-8.
39. Kurtz, S.M., H.A. Gawel, and J.D. Patel, *History and Systematic Review of Wear and Osteolysis Outcomes for First-generation Highly Crosslinked Polyethylene.* Clin Orthop Relat Res.
40. Sibly, T.F. and A. Unsworth, *Wear of cross-linked polyethylene against itself: a material suitable for surface replacement of the finger joint.* J Biomed Eng, 1991. **13**(3): p. 217-20.
41. Utzschneider, S., et al., *Wear of contemporary total knee replacements--a knee simulator study of six current designs.* Clin Biomech (Bristol, Avon), 2009. **24**(7): p. 583-8.
42. Muratoglu, O.K., et al., *Effect of radiation, heat, and aging on in vitro wear resistance of polyethylene.* Clin Orthop Relat Res, 2003(417): p. 253-62.
43. Kurtz, S.M., H.A. Gawel, and J.D. Patel, *History and Systematic Review of Wear and Osteolysis Outcomes for First-generation Highly Crosslinked Polyethylene.* Clin Orthop Relat Res, 2011.
44. Micheli, B.R., et al., *Knee Simulator Wear of Vitamin E Stabilized Irradiated Ultrahigh Molecular Weight Polyethylene.* J Arthroplasty, 2011.
45. Tsukamoto, R., et al., *Wear of sequentially enhanced 9-Mrad polyethylene in 10 million cycle knee simulation study.* J Biomed Mater Res B Appl Biomater, 2008. **86**(1): p. 119-24.
46. Dumbleton, J.H., et al., *The basis for a second-generation highly cross-linked UHMWPE.* Clin Orthop Relat Res, 2006. **453**: p. 265-71.
47. Campbell, D.G., J.R. Field, and S.A. Callary, *Second-generation highly cross-linked X3 polyethylene wear: a preliminary radiostereometric analysis study.* Clin Orthop Relat Res. **468**(10): p. 2704-9.
48. Bragdon, C.R., et al., *Radiostereometric analysis comparison of wear of highly cross-linked polyethylene against 36- vs 28-mm femoral heads.* J Arthroplasty, 2007. **22**(6 Suppl 2): p. 125-9.
49. Gill, H.S., et al., *In vivo measurement of volumetric wear of a total knee replacement.* Knee, 2006. **13**(4): p. 312-7.
50. Ranawat, A.S., et al., *Experience with an all-polyethylene total knee arthroplasty in younger, active patients with follow-up from 2 to 11 years.* J Arthroplasty, 2005. **20**(7 Suppl 3): p. 7-11.

51. Cheung, E.V., J.W. Sperling, and R.H. Cofield, *Polyethylene insert exchange for wear after total shoulder arthroplasty.* J Shoulder Elbow Surg, 2007. **16**(5): p. 574-8.
52. ElMaraghy, A. and M. Devereaux, *Medial wear of the polyethylene component associated with heterotopic ossification after reverse shoulder arthroplasty.* Can J Surg, 2008. **51**(5): p. E103-4.
53. Bell, C.J. and J. Fisher, *Simulation of polyethylene wear in ankle joint prostheses.* J Biomed Mater Res B Appl Biomater, 2007. **81**(1): p. 162-7.
54. Glazebrook, M., et al., *Longitudinal migration and inducible displacement of a mobile bearing total ankle arthoplasty system.* RSA Conference, 2011. Leiden, The Netherlands(April 6-8, 2011).
55. Cinotti, G., T. David, and F. Postacchini, *Results of disc prosthesis after a minimum follow-up period of 2 years.* Spine (Phila Pa 1976), 1996. **21**(8): p. 995-1000.
56. Campbell, P., F.W. Shen, and H. McKellop, *Biologic and tribologic considerations of alternative bearing surfaces.* Clin Orthop Relat Res, 2004(418): p. 98-111.
57. Collier, M.B., et al., *Radiographic assessment of the thickness lost from polyethylene tibial inserts that had been sterilized differently.* J Bone Joint Surg Am, 2008. **90**(7): p. 1543-52.
58. Muratoglu, O.K., et al., *Metrology to quantify wear and creep of polyethylene tibial knee inserts.* Clin Orthop Relat Res, 2003(410): p. 155-64.
59. Glyn-Jones, S., et al., *The creep and wear of highly cross-linked polyethylene: a three-year randomised, controlled trial using radiostereometric analysis.* J Bone Joint Surg Br, 2008. **90**(5): p. 556-61.
60. Engh, G.A., et al., *Analysis of wear in retrieved mobile and fixed bearing knee inserts.* J Arthroplasty, 2009. **24**(6 Suppl): p. 28-32.
61. Collier, M.B., et al., *Factors associated with the loss of thickness of polyethylene tibial bearings after knee arthroplasty.* J Bone Joint Surg Am, 2007. **89**(6): p. 1306-14.
62. Popoola, O.O., et al., *Wear, delamination, and fatigue resistance of melt-annealed highly crosslinked UHMWPE cruciate-retaining knee inserts under activities of daily living.* J Orthop Res, 2010. **28**(9): p. 1120-6.
63. D'Antonio, J.A., et al., *Five-year experience with Crossfire highly cross-linked polyethylene.* Clin Orthop Relat Res, 2005. **441**: p. 143-50.
64. Glyn-Jones, S., et al., *Does highly cross-linked polyethylene wear less than conventional polyethylene in total hip arthroplasty? A double-blind, randomized, and controlled trial using roentgen stereophotogrammetric analysis.* J Arthroplasty, 2008. **23**(3): p. 337-43.
65. Rohrl, S., et al., *In vivo wear and migration of highly cross-linked polyethylene cups a radiostereometry analysis study.* J Arthroplasty, 2005. **20**(4): p. 409-13.
66. Manning, D.W., et al., *In vivo comparative wear study of traditional and highly cross-linked polyethylene in total hip arthroplasty.* J Arthroplasty, 2005. **20**(7): p. 880-6.
67. Borlin, N. *Radiostereometric Analysis (RSA).* 2000 [cited 2011 03/08/2011].

68. Selvik, G., P. Alberius, and A.S. Aronson, *A roentgen stereophotogrammetric system. Construction, calibration and technical accuracy.* Acta Radiol Diagn (Stockh), 1983. **24**(4): p. 343-52.
69. Karrholm, J., R.H. Gill, and E.R. Valstar, *The history and future of radiostereometric analysis.* Clin Orthop Relat Res, 2006. **448**: p. 10-21.
70. Selvik, G., P. Alberius, and M. Fahlman, *Roentgen stereophotogrammetry for analysis of cranial growth.* Am J Orthod, 1986. **89**(4): p. 315-25.
71. Baldursson, H., et al., *Instability and wear of total hip prostheses determined with roentgen stereophotogrammetry.* Arch Orthop Trauma Surg, 1979. **95**(4): p. 257-63.
72. Selvik, G., *Roentgen stereophotogrammetric analysis.* Acta Radiol, 1990. **31**(2): p. 113-26.
73. Ryd, L., et al., *Roentgen stereophotogrammetric analysis as a predictor of mechanical loosening of knee prostheses.* J Bone Joint Surg Br, 1995. **77**(3): p. 377-83.
74. Karrholm, J., et al., *Does early micromotion of femoral stem prostheses matter? 4-7-year stereoradiographic follow-up of 84 cemented prostheses.* J Bone Joint Surg Br, 1994. **76**(6): p. 912-7.
75. Hauptfleisch, J., et al., *The premature failure of the Charnley Elite-Plus stem: a confirmation of RSA predictions.* J Bone Joint Surg Br, 2006. **88**(2): p. 179-83.
76. Alfaro-Adrian, J., H.S. Gill, and D.W. Murray, *Should total hip arthroplasty femoral components be designed to subside? A radiostereometric analysis study of the Charnley Elite and Exeter stems.* J Arthroplasty, 2001. **16**(5): p. 598-606.
77. Gill, H.S., et al., *The effect of anteversion on femoral component stability assessed by radiostereometric analysis.* J Arthroplasty, 2002. **17**(8): p. 997-1005.
78. Valstar, E.R., et al., *Model-based Roentgen stereophotogrammetry of orthopaedic implants.* J Biomech, 2001. **34**(6): p. 715-22.
79. Kaptein, B.L., et al., *A new model-based RSA method validated using CAD models and models from reversed engineering.* J Biomech, 2003. **36**(6): p. 873-82.
80. Stefansdottir, A., et al., *Movement pattern of the Exeter femoral stem; a radiostereometric analysis of 22 primary hip arthroplasties followed for 5 years.* Acta Orthop Scand, 2004. **75**(4): p. 408-14.
81. Ryd, L., et al., *Tibial component fixation in knee arthroplasty.* Clin Orthop Relat Res, 1986(213): p. 141-9.
82. Bey, M.J., et al., *Accuracy of biplane x-ray imaging combined with model-based tracking for measuring in-vivo patellofemoral joint motion.* J Orthop Surg Res, 2008. **3**: p. 38.
83. Aronson, A.S., N. Jonsson, and P. Alberius, *Tantalum markers in radiography. An assessment of tissue reactions.* Skeletal Radiol, 1985. **14**(3): p. 207-11.
84. Valstar, E.R., et al., *Guidelines for standardization of radiostereometry (RSA) of implants.* Acta Orthop, 2005. **76**(4): p. 563-72.
85. Ryd, L., X. Yuan, and H. Lofgren, *Methods for determining the accuracy of radiostereometric analysis (RSA).* Acta Orthop Scand, 2000. **71**(4): p. 403-8.

86. Biomedical, R., *Instructional RSA - User Course*, in *RSA Biomedical*. 2005: Goteborg, Sweden.
87. Gascoyne, T., et al. *Precision comparison between CR and DR x-ray system for radiostereometric analysis (RSA).* in *Canadian Orthopaedic Association*. 2011. St. John's, NFLD.
88. Nystrom, L., I. Soderkvist, and P.A. Wedin, *A note on some identification problems arising in roentgen stereo photogrammetric analysis.* J Biomech, 1994. **27**(10): p. 1291-4.
89. Makinen, T.J., et al., *Comparison of digital and conventional radiostereometric image analysis in an ankle phantom model.* Scand J Surg, 2005. **94**(3): p. 233-8.
90. Kaptein, B.L., et al., *Clinical validation of model-based RSA for a total knee prosthesis.* Clin Orthop Relat Res, 2007. **464**: p. 205-9.
91. Baad-Hansen, T., et al., *High-precision measurements of cementless acetabular components using model-based RSA: an experimental study.* Acta Orthop, 2007. **78**(4): p. 463-9.
92. Hurschler, C., et al., *Accuracy of model-based RSA contour reduction in a typical clinical application.* Clin Orthop Relat Res, 2008. **466**(8): p. 1978-86.
93. Seehaus, F., et al., *Experimental analysis of Model-Based Roentgen Stereophotogrammetric Analysis (MBRSA) on four typical prosthesis components.* J Biomech Eng, 2009. **131**(4): p. 041004.
94. Ranstam, J., L. Ryd, and I. Onsten, *Accurate accuracy assessment - Review of basic principles.* Acta Orthop Scand, 2000. **71**(1): p. 106-108.
95. Bragdon, C.R., et al., *Experimental assessment of precision and accuracy of radiostereometric analysis for the determination of polyethylene wear in a total hip replacement model.* J Orthop Res, 2002. **20**(4): p. 688-95.
96. Laende, E.K., et al., *Implementation and validation of an implant-based coordinate system for RSA migration calculation.* J Biomech, 2009. **42**(14): p. 2387-93.
97. Dym, C.L. and L. Patrick, *Engineering Design: A Project-Based Introduction*. Third ed. 2009, Hoboken, NJ: John Wiley & Sons.
98. D'Lima, D.D., et al., *Tibial forces measured in vivo after total knee arthroplasty.* J Arthroplasty, 2006. **21**(2): p. 255-62.
99. D'Lima, D.D., et al., *In vivo contact stresses during activities of daily living after knee arthroplasty.* J Orthop Res, 2008. **26**(12): p. 1549-55.
100. Ryd, L., *Roentgen stereophotogrammetric analysis of prosthetic fixation in the hip and knee joint.* Clin Orthop Relat Res, 1992(276): p. 56-65.
101. Alfaro-Adrian, J., et al., *Mid-term migration of a cemented total hip replacement assessed by radiostereometric analysis.* Int Orthop, 1999. **23**(3): p. 140-4.
102. Karrholm, J., et al., *Radiostereometry of hip prostheses. Review of methodology and clinical results.* Clin Orthop Relat Res, 1997(344): p. 94-110.
103. Madanat, R., et al., *Accuracy and precision of radiostereometric analysis in the measurement of three-dimensional micromotion in a fracture model of the distal radius.* J Orthop Res, 2005. **23**(2): p. 481-8.
104. Trozzi, C., et al., *Precision assessment of model-based RSA for a total knee prosthesis in a biplanar set-up.* Knee, 2008. **15**(5): p. 396-402.

105. Onsten, I., et al., *Accuracy and precision of radiostereometric analysis in the measurement of THR femoral component translations: human and canine in vitro models.* J Orthop Res, 2001. **19**(6): p. 1162-7.
106. Kaptein, B.L., et al., *Evaluation of three pose estimation algorithms for model-based roentgen stereophotogrammetric analysis.* Proc Inst Mech Eng H, 2004. **218**(4): p. 231-8.
107. Teeter, M.G., et al. *How do CAD models compare to reverse engineered polyethylene components for use in wear analysis?* in *RSA Conference*. 2011. Leiden, The Netherlands.
108. Hurschler, C., et al., *Comparison of the model-based and marker-based roentgen stereophotogrammetry methods in a typical clinical setting.* J Arthroplasty, 2009. **24**(4): p. 594-606.
109. Campbell, D.G., J.R. Field, and S.A. Callary, *Second-generation highly cross-linked X3 polyethylene wear: a preliminary radiostereometric analysis study.* Clin Orthop Relat Res, 2010. **468**(10): p. 2704-9.
110. Montgomery, D.C., *Design and Analysis of Experiments*. Vol. Third. 1991, New York: John Wiley & Sons.
111. McDonald, J.H., *Handbook of Biological Statistics*. 2009, Sparky House Publishing: Baltimore, Maryland.
112. Levangie, P. and C. Norkin, *Joint Structure and Function - A Comprehensive Analysis*. Fifth ed. 2011, Philadelphia, PA: Davis Company.
113. Digas, G., et al., *5-year experience of highly cross-linked polyethylene in cemented and uncemented sockets: two randomized studies using radiostereometric analysis.* Acta Orthop, 2007. **78**(6): p. 746-54.
114. Nakahara, I., et al., *Minimum five-year follow-up wear measurement of longevity highly cross-linked polyethylene cup against cobalt-chromium or zirconia heads.* J Arthroplasty, 2010. **25**(8): p. 1182-7.
115. D'Lima, D.D., P.C. Chen, and C.W. Colwell, Jr., *Polyethylene contact stresses, articular congruity, and knee alignment.* Clin Orthop Relat Res, 2001(392): p. 232-8.
116. Cottrell, J.M., et al., *Stair ascent kinematics affect UHMWPE wear and damage in total knee replacements.* J Biomed Mater Res B Appl Biomater, 2006. **78**(1): p. 15-9.
117. Callaghan, J.J., R. O'Rourke M, and K.J. Saleh, *Why knees fail: lessons learned.* J Arthroplasty, 2004. **19**(4 Suppl 1): p. 31-4.
118. Mulhall, K.J., et al., *Current etiologies and modes of failure in total knee arthroplasty revision.* Clin Orthop Relat Res, 2006. **446**: p. 45-50.
119. Vessely, M.B., et al., *The Chitranjan Ranawat Award: Long-term survivorship and failure modes of 1000 cemented condylar total knee arthroplasties.* Clin Orthop Relat Res, 2006. **452**: p. 28-34.
120. Carr, A.J., et al., *Knee replacement.* Lancet, 2012. **379**(9823): p. 1331-40.
121. Muratoglu, O.K., et al., *Knee-simulator testing of conventional and cross-linked polyethylene tibial inserts.* J Arthroplasty, 2004. **19**(7): p. 887-97.
122. Lachiewicz, P.F. and M.R. Geyer, *The use of highly cross-linked polyethylene in total knee arthroplasty.* J Am Acad Orthop Surg, 2011. **19**(3): p. 143-51.

123. Fisher, J., et al., *Wear, debris, and biologic activity of cross-linked polyethylene in the knee: benefits and potential concerns.* Clin Orthop Relat Res, 2004(428): p. 114-9.
124. Ries, M.D., *Highly cross-linked polyethylene: the debate is over--in opposition.* J Arthroplasty, 2005. **20**(4 Suppl 2): p. 59-62.
125. Wall, B.F. and D. Hart, *Revised radiation doses for typical X-ray examinations. Report on a recent review of doses to patients from medical X-ray examinations in the UK by NRPB. National Radiological Protection Board.* Br J Radiol, 1997. **70**(833): p. 437-9.
126. Kellett, C.F., et al., *In vivo measurement of total knee replacement wear.* Knee, 2004. **11**(3): p. 183-7.
127. Simpson, D.J., et al., *Development of a model-based Roentgen stereophotogrammetric analysis system to measure polyethylene wear in unicompartmental arthroplasty.* Proc Inst Mech Eng H. **224**(11): p. 1235-43.
128. Altan, E., *Phantom Study - Polyethylene wear in a total knee arthroplasty*. 2009, Dalhousie University, Biomedical Engineering and QEII Health Sciences Centre: Halifax, NS.
129. Cai, R., et al., *Development of an RSA calibration system with improved accuracy and precision.* J Biomech, 2008. **41**(4): p. 907-11.
130. Makinen, T.J., et al., *Precision measurements of the RSA method using a phantom model of hip prosthesis.* J Biomech, 2004. **37**(4): p. 487-93.
131. van Ijsseldijk, E.A., et al., *The robustness and accuracy of in vivo linear wear measurements for knee prostheses based on model-based RSA.* J Biomech, 2011. **44**(15): p. 2724-7.
132. Kadaba, M.P., H.K. Ramakrishnan, and M.E. Wootten, *Measurement of lower extremity kinematics during level walking.* J Orthop Res, 1990. **8**(3): p. 383-92.
133. Technology, N.I.o.S.a., *Engineering Statistics Handbook*, NIST/SEMATECH, Editor. 2012, U.S. Commerce Department of Technology Administration.

Appendices

7.1 Appendix A

The Anderson-Darling (AD) test is a statistical test used to determine if a sample of data originates from a population with a specific distribution, such as normal, lognormal, exponential, etc. It is a modification on the simpler Kolmogorov-Smirnov (KS) test, in that the AD test applies more weight to the tails of the sample distribution than the KS test, and is therefore a generally more sensitive distribution test [133]. The AD test statistic is defined as;

$$A^2 = -N - S$$

Where;

$$S = \sum_{i=1}^{N} \frac{2(i-1)}{N} \left[lnF(Y_i) + \ln\left(1 - F(Y_{N+1-i})\right) \right]$$

Where F is the cumulative distribution function of the specified distribution (bell-curve equation for a normal distribution) and Y_i are the data in order (smallest to largest) [133].

The prediction interval of the response value (Y value) at a specific input value (X value) is defined by the equation [133]:

$$\hat{y} \pm t_{1-\frac{\alpha}{2},v} \sqrt{\hat{\sigma}^2 + \hat{\sigma}_f^2}$$

Where $\hat{\sigma}^2$ is the residual standard deviation obtained when fitting the regression model to the data, $\hat{\sigma}_f^2$ is the standard deviation of the predicted $\hat{y}$ values of the regression model, $t_{1-\frac{\alpha}{2},v}$ is the Student's t value coverage factor with user-specified significance level $(1-\alpha)/2$ and degrees of freedom v [133].

An analysis of variance (ANOVA) is used to determine if a statistically significant difference exists between three or more groups while removing the effect of a covariate. For this research, the analyses of variance were used to remove the effect of either imaging orientation or knee flexion as part of a factorial experiment. Below is an example of a typical ANOVA table.

Yt Metric	Sum of Squares	Degrees of Freedom	Mean Square	Computed F ratio	Critical F value	P value
Orientation	9027.1	3	3009.0	6.16	2.7	Sig
Flexion	41370.8	2	20685.4	42.32	3.1	Sig
Interaction	78067.0	6	1301.2	2.66	2.2	Sig
Error	46925.6	96	488.8			
Total	105130.4	107				

Where the sum of squares is computed as the sum of the squared differences between each data point (x_i) and the mean of the dataset ($\overline{x}$). The degrees of freedom (DOF) for each factor is the number of levels of each factor – 1. DOF for interaction is the DOF of factor A * the DOF of factor B. The total DOF is the number of levels of factor A * number of levels of factor B * the number of replicates per group. Mean square is calculated as the sum of squares / the DOF. The F ratio is computed by dividing each mean square by the mean square of the error. The critical F values are obtained from a table of values and are specified by the DOF of the factor (numerator), DOF of the error term (denominator), and the selected level of significance (alpha). If the F ratio is greater than the critical F value, at least one statistically significant difference exists within the comparison group.

7.2 Appendix B

Tables B1 through B7 are summaries of the precision (standard deviation of error) of the mbRSA system using four different image comparison techniques; all-pairs, reference, random-reference, independent pairs (as described in Section 3.4.3 of this thesis), for both the original and revised TKA component models.

Table B1: Precision (standard deviation) for all axes of motion, all pairs comparison data, original models.

Knee Flexion	Imaging Orientation	Xt (mm)	Yt (mm)	Zt (mm)	Xr (°)	Yr (°)	Zr (°)	MTPM t (mm)	MTPM r (°)
Standing	AP	0.02008	0.02096	0.04875	0.07251	0.17332	0.06057	0.02658	0.08281
	30° offset	0.04781	0.01889	0.11357	0.11921	0.38230	0.09294	0.07755	0.24678
	60° offset	0.03221	0.02197	0.12465	0.09403	0.19583	0.02068	0.09655	0.10398
	ML	0.01122	0.01555	0.03888	0.06187	0.15647	0.06884	0.02269	0.10599
45° Flexed	AP	0.01796	0.02698	0.04710	0.03497	0.17579	0.05198	0.02198	0.09712
	30° offset	0.06029	0.02959	0.10718	0.09015	0.22298	0.04704	0.06903	0.13160
	60° offset	0.05998	0.02635	0.12403	0.11025	0.17078	0.09115	0.08403	0.10327
	ML	0.04226	0.01644	0.03889	0.05014	0.11775	0.04724	0.02503	0.05914
Sitting	AP	0.01914	0.01333	0.01237	0.07749	0.15265	0.03669	0.01044	0.07409
	30° offset	0.05407	0.02551	0.08598	0.10539	0.24875	0.04400	0.07240	0.13149
	60° offset	0.03140	0.01867	0.03782	0.03032	0.23785	0.04514	0.02150	0.14778
	ML	0.02353	0.01251	0.03414	0.02927	0.14223	0.03257	0.01717	0.07833

Table B2: Precision (standard deviation) for all axes of motion, all pairs comparison data, revised models.

Knee Flexion	Imaging Orientation	Xt (mm)	Yt (mm)	Zt (mm)	Xr (°)	Yr (°)	Zr (°)	MTPM t (mm)	MTPM r (°)
Standing	AP	0.03064	0.02430	0.05234	0.13042	0.23703	0.06495	0.03122	0.13668
	30° offset	0.09836	0.02754	0.08553	0.13927	0.55075	0.10548	0.06525	0.33947
	60° offset	0.02848	0.04065	0.15940	0.10474	0.20402	0.03019	0.13224	0.11619
	ML	0.05165	0.01563	0.11123	0.09509	0.17646	0.07620	0.08051	0.10376
45° Flexed	AP	0.04120	0.02470	0.07025	0.06091	0.26522	0.04836	0.03686	0.14888
	30° offset	0.05235	0.03091	0.08501	0.07676	0.24208	0.04241	0.04264	0.17886
	60° offset	0.04988	0.05028	0.16467	0.12473	0.16108	0.07950	0.14739	0.11467
	ML	0.04236	0.01803	0.05542	0.05790	0.11720	0.03801	0.03882	0.07201
Sitting	AP	0.03179	0.01735	0.08689	0.11461	0.21458	0.05314	0.06321	0.11808
	30° offset	0.05953	0.04067	0.08780	0.14975	0.30009	0.04332	0.06217	0.17182

	60° offset	0.04712	0.05879	0.14190	0.11245	0.20490	0.07011	0.12364	0.11352
	ML	0.03149	0.01398	0.09155	0.04443	0.26726	0.04825	0.06988	0.16539

Table B 3: Precision (standard deviation) for all axes of motion, reference data, revised models.

Knee Flexion	Imaging Orientation	Xt (mm)	Yt (mm)	Zt (mm)	Xr (°)	Yr (°)	Zr (°)	MTPM t (mm)	MTPM r (°)
Standing	AP	0.02737	0.02106	0.02823	0.03527	0.16996	0.05193	0.02588	0.05811
	30° offset	0.07493	0.02185	0.06677	0.11103	0.41527	0.08160	0.04830	0.26535
	60° offset	0.02922	0.03584	0.16279	0.07718	0.15906	0.02108	0.16136	0.14792
	ML	0.03883	0.01219	0.10696	0.09022	0.12698	0.06086	0.06224	0.09479
45° Flexed	AP	0.02603	0.01696	0.05088	0.04179	0.20460	0.03427	0.03271	0.13496
	30° offset	0.03688	0.02851	0.06257	0.05717	0.19921	0.04027	0.04670	0.19833
	60° offset	0.03169	0.05120	0.18904	0.10607	0.13487	0.06679	0.17645	0.14231
	ML	0.04006	0.01533	0.04424	0.05126	0.09691	0.02998	0.04456	0.04264
Sitting	AP	0.03149	0.01586	0.08398	0.09319	0.15785	0.04245	0.07052	0.11985
	30° offset	0.03687	0.03905	0.07290	0.09447	0.19817	0.03703	0.05453	0.18598
	60° offset	0.04681	0.05182	0.13265	0.09995	0.15215	0.05461	0.12100	0.08427
	ML	0.02855	0.01047	0.09567	0.04552	0.20095	0.03741	0.08085	0.20126

Table B4: Precision (standard deviation) for all axes of motion, random-reference data, original models.

Knee Flexion	Imaging Orientation	Xt (mm)	Yt (mm)	Zt (mm)	Xr (°)	Yr (°)	Zr (°)	MTPM t (mm)	MTPM r (°)
Standing	AP	0.02013	0.01494	0.03720	0.05437	0.13148	0.04233	0.02641	0.07400
	30° offset	0.03471	0.01518	0.08465	0.09351	0.27112	0.06849	0.06590	0.26798
	60° offset	0.03269	0.01620	0.12166	0.08834	0.12769	0.01553	0.11152	0.12965
	ML	0.01090	0.00996	0.03026	0.05164	0.13135	0.05410	0.02371	0.09206
45° Flexed	AP	0.01326	0.01861	0.03476	0.02889	0.13262	0.03116	0.01275	0.06918
	30° offset	0.05140	0.03406	0.08130	0.06591	0.18678	0.04759	0.05545	0.06288
	60° offset	0.04131	0.02719	0.11955	0.08505	0.13011	0.06326	0.08906	0.08833
	ML	0.03326	0.01602	0.03094	0.04561	0.08176	0.03139	0.02016	0.06921
Sitting	AP	0.01402	0.01002	0.01086	0.06345	0.09798	0.02915	0.01054	0.08025
	30° offset	0.03681	0.02692	0.09193	0.07623	0.17155	0.03692	0.05653	0.14551
	60° offset	0.03073	0.01391	0.02664	0.02305	0.17660	0.03268	0.02015	0.07489
	ML	0.01761	0.00929	0.02472	0.02382	0.11545	0.02630	0.01603	0.06897

Table B5: Precision (standard deviation) for all axes of motion, random-reference data, revised models.

Knee Flexion	Imaging Orientation	Xt (mm)	Yt (mm)	Zt (mm)	Xr (°)	Yr (°)	Zr (°)	MTPM t (mm)	MTPM r (°)
Standing	AP	0.02851	0.02070	0.03923	0.11160	0.17536	0.04972	0.02450	0.12196
	30° offset	0.07109	0.02141	0.06674	0.11044	0.39912	0.07815	0.06884	0.28418
	60° offset	0.02845	0.03542	0.16506	0.07681	0.15686	0.02194	0.16018	0.15127
	ML	0.03846	0.01217	0.10695	0.08626	0.13030	0.06110	0.04382	0.09614
45° Flexed	AP	0.02603	0.01696	0.05088	0.04179	0.20460	0.03427	0.03271	0.13496
	30° offset	0.04356	0.03356	0.05655	0.05403	0.23627	0.04647	0.05012	0.19022
	60° offset	0.03701	0.05547	0.19473	0.11385	0.15103	0.06096	0.16092	0.11080
	ML	0.04194	0.01651	0.05017	0.05403	0.09289	0.02970	0.02483	0.07691
Sitting	AP	0.03338	0.01596	0.08972	0.10331	0.10542	0.03623	0.04990	0.11443
	30° offset	0.04094	0.03763	0.08654	0.10492	0.22097	0.04392	0.05310	0.16006
	60° offset	0.04694	0.05165	0.13450	0.10079	0.13905	0.05626	0.10349	0.07829
	ML	0.02848	0.01068	0.10137	0.04608	0.22588	0.03428	0.03760	0.12376

Table B6: Precision (standard deviation) for all axes of motion, independent pairs data, original models.

Knee Flexion	Imaging Orientation	Xt (mm)	Yt (mm)	Zt (mm)	Xr (°)	Yr (°)	Zr (°)	MTPM t (mm)	MTPM r (°)
Standing	AP	0.02237	0.01008	0.06423	0.08154	0.16023	0.03834	0.03622	0.08941
	30° offset	0.05188	0.02078	0.11752	0.12477	0.49128	0.12321	0.08538	0.35377
	60° offset	0.02196	0.02380	0.11000	0.10867	0.24430	0.02341	0.06458	0.12445
	ML	0.00970	0.01700	0.02970	0.03208	0.12417	0.07558	0.01287	0.06855
45° Flexed	AP	0.02011	0.03030	0.03604	0.02161	0.17065	0.05662	0.01908	0.06397
	30° offset	0.04361	0.02398	0.12649	0.07946	0.22447	0.05035	0.07030	0.11390
	60° offset	0.07713	0.01628	0.07261	0.07954	0.19819	0.09365	0.03264	0.09067
	ML	0.03214	0.00593	0.01994	0.04343	0.06704	0.02442	0.02495	0.03602
Sitting	AP	0.02080	0.01082	0.01356	0.04525	0.18161	0.03897	0.00836	0.08066
	30° offset	0.01395	0.01594	0.08228	0.07451	0.15778	0.04019	0.06888	0.08667
	60° offset	0.02368	0.01084	0.03264	0.04260	0.31947	0.05872	0.03050	0.21023
	ML	0.01910	0.00769	0.03898	0.03008	0.16676	0.01558	0.01258	0.04304

Table B7: Precision (standard deviation) for all axes of motion, independent pairs data, revised models.

Knee Flexion	Imaging Orientation	Xt (mm)	Yt (mm)	Zt (mm)	Xr (°)	Yr (°)	Zr (°)	MTPM t (mm)	MTPM r (°)
Standing	AP	0.03398	0.01426	0.07526	0.15031	0.21817	0.06779	0.04048	0.10046
	30° offset	0.12159	0.03372	0.05276	0.16611	0.69929	0.14049	0.08314	0.45687
	60° offset	0.02170	0.02770	0.09221	0.13277	0.17087	0.03048	0.06499	0.10111
	ML	0.05241	0.01336	0.05420	0.04557	0.22539	0.08715	0.04933	0.12078
45° Flexed	AP	0.05619	0.02471	0.02145	0.04457	0.27570	0.05500	0.02891	0.16908
	30° offset	0.03924	0.01662	0.05781	0.04440	0.21904	0.03502	0.03593	0.17079
	60° offset	0.04419	0.04040	0.09948	0.11246	0.18314	0.05600	0.07514	0.09232
	ML	0.03378	0.00575	0.04623	0.05265	0.09343	0.03088	0.02587	0.06650
Sitting	AP	0.02638	0.01599	0.04383	0.06929	0.19316	0.05037	0.03772	0.09662
	30° offset	0.03660	0.02375	0.07511	0.09209	0.28726	0.03186	0.04606	0.15883
	60° offset	0.05694	0.01517	0.06320	0.05261	0.24470	0.08093	0.04398	0.17360
	ML	0.02381	0.00595	0.07774	0.03062	0.26741	0.04439	0.04127	0.15641

7.3 Appendix C

Table C1 is a summary of the results of the Anderson-Darling test for normal distribution for all image comparison methods, for both model types, and each sub-group of data. Statistical significance (bolded) indicates a non-normal distribution. The all-pairs data sub-groups consist of 45 samples (n=45), the reference and random-reference data sub-groups consist of 9 samples (n=9), and the independent pairs data sub-groups consist of 5 samples (n=5). The "All" groups (top row of each section) consist of 540 samples (all-pairs), 108 samples (reference and random-reference), and 60 samples (independent pairs).

Table C1: P values from Anderson-Darling normality test. P<0.05 indicates non-normal distribution.

			Original Models				Revised Models			
Dataset	Orientation	Flexion	Yt	Abs Yt	MTPM (t)	MTPM (r)	Yt	Abs Yt	MTPM (t)	MTPM (r)
All Pairs Data	All	All	**0.005**	**0.005**	**0.005**	**0.005**	**0.005**	**0.005**	**0.005**	**0.005**
	AP	Standing	**0.042**	**0.017**	0.241	0.1	**0.015**	**0.005**	0.328	0.111
	AP	45° Flex	0.93	0.156	0.563	**0.005**	0.547	0.165	0.445	**0.021**
	AP	Sitting	0.987	**0.005**	0.512	0.28	0.622	0.267	0.118	**0.014**
	30° offset	Standing	**0.005**	**0.005**	**0.005**	**0.005**	0.219	**0.005**	**0.009**	**0.026**
	30° offset	45° Flex	**0.005**	**0.005**	**0.04**	0.204	0.212	**0.012**	0.258	**0.005**
	30° offset	Sitting	0.283	0.104	**0.006**	**0.045**	0.746	0.109	**0.044**	0.167
	60° offset	Standing	0.973	**0.005**	0.077	0.187	0.118	0.077	**0.005**	0.097
	60° offset	45° Flex	0.243	**0.008**	0.159	0.186	**0.005**	**0.005**	0.073	0.234
	60° offset	Sitting	0.292	0.173	0.731	**0.005**	**0.005**	**0.005**	**0.005**	0.445
	ML	Standing	0.624	0.055	**0.005**	**0.005**	0.63	**0.005**	0.156	**0.006**
	ML	45° Flex	0.862	0.061	0.244	0.339	0.824	0.276	0.578	0.106
	ML	Sitting	0.266	**0.008**	0.566	0.107	**0.014**	**0.03**	**0.048**	**0.033**
Total	**55 of 104 normally distributed**									

Dataset	Orientation	Flexion	Original Models				Revised Models			
			Yt	Abs Yt	MTPM (t)	MTPM (r)	Yt	Abs Yt	MTPM (t)	MTPM (r)
Reference Data	All	All	**0.005**	**0.005**	**0.005**	**0.005**	**0.005**	**0.005**	**0.005**	**0.005**
	AP	Standing	0.263	**0.038**	0.246	0.94	**0.05**	**0.037**	**0.023**	0.169
	AP	45° Flex	0.925	0.925	0.652	0.159	0.771	0.643	0.934	**0.036**
	AP	Sitting	0.356	0.111	0.593	0.094	0.831	0.797	0.836	0.466
	30° offset	Standing	**0.006**	**0.005**	**0.025**	**0.026**	0.141	**0.028**	0.219	0.102
	30° offset	45° Flex	0.161	0.161	**0.01**	**0.04**	0.145	0.145	0.872	0.089
	30° offset	Sitting	0.394	0.45	0.113	0.409	0.695	0.151	**0.005**	0.544
	60° offset	Standing	0.228	0.228	0.328	0.91	0.52	0.568	0.11	0.221
	60° offset	45° Flex	0.326	0.119	0.329	0.387	**0.011**	**0.011**	0.287	0.327
	60° offset	Sitting	0.463	0.254	0.682	0.064	**0.005**	**0.005**	**0.005**	0.736
	ML	Standing	0.826	0.424	**0.022**	**0.04**	0.534	**0.037**	0.237	**0.041**
	ML	45° Flex	0.549	0.267	0.425	0.429	0.859	0.533	0.335	0.497
	ML	Sitting	0.26	0.077	0.18	0.1	0.483	**0.016**	0.315	0.154
Total	**73 of 104 normally distributed**									
Random Reference Data	All	All	**0.005**	**0.005**	**0.005**	**0.005**	**0.005**	**0.005**	**0.005**	**0.005**
	AP	Standing	0.184	**0.011**	0.509	0.574	0.091	**0.005**	0.621	0.118
	AP	45° Flex	0.925	0.925	0.652	0.159	0.771	0.643	0.934	**0.031**
	AP	Sitting	0.556	0.084	0.509	0.371	0.635	0.473	0.197	0.681
	30° offset	Standing	**0.006**	**0.005**	**0.028**	0.376	0.084	**0.005**	0.171	**0.047**
	30° offset	45° Flex	0.199	0.091	0.85	0.214	0.551	0.075	0.257	**0.0285**
	30° offset	Sitting	0.503	0.44	0.604	0.59	0.818	0.241	0.896	0.589
	60° offset	Standing	0.338	0.127	0.395	0.676	0.492	0.492	0.091	0.29
	60° offset	45° Flex	0.181	0.181	0.104	0.894	0.061	**0.008**	0.075	0.897
	60° offset	Sitting	0.556	0.514	0.957	0.103	**0.005**	**0.005**	**0.011**	0.33
	ML	Standing	0.74	0.74	0.083	0.103	0.565	**0.026**	0.377	0.173
	ML	45° Flex	0.939	0.331	0.222	0.754	0.844	0.884	0.797	0.53
	ML	Sitting	0.205	0.188	0.664	0.828	0.403	0.877	0.46	0.262
Total	**82 of 104 normally distributed**									
Independent Pairs Data	All	All	0.138	**0.005**	**0.005**	**0.005**	0.053	**0.005**	**0.005**	**0.005**
	AP	Standing	0.814	0.532	0.620	0.665	0.699	0.576	0.583	0.912
	AP	45° Flex	0.619	0.476	0.424	0.535	0.464	0.118	0.389	**0.010**
	AP	Sitting	0.530	0.516	0.144	0.552	0.406	0.153	0.125	0.559
	30° offset	Standing	**0.012**	**0.005**	0.425	0.269	0.346	0.182	0.061	0.415
	30° offset	45° Flex	0.588	0.323	0.301	0.852	0.136	0.119	0.106	**0.013**
	30° offset	Sitting	0.562	0.544	0.278	0.285	0.797	0.231	**0.014**	0.217
	60° offset	Standing	0.044	**0.005**	0.560	0.505	0.818	0.120	0.062	0.850
	60° offset	45° Flex	0.079	0.653	0.174	0.528	0.324	**0.021**	0.520	0.512
	60° offset	Sitting	**0.038**	0.209	0.287	0.384	0.352	0.230	0.282	0.353
	ML	Standing	0.193	0.429	0.473	0.392	0.507	0.061	0.355	0.411
	ML	45° Flex	0.691	0.691	0.595	0.630	0.697	0.697	0.595	0.319
	ML	Sitting	0.819	0.308	0.546	0.287	0.731	0.584	0.254	0.537
Total	**90 of 104 normally distributed**									

Table C2 is a summary of the analyses of variance. Numerical values are the calculated F ratios which are greater than the critical F value. NS denotes not significant, in which the computed F ratio is less than the critical F value. Comparison of parametric to non-parametric statistical significance showed 42 of 48 (87.5%) agreements (original models) and 38 of 48 (79.2%) agreements (revised models).

Table C2: Summary of parametric and non-parametric ANCOVA analyses.

				Original Models		Revised Models	
	Metric	Factor	F Critical	Para-metric	Non Para-metric	Para-metric	Non Para-metric
All Pairs Data (n=45)	Yt	Orientation	2.7	NS	NS	**9.06**	**4.40**
		Flexion	3.1	**9.97**	**8.59**	**5.91**	**6.39**
		Interaction	2.2	NS	NS	NS	NS
	Abs Yt	Orientation	2.7	**3.43**	NS	**8.31**	**4.82**
		Flexion	3.1	**6.13**	**4.30**	NS	NS
		Interaction	2.2	NS	NS	NS	NS
	MTPM (t)	Orientation	2.7	**14.84**	**15.53**	**9.87**	**4.89**
		Flexion	3.1	**4.42**	**6.98**	NS	NS
		Interaction	2.2	**2.53**	NS	NS	NS
	MTPM (r)	Orientation	2.7	**4.93**	**3.38**	**4.06**	NS
		Flexion	3.1	NS	NS	NS	NS
		Interaction	2.2	NS	NS	NS	NS
Reference Data (n=9)	Yt	Orientation	2.7	**5.24**	**6.16**	**4.99**	NS
		Flexion	3.1	**41.29**	**42.32**	**23.38**	**32.53**
		Interaction	2.2	**2.58**	**2.66**	**3.04**	NS
	Abs Yt	Orientation	2.7	**3.94**	NS	**9.42**	**7.69**
		Flexion	3.1	**16.96**	**12.26**	**12.00**	**17.50**
		Interaction	2.2	NS	NS	NS	**2.54**
	MTPM (t)	Orientation	2.7	**30.33**	**41.89**	**8.21**	NS
		Flexion	3.1	NS	**6.51**	NS	NS
		Interaction	2.2	**10.71**	**6.56**	**3.44**	**2.91**
	MTPM (r)	Orientation	2.7	**7.63**	**6.70**	**7.39**	**6.85**
		Flexion	3.1	NS	NS	NS	NS
		Interaction	2.2	NS	NS	**3.43**	**4.12**

				Original Models		Revised Models	

	Metric	Factor	F Critical	Para-metric	Non Para-metric	Para-metric	Non Para-metric
Random Reference Data (n=9)	Yt	Orientation	2.7	NS	NS	**4.18**	**NS**
		Flexion	3.1	**3.68**	**5.09**	NS	**3.35**
		Interaction	2.2	**8.26**	**9.34**	**2.67**	**4.01**
	Abs Yt	Orientation	2.7	NS	NS	**5.89**	**5.41**
		Flexion	3.1	**8.53**	**6.60**	NS	NS
		Interaction	2.2	**3.05**	**3.17**	NS	**2.50**
	MTPM (t)	Orientation	2.7	**17.75**	**12.05**	**10.70**	**3.86**
		Flexion	3.1	**4.95**	**6.60**	NS	NS
		Interaction	2.2	**4.81**	**3.19**	**2.31**	**2.35**
	MTPM (r)	Orientation	2.7	**7.48**	**6.67**	**5.29**	**4.51**
		Flexion	3.1	**3.85**	NS	NS	**3.33**
		Interaction	2.2	NS	NS	**3.12**	**2.54**
Independent Pairs Data (n=5)	Yt	Orientation	2.8	NS	NS	NS	NS
		Flexion	3.2	NS	NS	**3.38**	**4.36**
		Interaction	2.3	NS	NS	NS	NS
	Abs Yt	Orientation	2.8	NS	NS	NS	**3.49**
		Flexion	3.2	**3.31**	**4.50**	NS	NS
		Interaction	2.3	NS	NS	NS	NS
	MTPM (t)	Orientation	2.8	**4.57**	**3.41**	NS	NS
		Flexion	3.2	NS	**3.77**	NS	NS
		Interaction	2.3	NS	NS	NS	NS
	MTPM (r)	Orientation	2.8	NS	NS	NS	NS
		Flexion	3.2	NS	NS	NS	NS
		Interaction	2.3	NS	NS	NS	NS

7.4 Appendix D

Tables D1 through D4 are the scoring tables used to analyze the statistical improvement of the imaging factors, orientation and flexion. The metric Yt is given a score of 4, MTPM (t) a score of 3, Abs(Yt) a score of 2, and MTPM (r) a score of 1. A negative score indicates that the setting was detrimental to the precision for that specific metric. A positive score indicates that the setting improved the precision for that specific metric.

Table D1: Scoring table of orientation and flexion settings, reference comparison data.

	Original Models				Revised Models			Models
Setting	Metric	Score (+/-)	Total		Metric	Score (+/-)	Total	Total
AP			0		MTPM (t)	-3	-3	-3
30° OS	Yt Abs Yt MTPM (t) MTPM (r)	-4 -2 -3 -1	-10		Abs Yt MTPM (r)	-2 -1	-3	-13
60° OS	MTPM (t) MTPM (r)	-3 -1	-4		Yt Abs Yt MTPM (t)	-4 -2 -3	-9	-13
ML	MTPM (r) Abs Yt	1 2	3		MTPM (r) Abs Yt Yt	1 2 4	7	10
Standing	Yt	4	4		MTPM (t) Abs Yt Yt	-3 2 4	3	7
45° Flex	Yt Abs Yt	-4 -2	-6		Yt	-4	-4	-10
Sitting			0				0	0

Table D2: Scoring table of orientation and flexion settings, all-pairs comparison data.

	Original Models				New Models			Models
Setting	Metric	Score (+/-)	Total		Metric	Score (+/-)	Total	Total
AP					MTPM (t)	+3	3	3
30° OS	Yt Abs Yt MTPM (t) MTPM (r)	-4 -2 -3 -1	-10		MTPM (r)	-1	-1	-11
60° OS	MTPM (t) Abs Yt	-3 -2	-5		Yt Abs Yt MTPM (t)	-4 -2 -3	-9	-14
ML	MTPM (r) Abs Yt	+1 +2	3		MTPM (r) Abs Yt Yt	+1 +2 +4	7	10
Standing	MTPM (r) Yt	-1 +4	3		MTPM (r) Abs Yt Yt	-1 +2 +4	5	8
45° Flex	Yt Abs Yt	-4 -2	-6				0	-6
Sitting	MTPM (t)	+3	3				0	3

Table D3: Scoring table of orientation and flexion settings, random reference comparison data.

	Original Models				Revised Models			Models
Setting	Metric	Score (+/-)	Total		Metric	Score (+/-)	Total	Total
AP	Yt	-4	-4		MTPM (r) MTPM (t)	-1 +3	2	-2
30° OS	MTPM (t) MTPM (r) Yt	-3 -1 +4	0		Abs Yt MTPM (r)	-2 -1	-3	-3
60° OS	Yt MTPM (t) MTPM (r)	-4 -3 -1	-8		Yt Abs Yt MTPM (t)	-4 -2 -3	-9	-17
ML	MTPM (r) Abs Yt	1 2	3		MTPM (r) Abs Yt Yt	1 2 4	7	10
	MTPM (r)	-1	-1		MTPM (r)	-1	5	4

Setting	Original Models				Revised Models			Models Total
	Metric	Score (+/-)	Total		Metric	Score (+/-)	Total	
Standing					Abs Yt	2		
					Yt	4		
45° Flex	Yt	-4	-5		Yt	-4	-3	-8
	Abs Yt	-2			MTPM (r)	+1		
	MTPM (r)	+1						
Sitting	MTPM (r)	-1	2		Yt	-4	-5	-5
	MTPM (t)	+3			MTPM (r)	-1		

Table D4: Scoring table of orientation and flexion settings, independent pairs comparison data.

Setting	Original Models				Revised Models			Models Total
	Metric	Score (+/-)	Total		Metric	Score (+/-)	Total	
AP	MTPM (t)	+3	4		MTPM (r)	-1	2	6
	Yt	+4			MTPM (t)	+3		
30° OS	Abs Yt	-2	-7		Abs Yt	-2	-7	-14
	MTPM (r)	-1			MTPM (r)	-1		
	Yt	-4			Yt	-4		
60° OS	MTPM (r)	-1	-1		Abs Yt	-2	-5	-6
					MTPM (t)	-3		
ML	MTPM (t)	3	4		MTPM (r)	1	6	10
	MTPM (r)	1			Abs Yt	2		
					MTPM (t)	3		
Standing	MTPM (r)	-1	-1				0	-1
45° Flex	Yt	-4	-6		Yt	-4	-5	-11
	Abs Yt	-2			Abs Yt	-2		
					MTPM (r)	+1		
Sitting	Abs Yt	+2	2		MTPM (t)	+3	3	5

7.5 Appendix E

The following tables are summaries of the standard deviation of motion (precision) between each TKA component and the surrounding cluster of markers, in which no relative motion occurs between the components and the markers. Original and revised models are presented for the only the reference dataset. N/A is indicated where there are <4 markers present in the marker cluster.

Table E1: Model-to-marker precision data for the tibia. Original models, reference dataset.

Orientation	Flexion	N	Xt (mm)	Yt (mm)	Zt (mm)	Xr (°)	Yr (°)	Zr (°)
AP	Standing	9	0.01487	0.00808	0.02957	0.06611	0.15135	0.05540
AP	45° Flex	8	0.02444	0.01359	0.03058	0.05460	0.10087	0.06035
AP	Sitting	9	0.01789	0.01547	0.02707	0.06655	0.11170	0.06145
30° Offset	Standing	7	0.01596	0.02039	0.03177	0.05305	0.38625	0.07750
30° Offset	45° Flex	8	0.01202	0.01588	0.02971	0.05378	0.17767	0.04071
30° Offset	Sitting	8	0.01210	0.01361	0.01481	0.04177	0.18101	0.04823
60° Offset	Standing	9	0.01170	0.01822	0.03542	0.08338	0.03718	0.01923
60° Offset	45° Flex	8	0.01842	0.01381	0.03741	0.09453	0.05807	0.05008
60° Offset	Sitting	9	0.01252	0.01477	0.02324	0.04761	0.11892	0.02963
ML	Standing	9	0.02833	0.01248	0.02093	0.06727	0.17411	0.05549
ML	45° Flex	8	0.01083	0.00746	0.03416	0.03528	0.07692	0.02430
ML	Sitting	9	0.01401	0.00815	0.04394	0.06343	0.13594	0.02775

Table E2: Model-to-marker precision data for the tibia. Revised models, reference dataset.

Orientation	Flexion	N	Xt (mm)	Yt (mm)	Zt (mm)	Xr (°)	Yr (°)	Zr (°)
AP	Standing	9	0.01618	0.00896	0.03547	0.08327	0.20190	0.05345
AP	45° Flex	7	0.02144	0.01332	0.03842	0.07420	0.23005	0.08325
AP	Sitting	9	0.02184	0.01551	0.03441	0.10298	0.14287	0.06214
30° Offset	Standing	7	0.01440	0.02008	0.03063	0.06686	0.31331	0.06912
30° Offset	45° Flex	8	0.01713	0.01682	0.01807	0.05046	0.17158	0.03066
30° Offset	Sitting	8	0.01726	0.02295	0.01849	0.05817	0.21803	0.05091
60° Offset	Standing	9	0.01156	0.03659	0.05713	0.15587	0.06200	0.02480
60° Offset	45° Flex	8	0.02002	0.02413	0.04848	0.15198	0.13536	0.05726
60° Offset	Sitting	9	0.01238	0.04119	0.04924	0.15749	0.13582	0.03194
ML	Standing	9	0.02718	0.01498	0.04517	0.10669	0.15310	0.06021
ML	45° Flex	8	0.01618	0.00942	0.02754	0.04252	0.08760	0.03453
ML	Sitting	9	0.01594	0.01052	0.04731	0.07676	0.22613	0.03448

Table E3: Model-to-marker precision data for the femur. Original models, reference dataset.

Orientation	Flexion	N	Xt (mm)	Yt (mm)	Zt (mm)	Xr (°)	Yr (°)	Zr (°)
AP	Standing	9	0.01186	0.01514	0.01933	0.04004	0.04846	0.03142
AP	45° Flex	N/A						
AP	Sitting	9	0.01874	0.03946	0.02991	0.12341	0.07023	0.03393
30° Offset	Standing	N/A						
30° Offset	45° Flex	8	0.03740	0.05165	0.05092	0.12201	0.08224	0.16178
30° Offset	Sitting	4	0.02290	0.02896	0.04585	0.12628	0.02928	0.05311
60° Offset	Standing	9	0.01518	0.02085	0.02458	0.13390	0.12647	0.02539
60° Offset	45° Flex	9	0.03013	0.04795	0.02790	0.12968	0.12996	0.06450
60° Offset	Sitting	9	0.00991	0.02416	0.02159	0.04594	0.10223	0.04610
ML	Standing	N/A						
ML	45° Flex	8	0.07583	0.04987	0.03699	0.05819	0.10290	0.10084
ML	Sitting	N/A						

Table E4: Model-to-marker precision data for the femur. Revised models, reference dataset.

Orientation	Flexion	N	Xt (mm)	Yt (mm)	Zt (mm)	Xr (°)	Yr (°)	Zr (°)
AP	Standing	9	0.00997	0.01369	0.01818	0.03507	0.03860	0.03199
AP	45° Flex	N/A						
AP	Sitting	9	0.01759	0.03779	0.03086	0.11489	0.06835	0.03568
30° Offset	Standing	N/A						
30° Offset	45° Flex	8	0.03255	0.05127	0.04719	0.10746	0.07998	0.15732
30° Offset	Sitting	4	0.02137	0.02327	0.04384	0.08713	0.03715	0.05432
60° Offset	Standing	9	0.01374	0.01884	0.02168	0.15708	0.12154	0.02098
60° Offset	45° Flex	9	0.02848	0.04467	0.02971	0.12032	0.14410	0.05465
60° Offset	Sitting	9	0.01392	0.02905	0.01874	0.04919	0.10568	0.07018
ML	Standing	N/A						
ML	45° Flex	8	0.07422	0.05176	0.04027	0.05717	0.09769	0.10755
ML	Sitting	N/A						

7.6 Appendix F

Table F1 is a summary of the mean and standard deviation of the bias (measured – actual motion) as well as the mean ½ width of the prediction interval. Table F2 is a summary of the slope and y-intercept (with 95% confidence intervals) as well as the R^2 coefficient of the linear regression between actual and measured motion. The conditions of AP/ML orientation and standing/sitting flexion are examined in the tables, and both the translation along and rotation about each axis is presented for the original and revised TKA models.

Table F1: Mean bias and ½ of the mean 95% confidence interval of the accuracy dataset.

			Original Models			Revised Models		
Knee Flexion	Imaging Orientation	Axis	Mean Bias	SD	Mean ½ 95% PI	Mean Bias	SD	Mean ½ 95% PI
Translation								
Sitting	AP	X	-0.0033	0.019	0.0329	-0.0014	0.020	0.0340
Sitting	ML	X	0.0579	0.025	0.0244	0.0579	0.036	0.0592
Standing	AP	X	-0.0178	0.026	0.0423	-0.0297	0.031	0.0476
Standing	ML	X	-0.0048	0.017	0.0190	-0.0016	0.022	0.0274
Sitting	AP	Y	0.0015	0.016	0.0261	-0.0021	0.019	0.0318
Sitting	ML	Y	0.0201	0.016	0.0117	0.0191	0.019	0.0165
Standing	AP	Y	-0.0338	0.017	0.0239	-0.0550	0.025	0.0365
Standing	ML	Y	-0.0068	0.035	0.0407	-0.0245	0.051	0.0547
Sitting	AP	Z	-0.1217	0.020	0.0341	-0.0918	0.014	0.0234
Sitting	ML	Z	-0.0562	0.014	0.0174	-0.0719	0.050	0.0524
Standing	AP	Z	-0.0700	0.068	0.0745	-0.1369	0.111	0.1205
Standing	ML	Z	0.0507	0.040	0.0645	0.1156	0.054	0.0692
Rotation								
Sitting	AP	X	-0.0143	0.099	0.1620	0.0450	0.103	0.1802
Sitting	ML	X	-0.1943	0.105	0.1540	-0.1014	0.192	0.1485
Standing	AP	X	-0.0829	0.051	0.0715	-0.1023	0.032	0.0550
Standing	ML	X	-0.2154	0.147	0.1571	-0.1217	0.248	0.1483
Sitting	AP	Y	0.1814	0.169	0.2582	0.2304	0.166	0.2752
Sitting	ML	Y	-0.2237	0.140	0.2436	0.0387	0.229	0.2655
Standing	AP	Y	0.0190	0.130	0.1802	0.1186	0.167	0.2402
Standing	ML	Y	0.1280	0.115	0.1869	0.1733	0.166	0.2637
Sitting	AP	Z	-0.0799	0.103	0.1223	-0.0577	0.133	0.1223
Sitting	ML	Z	-0.1056	0.120	0.2022	-0.0326	0.131	0.2108
Standing	AP	Z	0.0268	0.104	0.0928	0.0266	0.136	0.0882
Standing	ML	Z	-0.0652	0.082	0.1045	-0.0712	0.086	0.1087

Table F2: Slope, y-intercept (with 95% confidence interval) and R^2 of linear regression between actual and measured motion.

			Original Models					Revised Models				
Flexion	Orientation	Axis	Slope	+/- 95% Confidence	Intercept	+/- 95% Confidence	R^2	Slope	+/- 95% Confidence	Intercept	+/- 95% Confidence	R^2
Translation												
Standing	AP	X	0.9818	0.0899	-0.0121	0.0419	0.9957	0.9629	0.1012	-0.0182	0.0471	0.9943
Standing	ML	X	0.9664	0.0405	0.0057	0.0189	0.9991	0.9604	0.0584	0.0107	0.0272	0.9981
Sitting	AP	X	0.9970	0.0700	-0.0023	0.0326	0.9974	0.9889	0.0723	0.0021	0.0337	0.9972
Sitting	ML	X	1.0533	0.0518	0.0413	0.0242	0.9987	1.0311	0.1258	0.0482	0.0586	0.9923
Standing	AP	Y	0.9748	0.0509	-0.0260	0.0237	0.9986	0.9655	0.0776	-0.0443	0.0362	0.9967
Standing	ML	Y	0.9334	0.0864	0.0140	0.0403	0.9956	0.8965	0.1164	0.0077	0.0542	0.9913
Sitting	AP	Y	1.0159	0.0555	-0.0035	0.0259	0.9985	0.9933	0.0677	0.0000	0.0315	0.9976
Sitting	ML	Y	0.9606	0.0249	0.0324	0.0116	0.9997	0.9571	0.0351	0.0325	0.0164	0.9993
Standing	AP	Z	0.8614	0.1585	-0.0268	0.0739	0.9827	0.7741	0.2562	-0.0664	0.1194	0.9462
Standing	ML	Z	0.9613	0.1372	0.0628	0.0639	0.9895	0.9068	0.1471	0.1447	0.0685	0.9865
Sitting	AP	Z	1.0066	0.0726	-0.1237	0.0338	0.9973	0.9955	0.0498	-0.0904	0.0232	0.9987
Sitting	ML	Z	0.9759	0.0369	-0.0487	0.0172	0.9993	0.8948	0.1114	-0.0391	0.0519	0.9920
Rotation												
Standing	AP	X	1.0131	0.0250	-0.1131	0.0775	0.9997	1.0016	0.0193	-0.1060	0.0597	0.9998
Standing	ML	X	-0.9488	0.0550	-0.3332	0.1703	0.9983	-0.8977	0.0519	-0.3571	0.1609	0.9983
Sitting	AP	X	1.0148	0.0567	-0.0485	0.1757	0.9984	1.0007	0.0631	0.0433	0.1955	0.9979
Sitting	ML	X	-0.9750	0.0539	-0.2519	0.1670	0.9984	-0.9242	0.0520	-0.2757	0.1611	0.9984
Standing	AP	Y	1.0350	0.0631	-0.0615	0.1954	0.9981	1.0414	0.0840	0.0235	0.2605	0.9966
Standing	ML	Y	0.9813	0.0654	0.1710	0.2027	0.9977	1.0298	0.0923	0.1048	0.2860	0.9959
Sitting	AP	Y	1.0357	0.0904	0.0992	0.2800	0.9961	1.0219	0.0963	0.1801	0.2985	0.9954
Sitting	ML	Y	0.9983	0.0853	-0.2198	0.2642	0.9962	1.0754	0.0929	-0.1346	0.2879	0.9961
Standing	AP	Z	-0.9607	0.0325	-0.0636	0.1006	0.9994	-0.9446	0.0309	-0.1007	0.0956	0.9994
Standing	ML	Z	-1.0246	0.0366	-0.0086	0.1133	0.9993	-1.0257	0.0380	-0.0120	0.1179	0.9993
Sitting	AP	Z	-0.9671	0.0428	-0.1555	0.1326	0.9990	-0.9505	0.0428	-0.1716	0.1327	0.9989
Sitting	ML	Z	-0.9858	0.0708	-0.1382	0.2193	0.9973	-0.9775	0.0737	-0.0844	0.2286	0.9971

7.7 Appendix G

Table G1 is a summary of the RSA-measured and "known" wear volume and surface area (approximated as ½ of the total surface area of the wear pool) on each pre-worn insert for each RSA image and the 7 combinations of RSA images.

Table G1: RSA-measured and "known" wear volume and surface area for each insert..

Volume (mm^3)	Insert Number						
Image/Combination	620	625	633	1073	1079	Mean	SD
AP Stnd	76.7	66.5	79.5	85.2	51.8	72.0	13.2
ML Stnd	58.0	45.5	47.5	66.7	54.9	54.5	8.5
ML Sit	6.7	3.8	4.3	31.6	0.5	9.4	12.6
ML Sit ER	5.5	5.7	12.2	12.7	4.3	8.1	4.0
ML Sit IR	3.0	5.7	4.2	35.8	0.3	9.8	14.7
Comb 1	102.1	75.7	99.9	107.1	72.9	91.5	16.0
Comb 2	83.3	67.6	79.7	106.5	49.7	77.4	20.9
Comb 3	58.2	46.0	47.6	89.9	55.2	59.4	17.8
Comb 4	13.5	5.2	10.5	51.7	4.2	17.0	19.8
Comb 5	89.2	71.1	88.3	128.2	53.4	86.0	27.7
Comb 6	62.7	49.7	54.4	111.6	58.6	67.4	25.2
Comb 7 (all)	111.0	79.8	106.8	149.0	76.6	104.6	29.2
Known	169.4	237.1	696.4	385.1	178.2	333.2	220.6

Surface Area (mm^2)	Insert Number						
Image/Combination	620	625	633	1073	1079	Mean	SD
AP Stnd	431.7	402.3	437.2	426.9	368.1	413.2	28.5
ML Stnd	319.7	338.8	263.4	372.1	375.3	333.8	45.7
ML Sit	86.4	53.3	28.0	183.4	20.3	74.3	66.2
ML Sit ER	58.5	55.3	87.4	70.7	46.1	63.6	16.0
ML Sit IR	57.1	55.3	53.5	188.0	15.5	73.9	66.1
Comb 1	513.3	452.5	492.4	510.0	459.0	485.4	28.3
Comb 2	515.4	439.1	444.8	553.2	354.9	461.5	76.6
Comb 3	373.3	357.7	271.0	519.0	391.9	382.5	89.2
Comb 4	183.8	111.7	117.6	341.0	67.8	164.3	107.1
Comb 5	599.2	500.1	532.9	673.0	399.9	541.0	103.0
Comb 6	447.7	421.3	349.5	634.8	432.0	457.1	106.3
Comb 7 (all)	642.4	535.8	578.5	746.8	513.3	603.3	94.1
Known	1304.4	1318.2	1789.1	930.1	671.5	1202.7	425.5

Table G2 is the complete dataset of the RSA-measured wear for each RSA image and each combination of images, as a percentage of the "known" wear volume.

Table G2: RSA-measured wear as a percentage of the "known" wear volume and surface area.

Volume (%)	Insert Number						
Image/Combination	620	625	633	1073	1079	Mean	SD
AP Stnd	45.3	28.1	11.4	22.1	29.1	27.2	12.3
ML Stnd	34.3	19.2	6.8	17.3	30.8	21.7	11.0
ML Sit	3.9	1.6	0.6	8.2	0.3	2.9	3.3
ML Sit ER	3.3	2.4	1.8	3.3	2.4	2.6	0.7
ML Sit IR	1.7	2.4	0.6	9.3	0.2	2.8	3.7
Comb 1	60.3	31.9	14.3	27.8	40.9	35.0	17.0
Comb 2	49.2	28.5	11.4	27.7	27.9	28.9	13.4
Comb 3	34.4	19.4	6.8	23.3	31.0	23.0	10.8
Comb 4	7.9	2.2	1.5	13.4	2.4	5.5	5.1
Comb 5	52.7	30.0	12.7	33.3	29.9	31.7	14.2
Comb 6	37.0	21.0	7.8	29.0	32.9	25.5	11.5
Comb 7 (all)	65.5	33.7	15.3	38.7	43.0	39.2	18.1

Surface Area (%)	Insert Number						
Image/Combination	620	625	633	1073	1079	Mean	SD
AP Stnd	33.1	30.5	24.4	45.9	54.8	37.8	12.3
ML Stnd	24.5	25.7	14.7	40.0	55.9	32.2	16.0
ML Sit	6.6	4.0	1.6	19.7	3.0	7.0	7.3
ML Sit ER	4.5	4.2	4.9	7.6	6.9	5.6	1.5
ML Sit IR	4.4	4.2	3.0	20.2	2.3	6.8	7.5
Comb 1	39.3	34.3	27.5	54.8	68.3	44.9	16.5
Comb 2	39.5	33.3	24.9	59.5	52.8	42.0	14.1
Comb 3	28.6	27.1	15.1	55.8	58.4	37.0	19.1
Comb 4	14.1	8.5	6.6	36.7	10.1	15.2	12.3
Comb 5	45.9	37.9	29.8	72.4	59.6	49.1	17.0
Comb 6	34.3	32.0	19.5	68.3	64.3	43.7	21.4
Comb 7 (all)	49.2	40.6	32.3	80.3	76.4	55.8	21.5

Table G3 is the complete dataset of the wear volume-to-area ratio and yearly volumetric wear rate for each polyethylene insert (based on time *in vivo*), where area is approximated as ½ of the total surface area of the wear pool.

Table G3: Summary of the wear volume-to-area ratio, and yearly volumetric wear rate for each RSA image, combination of images, and the "known" wear areas of each insert.

	Insert Number						
	620	625	633	1073	1079	Mean	SD
Volume to Surface Area Ratio							
AP Stnd	0.1996	0.1778	0.1653	0.1819	0.1407	0.1731	0.0219
ML Stnd	0.1793	0.1815	0.1344	0.1802	0.1462	0.1643	0.0223
ML Sit	0.1723	0.0771	0.0715	0.1549	0.0237	0.0999	0.0621
ML Sit ER	0.1792	0.0942	0.1037	0.1399	0.0923	0.1219	0.0374
ML Sit IR	0.1905	0.0519	0.1031	0.0782	0.0214	0.0890	0.0644
Comb 1	0.2100	0.1989	0.1672	0.2028	0.1588	0.1875	0.0229
Comb 2	0.1926	0.1617	0.1539	0.1791	0.1400	0.1655	0.0207
Comb 3	0.1733	0.1560	0.1285	0.1757	0.1409	0.1549	0.0204
Comb 4	0.1517	0.0733	0.0462	0.0890	0.0626	0.0845	0.0406
Comb 5	0.1904	0.1489	0.1422	0.1658	0.1335	0.1562	0.0225
Comb 6	0.1757	0.1401	0.1180	0.1556	0.1356	0.1450	0.0218
Comb 7 (all)	0.1996	0.1728	0.1490	0.1846	0.1492	0.1710	0.0222
Known	0.4141	0.1299	0.1798	0.3892	0.2654	0.2757	0.1251
Yearly Volumetric Wear Rate (mm^3/yr)							
AP Stnd	8.32	124.44	40.51	73.40	32.71	55.88	44.84
ML Stnd	6.51	94.09	27.74	43.81	34.66	41.36	32.52
ML Sit	3.08	10.80	2.32	4.00	0.30	4.10	3.98
ML Sit ER	1.24	8.94	3.49	11.29	2.68	5.53	4.34
ML Sit IR	3.49	4.80	3.47	3.86	0.21	3.17	1.74
Comb 1	10.45	165.52	46.08	92.19	46.04	72.06	59.77
Comb 2	10.39	135.13	41.17	73.53	31.38	58.32	48.60
Comb 3	8.77	94.44	28.00	43.95	34.88	42.01	32.04
Comb 4	5.05	21.83	3.14	9.66	2.68	8.47	7.96
Comb 5	12.50	144.68	43.32	81.53	33.71	63.15	51.98
Comb 6	10.88	101.74	30.29	50.18	36.99	46.02	34.23
Comb 7 (all)	14.54	179.95	48.61	98.56	48.37	78.00	64.39
Known	37.57	274.67	144.40	642.83	112.57	242.41	239.69

Table G4 is a summary of the RSA-measured wear volume and surface area on the un-worn insert in four different configurations; AP standing and ML standing positions with 120 lb_f load, ML sitting position with 35 lb_f load, and AP standing with <5 lb_f load.

Table G3: RSA-measured wear volume and surface area (approximated as 1/2 of the total surface area of the whole wear pool) for four configurations of the RSA phantom.

Volume	Image Configuration			
Image #	AP Stnd	ML Stnd	ML Sit	AP Stnd Unloaded
1	35.35	22.96	1.63	10.83
2	39.30	25.84	1.99	12.67
3	41.50	24.76	2.53	14.92
4	37.96	31.54	1.61	12.56
5	38.73	32.38	1.74	7.35
6	36.85	28.39	1.13	17.47
7	41.44	29.75	2.16	N/A
8	44.17	32.21	1.66	N/A
9	38.36	30.97	1.52	N/A
10	41.96	31.92	1.79	N/A
Mean	39.56	29.07	1.78	12.63
SD	2.67	3.43	0.38	3.46
Area	AP Stnd	ML Stnd	ML Sit	AP Stnd Unloaded
1	615.0	534.6	58.4	260.8
2	656.2	563.9	64.3	284.1
3	675.1	552.3	76.4	273.7
4	653.2	605.8	57.4	222.7
5	655.6	613.7	59.9	216.2
6	645.1	579.4	39.2	290.9
7	676.5	596.3	71.3	N/A
8	696.0	614.6	53.9	N/A
9	657.6	606.6	53.2	N/A
10	676.1	615.9	58.6	N/A
Mean	660.64	588.31	59.26	258.07
SD	22.07	29.17	10.20	31.66

Figures G1 through G5 are the 5 RSA-measured wear areas and the “known” wear areas, on each of the pre-worn polyethylene inserts.

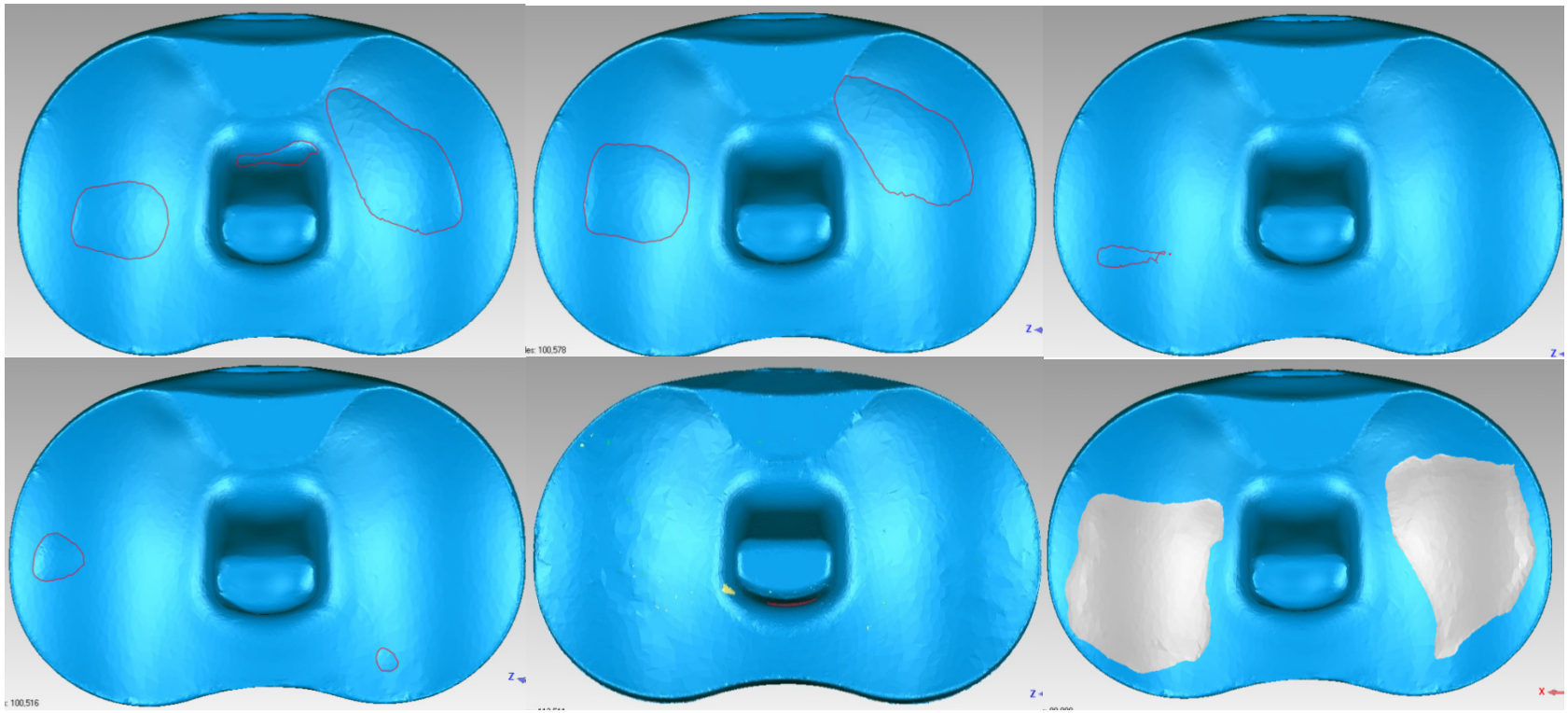

Figure G1: Insert #620, AP standing, ML standing, ML sitting, ML sitting with external rotation, ML sitting with internal rotation, and "known" wear areas.

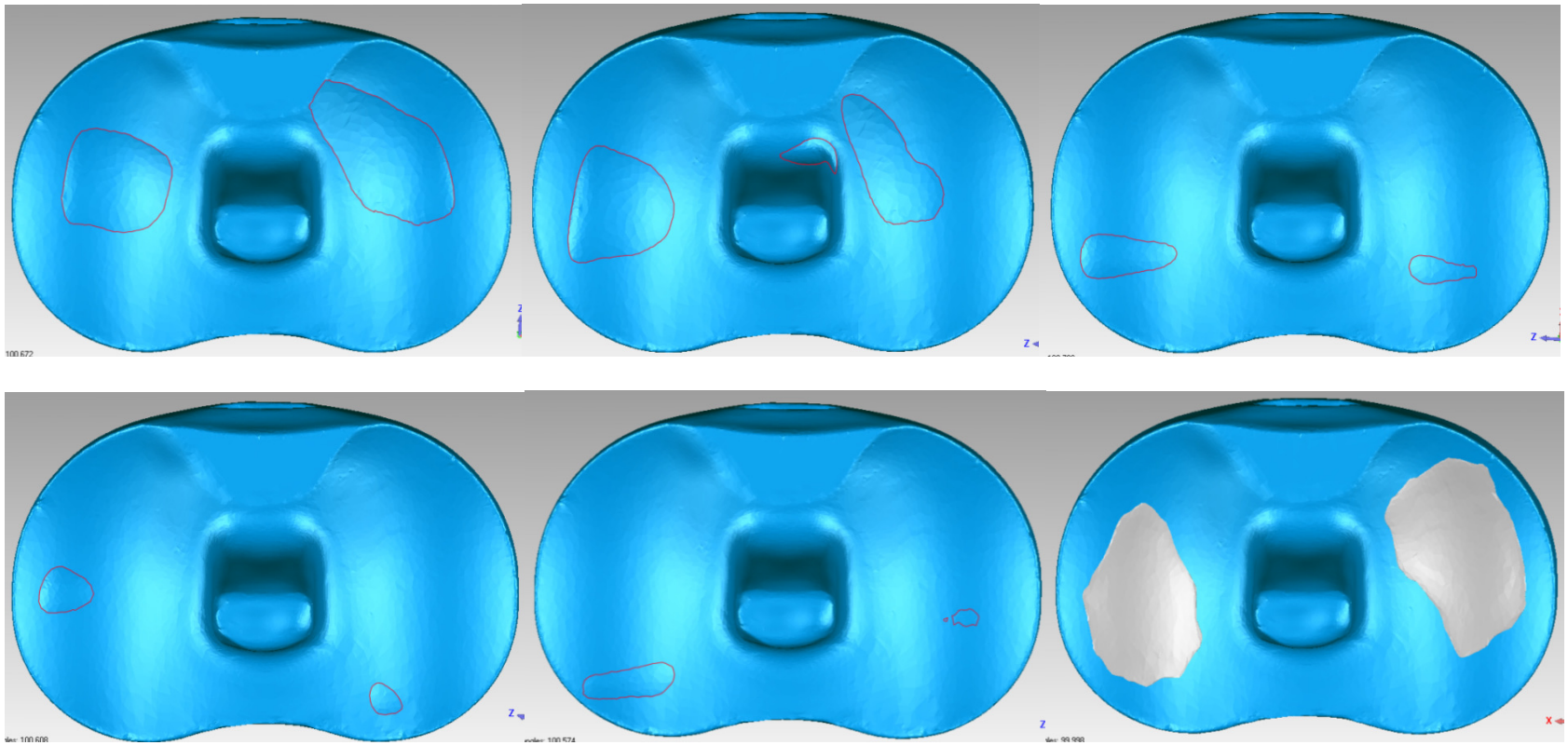

Figure G2: Insert # 625 AP standing, ML standing, ML sitting, ML sitting with external rotation, ML sitting with internal rotation, and "known" wear areas.

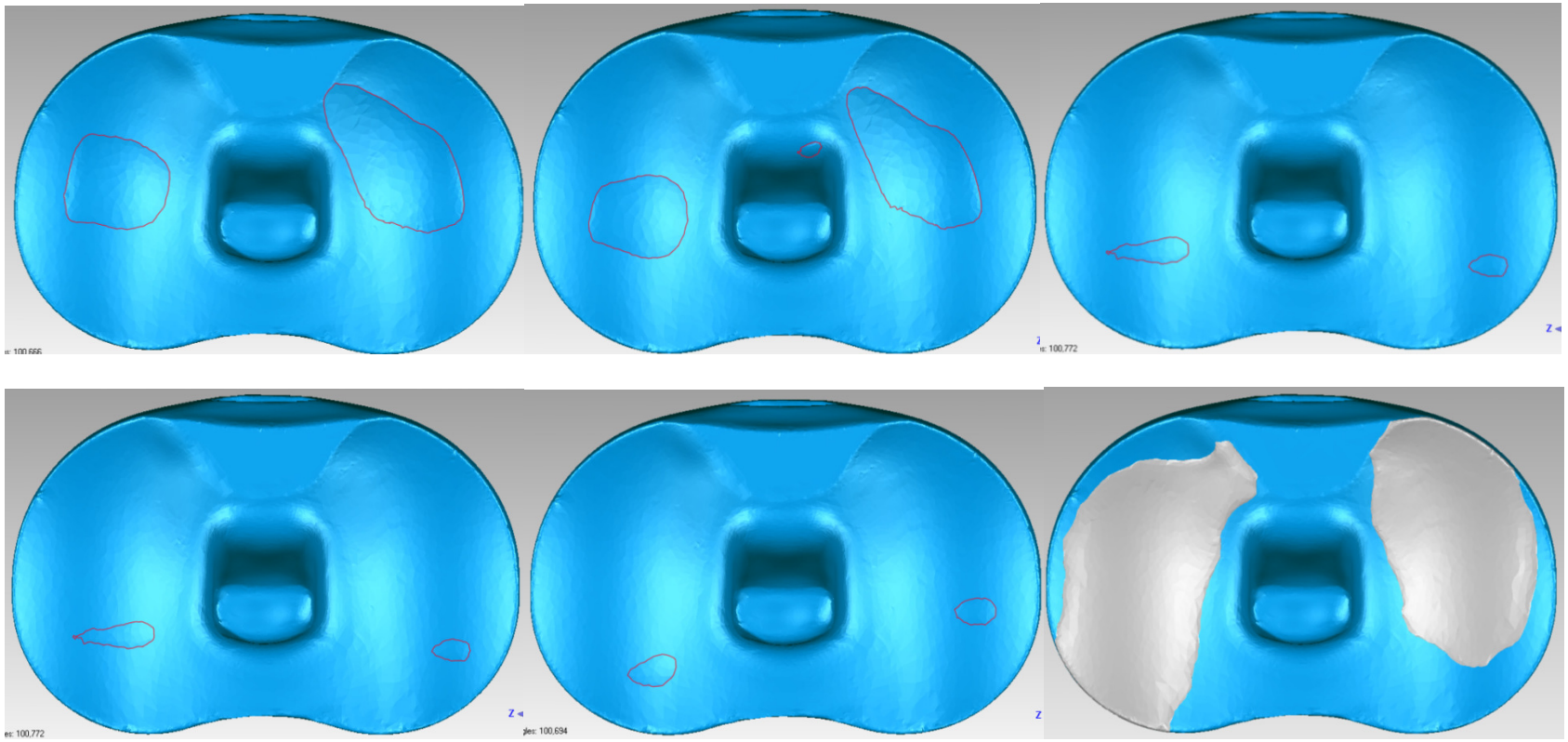

Figure G3: Insert #633 AP standing, ML standing, ML sitting, ML sitting with external rotation, ML sitting with internal rotation, and "known" wear areas.

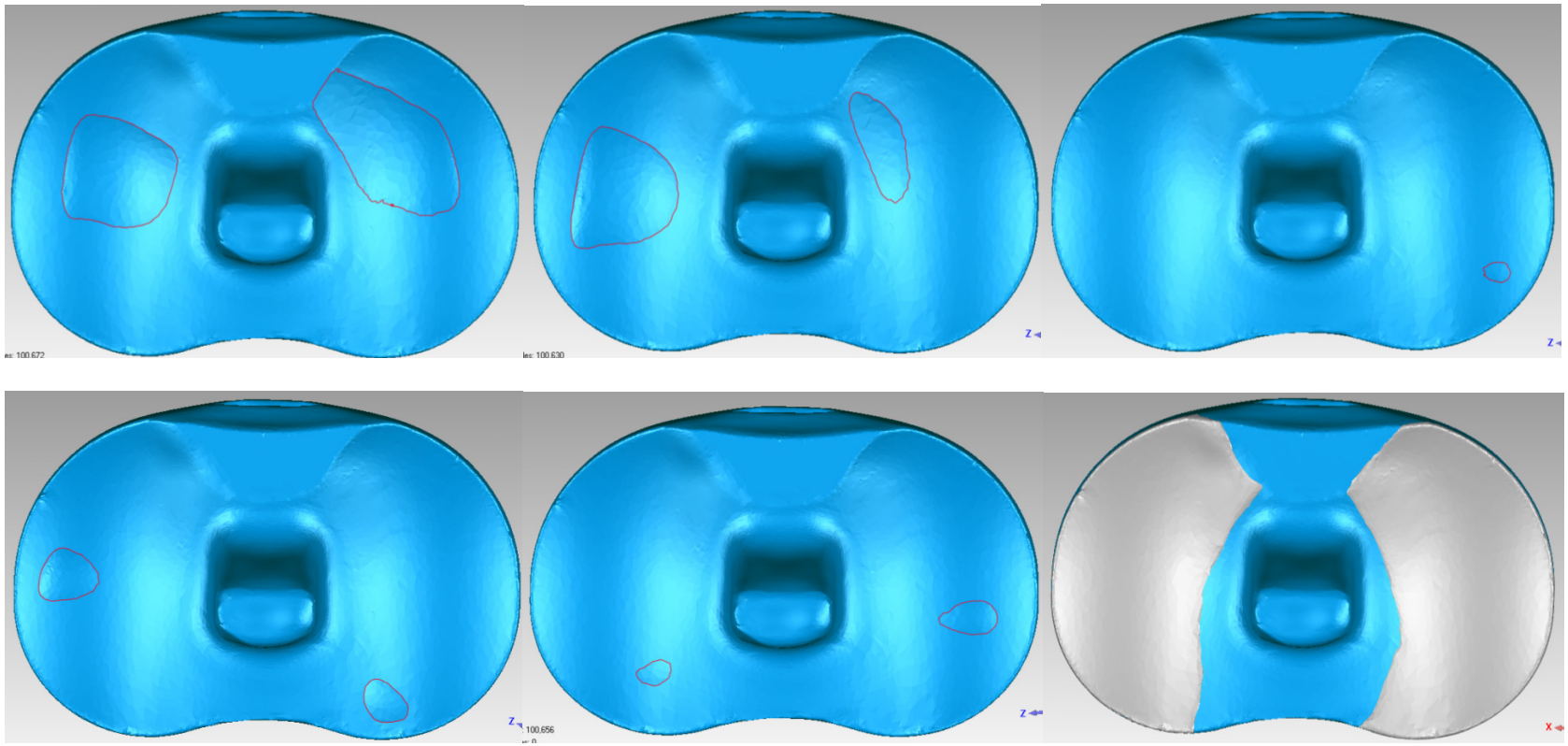

Figure G4: Insert #1073 AP standing, ML standing, ML sitting, ML sitting with external rotation, ML sitting with internal rotation, and "known" wear areas.

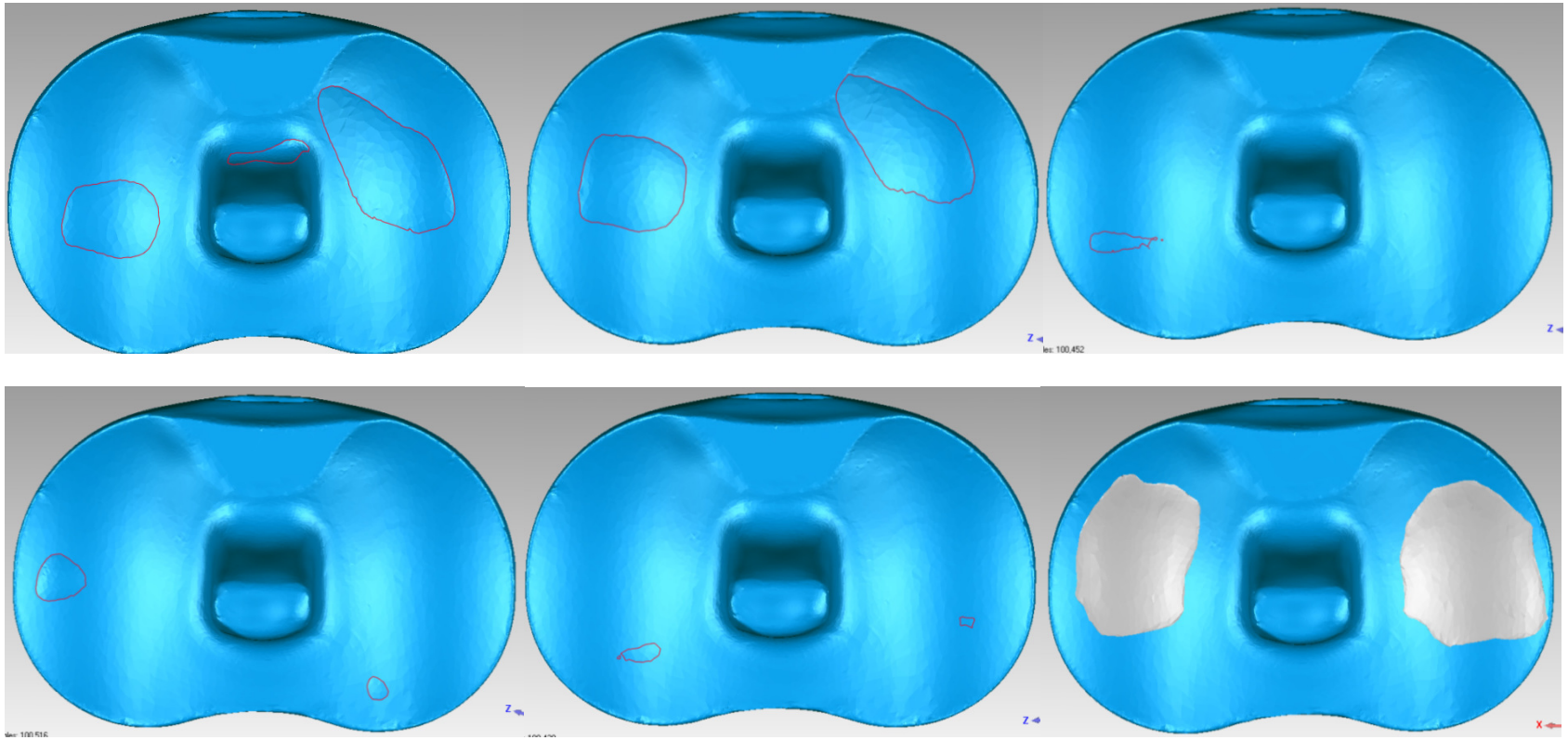

Figure G5: Insert #1079 AP standing, ML standing, ML sitting, ML sitting with external rotation, ML sitting with internal rotation, and "known" wear areas.